

THE JULY-AUGUST 1982
VOL. 61, NO. 6, PART 1



BELL SYSTEM
TECHNICAL JOURNAL

Electromagnetic Propagation in Homogeneous Media With Hermitian Permeability and Permittivity E. E. Bergmann	935
A Primal Algorithm for Finding Minimum-Cost Flows in Capacitated Networks With Applications C. L. Monma and M. Segal	949
Improved Reconstruction of DPCM-Coded Pictures A. N. Netravali and E. G. Bowen	969
An Improved Training Procedure for Connected-Digit Recognition L. R. Rabiner, A. Bergh, and J. G. Wilpon	981
Simulation and Design Studies of Digital Subscriber Lines S. V. Ahamed	1003
CONTRIBUTORS TO THIS ISSUE	1079
PAPERS BY BELL LABORATORIES AUTHORS	1083
CONTENTS, SEPTEMBER 1982 ISSUE	1093

THE BELL SYSTEM TECHNICAL JOURNAL

ADVISORY BOARD

D. E. PROCKNOW, *President*,
I. M. ROSS, *President*,
W. M. ELLINGHAUS, *President*,

Western Electric Company
Bell Telephone Laboratories, Incorporated
American Telephone and Telegraph Company

EDITORIAL COMMITTEE

A. A. PENZIAS, *Chairman*

M. M. BUCHNER, JR.	R. A. KELLEY
A. G. CHYNOWETH	R. W. LUCKY
R. P. CLAGETT	L. SCHENKER
T. H. CROWLEY	W. B. SMITH
B. P. DONOHUE, III	G. SPIRO
I. DORROS	J. W. TIMKO

EDITORIAL STAFF

B. G. KING, *Editor*
PIERCE WHEELER, *Managing Editor*
HEDWIG A. DEUSCHLE, *Assistant Editor*
H. M. PURVIANCE, *Art Editor*
B. G. GRUBER, *Circulation*

THE BELL SYSTEM TECHNICAL JOURNAL is published monthly, except for the May-June and July-August combined issues, by the American Telephone and Telegraph Company, C. L. Brown, Chairman and Chief Executive Officer; W. M. Ellinghaus, President; V. A. Dwyer, Vice President and Treasurer; T. O. Davis, Secretary. Editorial inquiries should be addressed to the Editor, The Bell System Technical Journal, Bell Laboratories, Room 1J-319, 101 J. F. Kennedy Parkway, Short Hills, N. J. 07078. Checks for subscriptions should be made payable to The Bell System Technical Journal and should be addressed to Bell Laboratories, Circulation Group, 101 J. F. Kennedy Parkway, Short Hills, N.J. 07078. Subscriptions \$20.00 per year; single copies \$2.00 each. Foreign postage \$1.00 per year; 15 cents per copy. Printed in U.S.A. Second-class postage paid at New Providence, New Jersey 07974 and additional mailing offices.

© 1982 American Telephone and Telegraph Company. ISSN0005-8580

Single copies of material from this issue of The Bell System Technical Journal may be reproduced for personal, noncommercial use. Permission to make multiple copies must be obtained from the editor.

Comments on the technical content of any article or brief are welcome. These and other editorial inquiries should be addressed to the Editor, The Bell System Technical Journal, Bell Laboratories, Room 1J-319, 101 J. F. Kennedy Parkway, Short Hills, N. J. 07078. Comments and inquiries, whether or not published, shall not be regarded as confidential or otherwise restricted in use and will become the property of the American Telephone and Telegraph Company. Comments selected for publication may be edited for brevity, subject to author approval.

THE BELL SYSTEM TECHNICAL JOURNAL

DEVOTED TO THE SCIENTIFIC AND ENGINEERING
ASPECTS OF ELECTRICAL COMMUNICATION

Volume 61

July-August 1982

Number 6, Part 1

Copyright © 1982 American Telephone and Telegraph Company. Printed in U.S.A.

Electromagnetic Propagation in Homogeneous Media With Hermitian Permeability and Permittivity

By E. E. BERGMANN

(Manuscript received November 5, 1981)

The problem of electromagnetic radiation traveling in a general homogeneous, but anisotropic and gyrotropic, medium has been solved. The plane wave representation is used to convert Maxwell's equations into a general eigenproblem, which allows for tensor permeability and permittivity and for electric and magnetic gyrotropy. This formulation can be applied directly to computer evaluation of wave velocities and polarizations for a given wave-normal direction. The reflection and refraction directions and amplitudes at an interface between two different, general anisotropic and gyrotropic media are solved. It is outlined how, with the aid of a digital computer, ray tracing through a general succession of anisotropic and gyrotropic, but locally homogeneous, media can be carried out.

I. INTRODUCTION

Traditionally, the theory of light propagation in transparent, anisotropic media has assumed that the permeability of the medium was the same as that of the vacuum, or at least that it was isotropic. Conversely, the theory of microwave propagation in ferrites and garnets has assumed that the permittivity was isotropic in spite of the permeability being anisotropic and possibly, gyrotropic. (References 1 and 2 are examples of the optics tradition and the microwave tradition, respectively.)

Both viewpoints are incomplete, particularly, when applied to in-

frared optics where anisotropy effects in both permeability and permittivity could be important. As a case in point, Yttrium Iron Garnet (YIG) is optically transparent at infrared wavelengths beyond $1 \mu\text{m}^3$ and at microwave frequencies; it could be used at wavelengths where the effects of permeability and permittivity are comparable.

We develop the theory of electromagnetic wave propagation in a homogeneous medium where both the permeability and permittivity are anisotropic. Furthermore, by assuming that the permittivity and permeability tensors are Hermitian, not merely real and symmetric, we incorporate the more general effects of gyrotropy.

II. BASIC ASSUMPTIONS

We assume the general validity of Maxwell's equations without "source terms" (no charges or currents):

$$\nabla \times \mathbf{H} = \partial \mathbf{D} / \partial t \quad (1)$$

$$\nabla \times \mathbf{E} = -\partial \mathbf{B} / \partial t \quad (2)$$

$$\nabla \cdot \mathbf{D} = 0 \quad (3)$$

$$\nabla \cdot \mathbf{B} = 0, \quad (4)$$

where \mathbf{E} , \mathbf{D} , \mathbf{B} , \mathbf{H} are complex vector fields which are functions of space and time (\mathbf{r} , t).

We shall restrict our considerations to plane-wave solutions where the above four vector fields can be cast in the form

$$\mathbf{F}(\mathbf{r}, t) = \mathbf{F}_0 \exp[i(\mathbf{k} \cdot \mathbf{r} - \omega t)], \quad (5)$$

where \mathbf{F}_0 is a complex vector constant and ω is a real constant. The vector, \mathbf{k} , is usually considered to be real, but may be complex even in lossless media (for "evanescent waves").

To complete the specifications, we need to define material-dependent relationships between the four vector fields of Maxwell's equations. We do so by means of the electromagnetic energy density:

$$U = \frac{1}{2} \mathbf{E}^* \cdot \mathbf{D} + \frac{1}{2} \mathbf{H}^* \cdot \mathbf{B}. \quad (6)$$

For a plane wave, we can substitute (5) into (6) to show that U is independent of time and position (assuming \mathbf{k} is real):

$$U = \frac{1}{2} \mathbf{E}_0^* \cdot \mathbf{D}_0 + \frac{1}{2} \mathbf{H}_0^* \cdot \mathbf{B}_0. \quad (7)$$

By assuming that U is a purely quadratic function of the components of \mathbf{E}_0^* , we obtain

$$\mathbf{D}_0 = \tilde{\epsilon} \mathbf{E}_0. \quad (8)$$

The Hermiticity of $\tilde{\epsilon}$, the permittivity or dielectric tensor, follows from the reality of U .

Similarly, by assuming that U is a purely quadratic function of the components of \mathbf{H}_0 , we conclude that

$$\mathbf{B}_0 = \bar{\mu}\mathbf{H}_0, \quad (9)$$

where the permeability tensor, $\bar{\mu}$, is Hermitian.

Our assumptions are consistent with magneto-optic effects where, conventionally, a Polder tensor⁴ is defined, e.g.,

$$\bar{\mu} = \begin{pmatrix} \mu & i\mu_a & 0 \\ -i\mu_a & \mu & 0 \\ 0 & 0 & \mu' \end{pmatrix}. \quad (10)$$

Using the plane-wave representation (5) in Maxwell's first pair of equations, (1) and (2), we obtain

$$\mathbf{k} \times \mathbf{H} = -\omega\mathbf{D}. \quad (11)$$

$$\mathbf{k} \times \mathbf{E} = \omega\mathbf{B}. \quad (12)$$

Similar substitutions into Maxwell's last pair of equations, (3) and (4),

$$\mathbf{k} \cdot \mathbf{D} = 0 \quad (13)$$

$$\mathbf{k} \cdot \mathbf{B} = 0, \quad (14)$$

which, in fact, follow from (11) and (12) when $\omega \neq 0$.

III. THE WAVE VELOCITY

We rewrite the plane-wave representation (5) in a suggestive form

$$\mathbf{F} = \mathbf{F}_0 \exp[-(\text{Im} \mathbf{k}) \cdot \mathbf{r}] \cdot \exp[i|\text{Re} \mathbf{k}|(\hat{n} \cdot \mathbf{r} - v_w t)], \quad (15)$$

where

$$\hat{n} = \text{Re} \mathbf{k} / |\text{Re} \mathbf{k}| \quad (16)$$

is a unit vector that is normal to the wave fronts, and the wave velocity

$$v_w = \omega / |\text{Re} \mathbf{k}|. \quad (17)$$

Thus, v_w represents the rate at which the wave fronts appear to be advancing in the \hat{n} direction.

We usually assume that $\text{Im} \mathbf{k} = 0$. However, for $\text{Im} \mathbf{k} \neq 0$ we have an "evanescent wave"; a wave whose intensity diminishes in the $\text{Im} \mathbf{k}$ direction. It will be shown later, under the discussion of Poynting's vector, that $\text{Im} \mathbf{k}$ is perpendicular to Poynting's vector in nondissipative media.

Let us assume now that $\text{Im} \mathbf{k} = 0$ and that, consequently, \hat{n} is parallel to \mathbf{k} . We can restate (25) and (26) as follows:

$$\hat{n} \times \mathbf{H} = -v_w \mathbf{D} = -v_w \bar{\epsilon} \mathbf{E} \quad (18)$$

$$\hat{n} \times \mathbf{E} = v_w \mathbf{B} = v_w \hat{\mu} \mathbf{H}. \quad (19)$$

If we go to a six-dimensional representation, we may combine (18) and (19) into a single-matrix equation:

$$\begin{pmatrix} 0 & 0 & 0 & 0 & \hat{n}_z & -\hat{n}_y \\ 0 & 0 & 0 & -\hat{n}_z & 0 & \hat{n}_x \\ 0 & 0 & 0 & \hat{n}_y & -\hat{n}_x & 0 \\ 0 & -\hat{n}_z & \hat{n}_y & 0 & 0 & 0 \\ \hat{n}_z & 0 & -\hat{n}_x & 0 & 0 & 0 \\ -\hat{n}_y & \hat{n}_x & 0 & 0 & 0 & 0 \end{pmatrix} \begin{pmatrix} E_x \\ E_y \\ E_z \\ H_x \\ H_y \\ H_z \end{pmatrix} = v_w \begin{pmatrix} \epsilon_{xx} & \epsilon_{xy} & \epsilon_{xz} & 0 & 0 & 0 \\ \epsilon_{yx} & \epsilon_{yy} & \epsilon_{yz} & 0 & 0 & 0 \\ \epsilon_{zx} & \epsilon_{zy} & \epsilon_{zz} & 0 & 0 & 0 \\ 0 & 0 & 0 & \mu_{xx} & \mu_{xy} & \mu_{xz} \\ 0 & 0 & 0 & \mu_{yx} & \mu_{yy} & \mu_{yz} \\ 0 & 0 & 0 & \mu_{zx} & \mu_{zy} & \mu_{zz} \end{pmatrix} \begin{pmatrix} E_x \\ E_y \\ E_z \\ H_x \\ H_y \\ H_z \end{pmatrix}. \quad (20)$$

For convenience, we shall compress (20) by defining a more compact notation

$$\begin{pmatrix} 0 & -\vec{N} \\ \vec{N} & 0 \end{pmatrix} \begin{pmatrix} \mathbf{E} \\ \mathbf{H} \end{pmatrix} = v_w \begin{pmatrix} \vec{\epsilon} & 0 \\ 0 & \vec{\mu} \end{pmatrix} \begin{pmatrix} \mathbf{E} \\ \mathbf{H} \end{pmatrix} \quad (21)$$

or

$$\vec{\alpha} \mathbf{v} = v_y \vec{\beta} \mathbf{v}. \quad (22)$$

Note that (22) is clearly a general eigenproblem. The tensor, $\vec{\beta}$, is determined by the permeability and permittivity of the medium. If \mathbf{k} is real, then $\vec{\alpha}$ is determined completely by \hat{n} .

Both $\vec{\alpha}$ and $\vec{\beta}$ are usually Hermitian. Tensor, $\vec{\alpha}$, is symmetric. It is real if \mathbf{k} was real. We can restate (6) as

$$2U = \mathbf{v}^* \cdot \vec{\beta} \mathbf{v}. \quad (23)$$

Away from dramatic resonances, we may assume that U is positive definite as well as real. If so, $\vec{\beta}$ is not only Hermitian but positive definite.

When $\vec{\beta}$ is both Hermitian and positive definite, we can find its inverse and its square root (all of which are Hermitian and positive definite as well). Thus, we are able to convert (8) to an ordinary eigenproblem of a Hermitian matrix:

$$(\vec{\beta}^{-1/2} \vec{\alpha} \vec{\beta}^{-1/2}) (\vec{\beta}^{1/2} \mathbf{v}) = v_w (\vec{\beta}^{1/2} \mathbf{v}). \quad (24)$$

The Hermiticity of $(\vec{\beta}^{-1/2} \vec{\alpha} \vec{\beta}^{-1/2})$ guarantees that there are six eigen-solutions, each with a real v_w .

We can use the Hermiticity of $\vec{\alpha}$ and $\vec{\beta}$ to prove orthogonality:

$$\nu_1^* \cdot \vec{\alpha} \nu_2 = \nu_{w1}^* \nu_1^* \cdot \vec{\beta} \nu_2 = \nu_{w2} \nu_1^* \cdot \vec{\beta} \nu_2. \quad (25)$$

Clearly, when ν_{w1}^* does not equal ν_{w2} , the corresponding eigenvectors satisfy the orthogonality relations:

$$\nu_1^* \cdot \vec{\alpha} \nu_2 = 0 = \nu_1^* \cdot \vec{\beta} \nu_2. \quad (26)$$

Additional orthogonality relationships can be proved if $\nu_{w1}^n \neq \nu_{w2}^n$ ($n = 1, 2, 3 \dots$):

$$\nu_1^* \cdot \vec{\beta} (\vec{\beta}^{-1} \vec{\alpha})^n \nu_2 = 0. \quad (27)$$

Two eigensolutions can be provided automatically:

$$\begin{aligned} \nu_5 &= \begin{pmatrix} \hat{n} \\ 0 \end{pmatrix} \quad \text{and} \quad \nu_6 = \begin{pmatrix} 0 \\ \hat{n} \end{pmatrix} \\ \nu_{w5} &= 0 \quad \text{and} \quad \nu_{w6} = 0. \end{aligned} \quad (28)$$

Thus, we have to find four more eigensolutions to this six-dimensional eigenproblem.

The reality of \hat{n} and the special form of $\vec{\beta}$ enable us to simplify the problem still further. Suppose we have a solution to (21). It follows then that

$$\begin{pmatrix} 0 & -\vec{N} \\ \vec{N} & 0 \end{pmatrix} \begin{pmatrix} \mathbf{E} \\ -\mathbf{H} \end{pmatrix} = -\nu_w \begin{pmatrix} \vec{\epsilon} & 0 \\ 0 & \vec{\mu} \end{pmatrix} \begin{pmatrix} \mathbf{E} \\ -\mathbf{H} \end{pmatrix}. \quad (29)$$

Thus, for each eigensolution with wave velocity ν_w , there is an analogous solution that travels in the opposite direction.

In summary, of the six solutions to the eigenproblem (20) for a specified, real \hat{n} , two are trivial and have zero wave velocity, two are positive and correspond to two polarized solutions propagating in the $+\hat{n}$ direction, and the last two are negative, and, consequently, travel in the $-\hat{n}$ direction.

It is worthwhile noting that we have included nonreciprocal cases, since Faraday rotation, the traditional nonreciprocal effect, is manifested by complex, yet Hermitian, permittivity and/or permeability tensors. These effects do not seem to cause the wave velocities in the $-\hat{n}$ direction to differ from those in the $+\hat{n}$ direction. The nonreciprocal effects must be manifest in the differing polarizations between the forward and the backward directions.

Polarization is specified usually by the orientation of the electromagnetic field components normal to the relevant velocity direction (here \hat{n}). Thus, from eqs. (13) and (14) we should concentrate upon \mathbf{D} , when \mathbf{k} is real. In general, the components of \mathbf{D} , say, are complex; then the polarization should be considered elliptical. The special case of $\mathbf{D} \propto \mathbf{D}^*$ is called "linear polarization." Since \mathbf{D} is confined to the plane

perpendicular to \mathbf{k} , its description for a specified \hat{n} can be reduced always to two complex vector components; this two-dimensional representation is known as the Jones vector.^{5,6}

Nonreciprocity is the inequivalence of wave velocity (or attenuation, which we ignore here) for a given polarization for the $\pm\hat{n}$ directions. The reason that Faraday rotation is nonreciprocal is that the polarization for a given magnitude of wave velocity in the $\pm\hat{n}$ directions are not the same; the Jones vector representation for the $\pm\hat{n}$ directions associate right-handed elliptical polarization to left-hand elliptical polarization in the opposite direction. Two polarizations in the $\pm\hat{n}$ directions would be considered the same if the corresponding \mathbf{D} fields obeyed the proportionality

$$\mathbf{D}_1 \propto \mathbf{D}_2^* \quad (30)$$

Thus, nonreciprocity for solutions consistent with (20) could occur only when \mathbf{D}^* is not proportional to \mathbf{D} ; no nonreciprocity occurs for modes that are linearly polarized. It also appears to be a consequence of the form of (20) that no polarization-independent nonreciprocity can be produced in homogeneous media. However, if the medium is bianisotropic, then polarization-independent nonreciprocity is possible (see Ref. 7).

The orthogonality relations (26) and (27) derived earlier, can be used to show that the two polarizations associated with the two different wave velocities in a given \hat{n} -direction are "perpendicular." Let us call these solutions, "fast" and "slow." By assuming that $\omega \neq 0$, we can derive from the orthogonality relation

$$\mathbf{E}_{\text{fast}}^* \cdot \mathbf{D}_{\text{slow}} + \mathbf{H}_{\text{fast}}^* \cdot \mathbf{B}_{\text{slow}} = 0. \quad (31)$$

Since \mathbf{E}_{fast} , $-\mathbf{H}_{\text{fast}}$ is again a solution with yet another v_w , we can derive from orthogonality

$$\mathbf{E}_{\text{fast}}^* \cdot \mathbf{D}_{\text{slow}} - \mathbf{H}_{\text{fast}}^* \cdot \mathbf{B}_{\text{slow}} = 0. \quad (32)$$

Thus, we can conclude from (31) and (32) that

$$\mathbf{E}_{\text{fast}}^* \cdot \mathbf{D}_{\text{slow}} = 0 \quad (33)$$

$$\mathbf{H}_{\text{fast}}^* \cdot \mathbf{B}_{\text{slow}} = 0. \quad (34)$$

We see from (31) also that there is no interference in the energy density between the fast and slow solutions for a given direction, \hat{n} . Suppose at some location

$$\mathbf{v} = a\mathbf{v}_{\text{fast}} + b\mathbf{v}_{\text{slow}}, \quad (35)$$

then

$$U = \frac{1}{2}\mathbf{v} \cdot \vec{\beta}\mathbf{v} = \frac{1}{2}|a|^2\mathbf{v}_{\text{fast}}^* \cdot \vec{\beta}\mathbf{v}_{\text{fast}} + \frac{1}{2}|b|^2\mathbf{v}_{\text{slow}}^* \cdot \vec{\beta}\mathbf{v}_{\text{slow}}. \quad (36)$$

Usually, the literature considers the more restrictive cases,⁸ where either $\vec{\mu}$ or $\vec{\epsilon}$ is isotropic and conclude

$$\mathbf{D}_{\text{fast}}^* \cdot \mathbf{D}_{\text{slow}} = 0(?),$$

which is not always true for more general cases such as are considered here.

IV. THE POYNTING VECTOR

If we consider the time dependence of U , we derive:

$$\frac{dU}{dt} = \frac{1}{2} \frac{d\mathbf{v}^* \cdot \vec{\beta}}{dt} \mathbf{v} + \frac{1}{2} \mathbf{v}^* \cdot \frac{d\vec{\beta} \mathbf{v}}{dt} = \text{Re} \left(\mathbf{v}^* \cdot \frac{d\vec{\beta} \mathbf{v}}{dt} \right). \quad (37)$$

By using Maxwell's eqs. (1) and (2), we obtain further:

$$dU/dt = \text{Re}(\mathbf{E}^* \cdot \nabla \times \mathbf{H} - \mathbf{H}^* \cdot \nabla \times \mathbf{E}) = \nabla \cdot [\text{Re}(\mathbf{E}^* \times \mathbf{H})]. \quad (38)$$

As we have identified dU/dt with the divergence of a "flux," this flux should be identified with Poynting's vector. With this in mind, we make two definitions

$$\mathbf{G} \equiv \mathbf{E}^* \times \mathbf{H} \quad (39)$$

and

$$\mathbf{S} \equiv \text{Re } \mathbf{G}. \quad (40)$$

For a plane wave of real \mathbf{k} , \mathbf{G} is independent of time and space. However, it may be complex. The real part of \mathbf{G} , namely, \mathbf{S} , is Poynting's vector and is always real, obviously.

The vectors \mathbf{G} and \mathbf{G}^* are useful because they are "dual" to \mathbf{k} . Consider

$$\begin{aligned} \mathbf{G} \times \mathbf{D} &= \mathbf{H}(\mathbf{E}^* \cdot \mathbf{D}) - \mathbf{E}^*(\mathbf{H} \cdot \mathbf{D}) \\ &= \mathbf{H}(\mathbf{E}^* \cdot \mathbf{D}) + \omega^{-1} \mathbf{E}^*(\mathbf{H} \cdot \mathbf{k} \times \mathbf{H}) = U\mathbf{H}. \end{aligned}$$

Consequently,

$$\mathbf{G} \times \mathbf{D} = U\mathbf{H}. \quad (41)$$

A similar derivation shows

$$\mathbf{G}^* \times \mathbf{B} = -U\mathbf{E}. \quad (42)$$

These two equations are analogous to (12) and (11) and suggest a series of steps that are usable for calculating the ray velocity.

The ray velocity vector, \mathbf{v}_r , which is parallel to the Poynting vector, \mathbf{S} , is defined as

$$\mathbf{v}_r \equiv \mathbf{S}/U \quad (43a)$$

$$v_r \equiv |\mathbf{v}_r|. \quad (43b)$$

The Appendix proves that the Poynting vector is indeed the ray direction.

Unlike the theory for \mathbf{k} , we will *not* be able to assume that \mathbf{G} is real. Nevertheless, we define

$$\hat{\mathbf{g}} \equiv \mathbf{G}/|\operatorname{Re} \mathbf{G}| \quad (44)$$

and

$$\hat{\mathbf{s}} \equiv \operatorname{Re} \hat{\mathbf{g}} = \mathbf{S}/|\mathbf{S}|. \quad (45)$$

With these notational conventions, we restate (5) and (6)

$$\hat{\mathbf{g}}^* \times \mathbf{B} = -v_r^{-1} \mathbf{E} = -v_r^{-1} \tilde{\epsilon}^{-1} \mathbf{D} \quad (46)$$

$$\hat{\mathbf{g}} \times \mathbf{D} = v_r^{-1} \mathbf{H} = v_r^{-1} \tilde{\mu}^{-1} \mathbf{B}. \quad (47)$$

These two relations can be rewritten as an eigencondition:

$$\begin{pmatrix} 0 & 0 & 0 & 0 & \hat{g}_z^* & -\hat{g}_y^* \\ 0 & 0 & 0 & -\hat{g}_z^* & 0 & \hat{g}_x^* \\ 0 & 0 & 0 & \hat{g}_y^* & -\hat{g}_x^* & 0 \\ 0 & -\hat{g}_z & \hat{g}_y & 0 & 0 & 0 \\ \hat{g}_z & 0 & -\hat{g}_x & 0 & 0 & 0 \\ -\hat{g}_y & \hat{g}_x & 0 & 0 & 0 & 0 \end{pmatrix} \begin{pmatrix} D_x \\ D_y \\ D_z \\ B_x \\ B_y \\ B_z \end{pmatrix} = v_r^{-1} \tilde{\beta}^{-1} \begin{pmatrix} D_x \\ D_y \\ D_z \\ B_x \\ B_y \\ B_z \end{pmatrix}. \quad (48)$$

And a terser notation, analogous to (22), could be

$$\tilde{\Gamma} \mathbf{v} = v_r^{-1} \tilde{\beta}^{-1} \mathbf{v}, \quad (49)$$

where $\tilde{\Gamma}$ is Hermitian; $\tilde{\beta}$ is positive definite and Hermitian because

$$2U = \mathbf{v}^* \cdot \tilde{\beta}^{-1} \mathbf{v} \quad (50)$$

in analogy to (23).

In accordance with the analogous discussion of the solutions (22), the six real eigenvalue solutions to (49) will consist of two zero v_r^{-1} , two positive v_r^{-1} , and their two negatives. Similar orthogonality relations can also be generated.

The duality⁹ would be complete if $\hat{\mathbf{g}}$ were equal to $\hat{\mathbf{s}}$. If \mathbf{k} and $\tilde{\beta}$ were real, we could expect that $\mathbf{G} = \mathbf{S}$. However, we have demonstrated by computer that a real \mathbf{k} does not always lead to a real \mathbf{G} .

Thus, we must conclude that to solve for v_r starting with a given $\hat{\mathbf{s}}$, we must find the appropriate values of $\operatorname{Im} \hat{\mathbf{g}}$ that produce a real \mathbf{k} in

a test such as

$$U\mathbf{k} = \omega(\mathbf{D}^* \times \mathbf{B}). \quad (51)$$

We shall show now that if \mathbf{k} is complex, then its imaginary part is perpendicular to \mathbf{S} . From (11) and (12), we can generate

$$-\mathbf{E}^* \cdot \mathbf{k} \times \mathbf{H} = \omega \mathbf{E}^* \cdot \mathbf{D} \quad (52)$$

$$\mathbf{H}^* \cdot \mathbf{k} \times \mathbf{E} = \omega \mathbf{H}^* \cdot \mathbf{B}. \quad (53)$$

Adding (52) and (53), we obtain

$$\mathbf{k} \cdot (\mathbf{E}^* \times \mathbf{H} + \mathbf{E} \times \mathbf{H}^*) = \omega(\mathbf{E}^* \cdot \mathbf{D} + \mathbf{H}^* \cdot \mathbf{B}). \quad (54)$$

Using the definitions of Poynting's vector and energy density, we can restate (54) as

$$\mathbf{k} \cdot \mathbf{S} = \omega U. \quad (55)$$

Because ω , U , and \mathbf{S} are always assumed to be real, we can conclude that

$$\mathbf{S} \cdot \text{Im } \mathbf{k} = 0. \quad (56)$$

V. REFLECTION AND REFRACTION

We can find the reflection and refraction of a plane wave at a flat interface between two different, homogeneous media of the general type we have been considering.

Figure 1 indicates what we should expect at the interface between two media. The \mathbf{k}_0 is the propagation vector of the incident wave. Usually, there will be two reflected waves, represented by \mathbf{k}_1 and \mathbf{k}_2 , and two refracted (transmitted) waves, represented by \mathbf{k}_3 and \mathbf{k}_4 . Details of the four "scattered" waves are determined by boundary conditions.

To determine \mathbf{k}_1 , \mathbf{k}_2 , \mathbf{k}_3 , and \mathbf{k}_4 for a particular \mathbf{k}_0 , the boundary conditions we need to consider are the equality of the $\omega(\mathbf{k})$ associated with all five \mathbf{k} vectors. In addition, because the geometry possesses two-dimensional translational symmetry in the plane of the interface, we must match the components in the plane of the interface for all the \mathbf{k} vectors. These constraints are sufficient to determine the four "scattered" \mathbf{k} vectors for a given \mathbf{k}_0 .

Finding the scattered \mathbf{k} vectors amounts to specifying the components of $\boldsymbol{\gamma} \equiv \mathbf{k}/\omega$ that are in the plane of the interface, $\boldsymbol{\gamma}_\parallel$, and solving an eigenproblem that provides

$$\boldsymbol{\gamma}_\perp^{-1} \equiv \omega/|\mathbf{k} \cdot \hat{\boldsymbol{x}}_\perp|. \quad (57)$$

We define $\hat{\boldsymbol{x}}_\perp$, for notational convenience, as a unit vector perpendicular to the interface and directed in the same sense as the incident radiation.

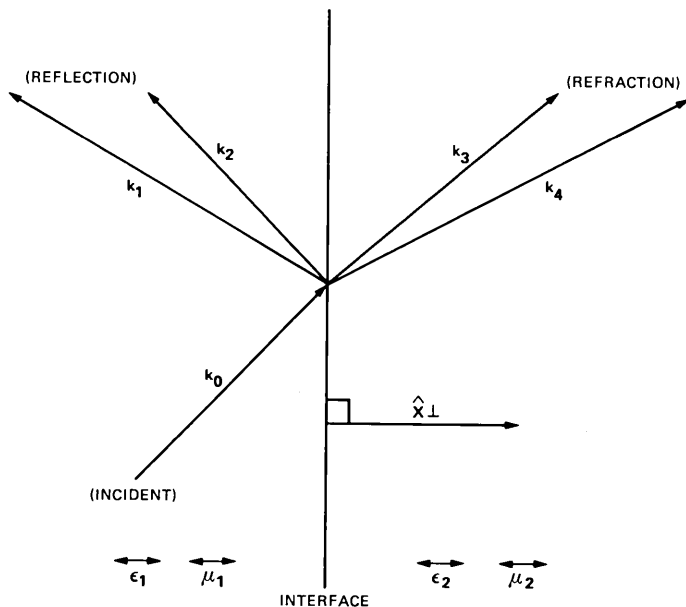


Fig. 1—Scattering at an interface between two anisotropic media.

From (11) and (12), we have

$$-\gamma \times \mathbf{H} = \tilde{\epsilon} \mathbf{E} \quad (58)$$

$$\gamma \times \mathbf{E} = \tilde{\mu} \mathbf{H}. \quad (59)$$

Rearranging, we have

$$-\gamma_{\perp} \hat{x}_{\perp} \times \mathbf{H} = \tilde{\epsilon} \mathbf{E} + \gamma_{\parallel} \times \mathbf{H} \quad (60)$$

$$\gamma_{\perp} \hat{x}_{\perp} \times \mathbf{E} = \tilde{\mu} \mathbf{H} - \gamma_{\parallel} \times \mathbf{E}. \quad (61)$$

Thus, we have a general eigenproblem again:

$$\begin{pmatrix} 0 & 0 & 0 & 0 & \hat{x}_{\perp z} & -\hat{x}_{\perp y} \\ 0 & 0 & 0 & -\hat{x}_{\perp z} & 0 & \hat{x}_{\perp x} \\ 0 & 0 & 0 & \hat{x}_{\perp y} & -\hat{x}_{\perp x} & 0 \\ 0 & -\hat{x}_{\perp z} & \hat{x}_{\perp y} & 0 & 0 & 0 \\ \hat{x}_{\perp z} & 0 & -\hat{x}_{\perp x} & 0 & 0 & 0 \\ -\hat{x}_{\perp y} & \hat{x}_{\perp x} & 0 & 0 & 0 & 0 \end{pmatrix} \mathbf{v} \\ = \gamma_{\perp}^{-1} \left[\tilde{\beta} + \begin{pmatrix} 0 & 0 & 0 & 0 & -\gamma_{\parallel x} & \gamma_{\parallel z} \\ 0 & 0 & 0 & \gamma_{\parallel z} & 0 & -\gamma_{\parallel x} \\ 0 & 0 & 0 & -\gamma_{\parallel y} & \gamma_{\parallel x} & 0 \\ 0 & \gamma_{\parallel z} & -\gamma_{\parallel y} & 0 & 0 & 0 \\ -\gamma_{\parallel z} & 0 & \gamma_{\parallel x} & 0 & 0 & 0 \\ \gamma_{\parallel y} & -\gamma_{\parallel x} & 0 & 0 & 0 & 0 \end{pmatrix} \right] \mathbf{v} \\ \equiv \tilde{\alpha}_{\perp} \mathbf{v} = \gamma_{\perp}^{-1} \tilde{\beta}_{\perp} \mathbf{v}. \quad (62)$$

This eigenproblem has a lot of similarity to (20) in that the matrices on each side of the equation are Hermitian. Further, we expect two extraneous solutions for which the eigenvalues $\gamma_{\perp}^{-1} = 0$ and the eigenvectors

$$\nu_5 = \begin{pmatrix} \hat{x}_{\perp} \\ 0 \end{pmatrix} \quad \text{and} \quad \nu_6 = \begin{pmatrix} 0 \\ \hat{x}_{\perp} \end{pmatrix}, \quad (63)$$

are analogous to (28). We expect two “reflected” solutions with negative

$$\hat{s}_{\perp} \equiv \hat{x}_{\perp} \cdot \hat{s}. \quad (64)$$

The sign of γ_{\perp} is not so relevant because \mathbf{k} and \mathbf{S} are rarely parallel in anisotropic media.

We expect a maximum of two “refracted” solutions when we use $\tilde{\epsilon}_2$ and $\tilde{\mu}_2$ in (62) and look for solutions with positive \hat{s}_{\perp} . We shall have less than the maximum number of refracted solutions when γ_{\parallel} is getting large enough so that $\tilde{\beta}_{\perp}$ ceases to be positive definite.

If $\tilde{\beta}_{\perp}$ is neither positive definite nor negative definite, a derivation similar to (24) does not exist and some of the solutions for γ_{\perp}^{-1} may be complex. If γ_{\perp} is complex, then the corresponding \mathbf{E} and \mathbf{H} fields satisfy from (26):

$$\nu^* \cdot \tilde{\alpha}_{\perp} \nu = 0. \quad (65)$$

Therefore, we have an evanescent solution:

$$\hat{s}_{\perp} = 0. \quad (66)$$

Note that the sign of γ_{\perp} is *not* the criterion for acceptable solutions to (62), rather the sign of \hat{s}_{\perp} is the criterion.

VI. SCATTERING AMPLITUDES

The solution of (62) has provided the values of \mathbf{k}_1 , \mathbf{k}_2 , \mathbf{k}_3 , and \mathbf{k}_4 for a given \mathbf{k}_0 . Let us label the corresponding eigenvectors: ν_1 , ν_2 , ν_3 , ν_4 , and ν_0 . We shall assume no particular normalization for the eigenvectors, but suppose for a given ν_0 there will be particular amplitudes $\alpha_i \nu_i$ for each scattered wave. Naturally, the solutions for the α_i are dependent upon the normalizations of the ν_i .

From Maxwell's eqs. (1) and (2), we must satisfy continuity of the components of \mathbf{E} and \mathbf{H} in the plane of the interface. These conditions may be restated as

$$\tilde{\alpha}_{\perp} \nu_0 = \tilde{\alpha}_{\perp} (-\alpha_1 \nu_1 - \alpha_2 \nu_2 + \alpha_3 \nu_3 + \alpha_4 \nu_4). \quad (67)$$

Equation (67) can be restated as four simultaneous equations by suitable definitions. In the following, assume the index, i , takes on the

integer values 1 through 4. Let

$$b_i \equiv \mathbf{v}_i^* \cdot \tilde{\alpha}_\perp \mathbf{v}_0 \quad (68)$$

$$c_{ij} \equiv \mathbf{v}_i^* \cdot \tilde{\alpha}_\perp \mathbf{v}_j. \quad (69)$$

Then it follows that

$$b_i = \sum_{j=1}^4 c_{ij} a_j. \quad (70)$$

The form of the Hermitian, 4×4 matrix, (c_{ij}) , is simplified somewhat by orthogonality relations:

$$c_{12} = c_{21} = c_{34} = c_{43} = 0. \quad (71)$$

Thus, by solving (70), we obtain the four coupling coefficients, a_i .

VII. RAY TRACING

We envision that our results will find general applicability in problems where "ray-tracing" is to be performed through anisotropic/gyrotropic media and where the relative attenuation of alternative paths is to be explored. We shall indicate how to use the preceding results to this end.

As indicated in the discussion following equation (50), there are difficulties in working directly with the Poynting vector, \mathbf{S} . Even so it is the more macroscopic variable as it is the ray direction, as opposed to \mathbf{k} which depends upon the wavefront normal. Most of the difficulty is resolved if we make the assumption (which does not seem too restrictive in practice) that the initial medium of the ray is to be isotropic (such as air, glass, index matching fluid, etc.).

For isotropic media, the \mathbf{k} direction is identical with the ray direction. It is relatively straightforward to calculate γ_\parallel at the first interface when the initial medium is isotropic. By solving (62) and, subsequently, calculating the corresponding \mathbf{S}_i and, if desired, the amplitudes, a_i , we can decide which of the scattered ray(s) we may wish to trace further.

After we have chosen which scattered wave to follow, we use the Poynting vector to trace the ray to the next interface. We know the \mathbf{k} of this ray and are not faced with the awkward task of reconstructing it from other information. If we are interested in exact phase relationships, these are easy to obtain:

$$\nu(\text{second interface}) = \exp[i(\mathbf{k} \cdot \Delta \mathbf{r})] \nu(\text{first interface}). \quad (72)$$

The spatial displacement from the first to the second interface has been designated $\Delta \mathbf{r}$.

We can calculate the γ_\parallel at the second interface and proceed to solve (62). We calculate the new \mathbf{S}_i of the scattered waves, etc., and choose which one we will follow to the next interface. This process can be

iterated as often as necessary to trace the ray of interest through an arbitrary optical system made up of homogeneous media and interfaces.

VIII. SUMMARY AND CONCLUSIONS

We have developed a general formalism suitable for computation in the analysis of optical propagation through a succession of anisotropic, gyrotropic, homogeneous media. Such problems arise in a large variety of optical devices that are made of materials such as YIG, LiNbO₃, rutile, and calcite.

IX. ACKNOWLEDGMENT

The author is indebted to R. H. Knerr for his continued support and encouragement of this investigation.

APPENDIX

Equivalence of Ray Direction and \hat{s} .

We shall develop a first-order perturbation theory of the general eigenproblem. The result is directly applicable to the calculation of group velocity. When the permeability and permittivity are assumed to be frequency independent, the group velocity must be parallel to the ray velocity.

Suppose we wish to perturb the eigenproblem:

$$\vec{A}\mathbf{v}_i = \lambda_i \vec{B}\mathbf{v}_i, \quad (73)$$

where \vec{A} and \vec{B} are Hermitian. In addition, \vec{B} is positive definite so that a complete set of eigensolutions with real λ_i is expected.

Our perturbation assumption is that the replacement of

$$\vec{A} \rightarrow \vec{A} + \epsilon \vec{A}' \quad (74)$$

requires the corresponding substitutions:

$$\lambda_i \rightarrow \lambda_i + \epsilon \lambda'_i + \dots \quad (75)$$

$$\mathbf{v}_i \rightarrow \mathbf{v}_i + \epsilon \mathbf{v}'_i + \dots \quad (76)$$

Therefore,

$$(\vec{A} + \epsilon \vec{A}')(\mathbf{v}_i + \epsilon \mathbf{v}'_i + \dots) = (\lambda_i + \epsilon \lambda'_i + \dots) \vec{B}(\mathbf{v}_i + \epsilon \mathbf{v}'_i + \dots). \quad (77)$$

Expanding and collecting terms with common powers of ϵ , we obtain for ϵ^0 the original (73); we obtain for ϵ^1 :

$$\vec{A}\mathbf{v}'_i + \vec{A}'\mathbf{v}_i = \lambda_i \vec{B}\mathbf{v}'_i + \lambda'_i \vec{B}\mathbf{v}_i. \quad (78)$$

Taking the dot product with \mathbf{v}_i^* and cancelling terms:

$$\mathbf{v}_i^* \cdot \vec{A}' \mathbf{v}_i = \lambda' \mathbf{v}_i^* \cdot \vec{B} \mathbf{v}_i. \quad (79)$$

Therefore, we can calculate λ'_i from

$$\lambda'_i = \frac{\mathbf{v}_i^* \cdot \vec{A} \mathbf{v}_i}{\mathbf{v}_i^* \cdot \vec{B} \mathbf{v}_i}. \quad (80)$$

The group velocity is calculated by differentiating $\omega(\mathbf{k})$ with respect to the components of \mathbf{k} .¹⁰ The ω dependence is determined from an eigenproblem of the form:

$$\begin{pmatrix} 0 & 0 & 0 & 0 & k_z & -k_y \\ 0 & 0 & 0 & -k_z & 0 & k_x \\ 0 & 0 & 0 & k_y & -k_x & 0 \\ 0 & -k_z & k_y & 0 & 0 & 0 \\ k_z & 0 & -k_x & 0 & 0 & 0 \\ -k_y & k_x & 0 & 0 & 0 & 0 \end{pmatrix} \mathbf{v} = \omega \vec{\beta} \mathbf{v}. \quad (81)$$

Thus, for example, the x -component of the group velocity, v_{gx} is determined from (80) and (81):

$$\begin{aligned} v_{gx} &= \partial\omega/\partial k_x = \frac{1}{2U} \mathbf{v}^* \cdot \begin{pmatrix} 0 & 0 & 0 & 0 & 0 & 0 \\ 0 & 0 & 0 & 0 & 0 & 1 \\ 0 & 0 & 0 & 0 & -1 & 0 \\ 0 & 0 & 0 & 0 & 0 & 0 \\ 0 & 0 & -1 & 0 & 0 & 0 \\ 0 & 1 & 0 & 0 & 0 & 0 \end{pmatrix} \mathbf{v} \\ &= (E_y^* H_z - E_z^* H_y - H_y^* E_z + H_z^* E_y)/2U = S_x/U. \end{aligned} \quad (82)$$

Thus, we have demonstrated:

$$\mathbf{v}_g = \frac{\mathbf{S}}{U} = \mathbf{v}_r. \quad (83)$$

REFERENCES

1. M. Born and E. Wolf, *Principles of Optics*, 5th ed., New York: Pergamon Press, 1975, Chapter 14.
2. B. Lax and K. J. Button, *Microwave Ferrites and Ferrimagnetics*, New York: McGraw-Hill, Chapter 7, 1962.
3. J. F. Dillon, Jr., *J. Appl. Phys.*, **39**, No. 2 (February 1968), p. 922.
4. D. Polder, "On the Theory of Ferromagnetic Resonance," *Phil. Mag.*, **40** (1949), pp. 99-115.
5. R. W. Ditchburn, *Light*, 3rd ed., New York: Academic Press, 1976, p. 463.
6. G. R. Fowles, *Introduction to Modern Optics*, 2nd ed., New York: Holt, Rinehart, and Winston, 1975, pp. 33-7.
7. J. A. Kong, *Proc. IEEE*, **60** (September 1972), p. 1036.
8. R. W. Ditchburn, *Light*, 3rd ed., New York: Academic Press, 1976, p. 575.
9. *Ibid.*, p. 578.
10. E. E. Bergmann, "Comments on Precise Definition of Group Velocity," *Amer. J. Phys.*, **44**, No. 9 (September 1976), p. 890.

A Primal Algorithm for Finding Minimum-Cost Flows in Capacitated Networks With Applications

By C. L. MONMA and M. SEGAL

(Manuscript received December 7, 1981)

Algorithms for finding a minimum-cost, single-commodity flow in a capacitated network are based on variants of the simplex method of linear programming. We describe an implementation of a primal algorithm which is fast and can solve large problems. The major ideas incorporated are (i) the sparsity of the network is used to reduce the time and computer storage space requirements; (ii) basic solutions are stored compactly as spanning trees of the network; (iii) a candidate stack is used to allow flexible strategies in choosing an arc to enter the basis tree; (iv) the predecessor and thread data structures are used to efficiently traverse the tree and to update the solution at each iteration; (v) rules are implemented to avoid cycling or stalling caused by degeneracy; and (vi) piecewise-linear, convex arc costs are handled implicitly. The Primal Network Flow Convex (PNFC) code implements this algorithm and three examples, from communication networks, that can be solved with PNFC are discussed: (i) solving the area transfer problem; (ii) scheduling the collection of traffic data records; and (iii) planning the placement of pair-gain systems.

I. INTRODUCTION

This paper describes an implementation of the network simplex method for solving the transshipment problem. The problem consists of finding a minimum-cost, single-commodity flow in a capacitated network satisfying supply-and-demand constraints. The familiar transportation, assignment, and shortest route problems are all related to the transshipment problem. The area of network-flow theory has been well studied and has proven useful in many areas of applications. (See Refs. 1 to 7.)

A number of different methods have been proposed over the years to solve network-flow problems. These include primal, dual, primal-dual, out-of-kilter, negative-cycle, and scaling methods. A survey of computer codes is presented by Charnes et al.⁸ Until recently, primal-dual approaches were believed to be superior to the others. However, much work has been done involving data structures to reduce the computation time and space requirements for primal-network flow codes. The primal approach is a specialization of the bounded-variable, primal-simplex algorithm of linear programming which takes advantage of the special structure of network problems. We describe an implementation of a primal algorithm that is fast and can solve large problems. The major ideas used are as follows:

(i) The sparsity of the network is used to reduce the time and space requirements for solving network-flow problems.

(ii) Basic solutions are stored compactly as spanning trees of the network.

(iii) A candidate stack is used to allow flexible strategies in choosing an arc to enter the tree.

(iv) The predecessor and thread data structures are used to efficiently traverse the spanning tree and to update the solution at each iteration.

(v) Rules by Cunningham^{9,10} are implemented to avoid cycling or stalling caused by degeneracy.

(vi) Piecewise-linear, convex arc costs (or, equivalently, multiple-parallel arcs) are handled implicitly.

The Primal Network Flow Convex (PNFC) code is an implementation of this algorithm and is described in more detail by Seery.^{11,12} An overview flowchart of the PNFC code is shown in Fig. 1. We will only discuss the INITIAL and SOLVE modules, which perform analogous functions to Phases I and II of the simplex method of linear programming.

The problem of finding a minimum-cost flow in a network with linear costs is described in detail in Section II. The primal network approach is then outlined in Section III. We describe the data structures used to implement the algorithm in Section IV. The major steps of determining an initial solution, finding an entering arc and leaving arc, and exchanging these arcs are detailed in Sections V, VI, VII, and VIII, respectively. Extensions to other than linear arc costs are described in Section IX. Finally, in Section X, we describe three problems in communication networks that can be modeled as network-flow problems:

- (i) Solving the area transfer problem.
- (ii) Scheduling the collection of traffic data records.
- (iii) Planning the placements of pair-gain devices.

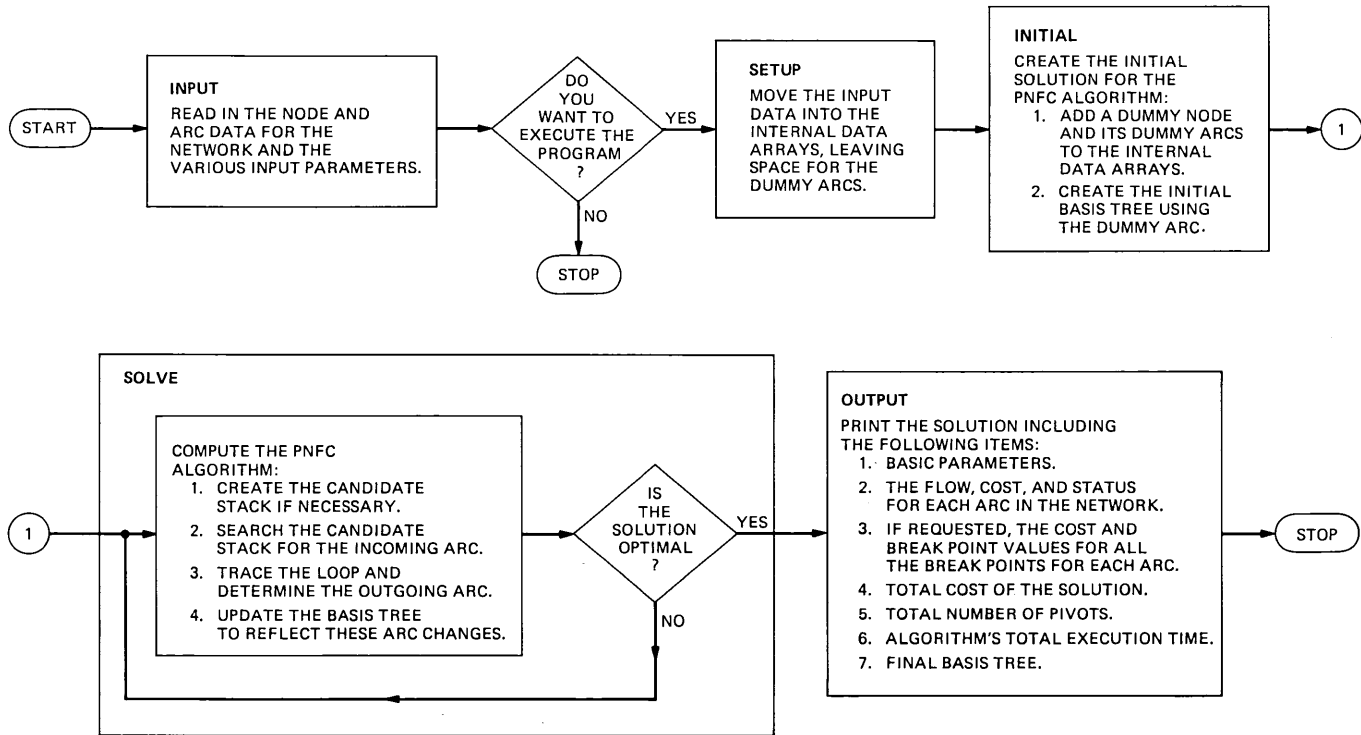


Fig. 1—Overview of the PNFC program.

II. PROBLEM FORMULATION

We refer the reader to Harary¹³ for graph-theoretic concepts necessary for defining the problem; however, we do define a few of these concepts here. Consider a directed graph $G = (N, A)$ consisting of a set N of nodes and a set A of ordered pairs of nodes called arcs. Associated with each node i is a value d_i , representing the amount of supply of a commodity available at the node. A negative "supply" represents a demand for the commodity at the node. Each arc (i, j) has a lower bound a_{ij} and upper bound b_{ij} on the number of units of the commodity that is allowed to flow along the arc from node i to node j . Also, there is a shipping cost of c_{ij} per unit of flow along each arc (i, j) . An example network is shown in Fig. 2, with each node i labeled by d_i , and each arc (i, j) labeled by (arc no. a_{ij}, b_{ij}, c_{ij}). A feasible flow $x = (x_{ij})$ assigns flow values x_{ij} to arcs (i, j) which satisfy the conservation-of-flow constraints eq. (2) and the capacity requirements eq. (3). An example of feasible flow for the network in Fig. 2 is shown in Fig. 3, where each arc is labeled by its flow value. The

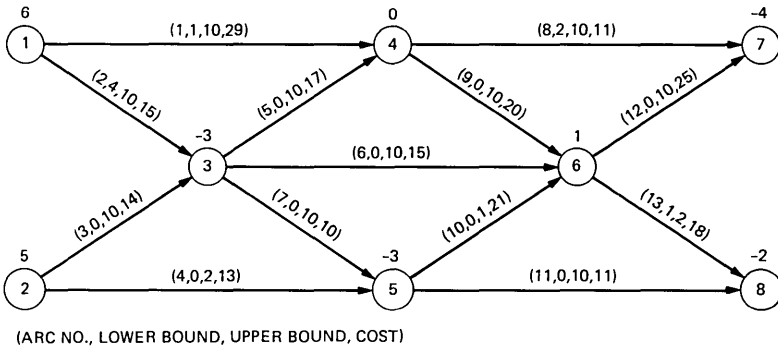


Fig. 2—Network.

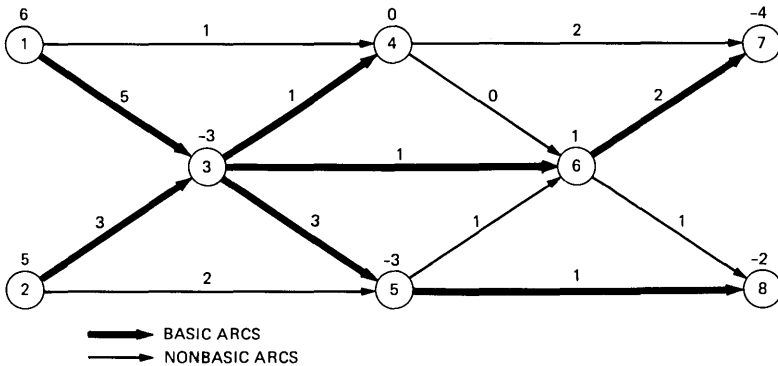


Fig. 3—Feasible flow.

objective is to find a feasible flow that minimizes the total cost of eq. (1). This problem corresponds to the following Primal Linear Program (PLP): Minimize

$$\sum_{i,j:(i,j) \in A} c_{ij} x_{ij} \quad (1)$$

subject to

$$\sum_{j:(i,j) \in A} x_{ij} - \sum_{k:(k,i) \in A} x_{ki} = d_i \quad i \in N \quad (2)$$

$$a_{ij} \leq x_{ij} \leq b_{ij} \quad (i, j) \in A. \quad (3)$$

The summations are taken only over existing arcs. This emphasizes the fact that sparsity of the network is exploited by only storing data for arcs that are present in the network and only performing operations on these arcs.

We do, of course, allow multiple (or parallel) arcs between nodes i and j . These arcs can each be given explicitly with associated costs and bounds and would be treated as distinct arcs. In Section IX, we describe how the implementation of this algorithm handles parallel arcs implicitly.

It is well known that PLP can be reformulated with either all supply values equal to zero or all lower bounds equal to zero. However, since some problems are formulated naturally in one way and some in the other way, we allow both the supply and lower-bound values to be nonzero.

We assume that the network is connected. If not, the problem decomposes into independent subproblems on the connected components. We make this assumption merely to simplify the discussion. In fact, the algorithm described here converts the given network into a connected one by appending a dummy node and dummy arcs as part of obtaining an initial feasible solution.

III. PRIMAL NETWORK ALGORITHM

The primal-simplex algorithm of linear programming was specialized to the transshipment problem by Dantzig³. It leads to the "stepping-stone" approach as described by Charnes and Cooper.¹ This approach was generally believed to be computationally inferior to the existing primal-dual methods. However, recent work on primal network approaches has taken advantage of data structures to streamline the calculations involved and reduce the storage requirement. In this section, we outline the major facts related to the application of the primal-simplex approach to network problems. A more complete analysis is provided by Bradley et al.¹⁴

3.1 Basic solutions

The primal network algorithm is a specialization of the bounded-variable, simplex method. This allows the capacity constraints eq. (3) to be handled implicitly in the computations. The remaining constraints eq. (2) can be written in matrix notation as $Ax = d$, where A is the node-arc incidence matrix for the network and d is the vector of supply values. A solution x to eq. (2) is called basic if the columns of A associated with the variables x_{ij} , which are strictly between their bounds, are linearly independent. The value of the basic variables are uniquely determined once the nonbasic variables have been specified to be equal to their lower or upper bounds. Basic solutions correspond to the bases of the column space of A . Also, the feasible basic solutions are exactly the extreme points of the polyhedron described by eqs. (2) and (3). Hence, for any (linear) objective function eq. (1), some basic solution is optimal.

Each column of A corresponds to an arc in the network. Therefore, since the network is connected, the basic solutions correspond to subsets of arcs that form spanning trees in the network; the remaining arcs have flow values that are restricted to their lower or upper bound. The darker arcs in Fig. 3 form a basis tree.

3.2 Optimality criteria

Assign dual variables (or node potentials) u_i to each constraint in eq. (2), and variables v_{ij} and w_{ij} to each lower- and upper-bound constraint, respectively, in eq. (3). The Dual Linear Program (DLP) for PLP is defined as follows: Maximize

$$\sum_{i \in N} d_i u_i + \sum_{(i,j) \in A} a_{ij} v_{ij} - \sum_{(i,j) \in A} b_{ij} w_{ij} \quad (4)$$

subject to

$$u_i - u_j + v_{ij} - w_{ij} \leq c_{ij} \quad (i, j) \in A \quad (5)$$

$$v_{ij}, w_{ij} \geq 0 \quad (i, j) \in A. \quad (6)$$

Using linear programming duality theory, the complementary slackness conditions that optimal solutions to PLP and DLP must satisfy are given by

$$x_{ij}(c_{ij} - u_i + u_j - v_{ij} + w_{ij}) = 0, \quad (7)$$

and

$$v_{ij}(x_{ij} - a_{ij}) = 0, \quad (8)$$

$$w_{ij}(b_{ij} - x_{ij}) = 0. \quad (9)$$

By defining the reduced cost of an arc (i, j) to be

$$\bar{c}_{ij} = c_{ij} - u_i + u_j, \quad (10)$$

the optimality conditions for a pair of primal and dual solutions become

$$\text{if } a_{ij} < x_{ij} < b_{ij} \text{ then } \bar{c}_{ij} = 0, \quad (11)$$

$$\text{if } x_{ij} = a_{ij} \text{ then } \bar{c}_{ij} \geq 0, \quad (12)$$

and

$$\text{if } x_{ij} = b_{ij} \text{ then } \bar{c}_{ij} \leq 0. \quad (13)$$

3.3 Basis exchange

Consider a basic feasible solution x^* for PLP. The *node potentials* u^* are determined using eq. (11) for the basic arcs; these values are uniquely determined once any one node potential value is fixed. If eqs. (12) and (13) are satisfied, then the optimality of the solutions x^* and u^* follows from their feasibility and complementary slackness. Otherwise, an entering (nonbasic) arc and a leaving (basic) arc are identified and exchanged to obtain a new basic solution. This process is repeated until optimality is reached.

A nonbasic arc that violates eq. (12) or (13) is selected to enter the basis; that is, arc (i, j) is chosen if

$$x_{ij} = a_{ij} \text{ and } \bar{c}_{ij} < 0, \text{ or}$$

$$x_{ij} = b_{ij} \text{ and } \bar{c}_{ij} > 0.$$

The entering arc forms a unique cycle (or loop) when added to the basis tree. By interpreting $u_i - u_j$ to be the cost of sending one unit of flow from node j to node i , using arcs only in the basis tree, $\bar{c}_{ij} < 0$ implies that increasing the flow along arc (i, j) and sending this flow around the loop from j back to i will strictly decrease the cost. [This is true also when decreasing the flow on arc (i, j) when $\bar{c}_{ij} > 0$.] Since this conserves the flow at each node, the amount of flow change on the loop is limited only by the capacity constraints on the arcs of the loop. One of the arcs whose flow reaches its bound first is selected to leave the basis. For example, increasing the flow on the nonbasic arc (4, 7) in Fig. 3 increases the flow on arc (3, 4) and decreases the flow on arcs (3, 6) and (6, 7). Arc (3, 6) reaches its bound first. Exchanging arcs (4, 7) and (3, 6) forms the new basis tree shown in Fig. 4.

IV. DATA STRUCTURES

The contemporary work on network algorithms has focused on using data structures to improve the effectiveness of primal network codes. Since network problems are typically sparse, with many node pairs having no arcs between them, we only store the data and perform

Table I—Data for the network of Fig. 2

Arc	1	2	3	4	5	6	7	8	9	10	11	12	13
Lower Bound	1	4	0	0	0	0	0	2	0	0	0	0	1
Upper Bound	10	10	10	2	10	10	10	10	10	1	10	10	2
Cost	29	15	14	13	17	15	10	11	20	21	11	25	18

calculations for the arcs actually present in the network. The arcs are stored in a list, with all of the arcs pointing out of a node grouped together. The costs and bounds are kept in similar arc-length lists. This is illustrated in Table I for the network in Fig. 2.

The representation of a basis as a tree results in a compact format for storing the relevant data. This format is shown in Table II for the basis tree in Fig. 4. A basis tree is specified by identifying one node to be the root node and indicating a predecessor NPRED(*i*) for each node *i*, which is the next node after *i* on the unique path from *i* to the root node in the tree. The physical direction of the arc between *i* and NPRED(*i*) is distinguished by setting NDIRECT(*i*) equal to 1 if the arc points from *i* to NPRED(*i*) and to -1 otherwise. The variable DUALV(*i*) is the dual variable associated with each node *i*. The amount of flow on the arc between *i* and NPRED(*i*) is given by FLOW(*i*).

The loop formed by an entering nonbasic arc (*i*, *j*) and the basis tree can be traced, in one pass, by following the predecessor paths from *i* and *j* back towards the root until these paths meet. The depth NDEPTH(*i*) of a node *i* is the number of nodes on the path from *i* to the root. The predecessor and depth arrays are used to proceed up

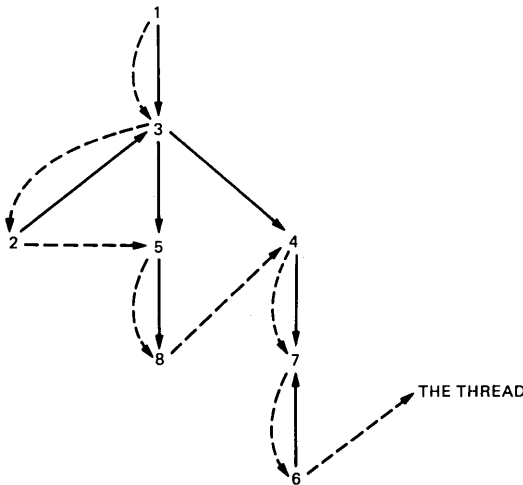


Fig. 4—Basis tree.

Table IIa—Data structures for the basis tree of Fig. 4—node data

Node	1	2	3	4	5	6	7	8
NPRED	0	3	1	3	3	7	4	5
NDIRECT	0	1	-1	-1	-1	1	-1	-1
DUALV	0	1	15	32	25	18	43	36
FLOW	0	3	5	2	3	1	3	1
NDEPTH	1	3	2	3	3	5	4	4
LTHRED	3	5	2	7	8	0	6	4

Table IIb—Data structure for the basis tree of Fig. 4—arc data

Arc	1	2	3	4	5	6	7	8	9	10	11	12	13
KASE	0	-1	-1	1	-1	0	-1	-1	0	1	-1	-1	0

these paths, staying at the same depth on each path so that the search ends at the node where the paths meet, thus forming a loop.

After the entering and leaving arcs have been determined, it is necessary to update the basis tree. This involves traversing all of the successors of a node to update their dual variable and depth values. A useful tool for doing this is the “thread.” The thread $LTHRED(i)$ of a node i labels the nodes of the tree in “preorder” according to the following recursive rule: First label the root. Then label the nodes in each of the subtrees belonging to the immediate successors of the root in preorder. (The order in which these subtrees are visited is immaterial.) The thread is illustrated by dotted arcs in Fig. 4.

A final data structure keeps track of the status of each arc. The array $KASE(LN)$ is set to 0 if arc LN is currently nonbasic at its lower bound, 1 if it is nonbasic at its upper bound, and -1 if it is basic.

These data structures are illustrated in Tables IIa and IIb for the basic solution in Fig. 4, with node 1 as the root.

V. INITIAL SOLUTION

The primal network-flow algorithm proceeds from one basic solution to another until an optimal solution is found. It is necessary to provide an initial feasible solution to begin this iterative process. Several methods are available for obtaining initial feasible solutions.¹⁴ We use the “Big-M” method of artificially creating a feasible flow by adding a dummy node and dummy arcs. This method is easy to implement and understand, and works well.¹⁵

The method begins by initialing the flow in all arcs to be at their lower bounds, that is, all arcs are nonbasic at their lower bound and the KASE array is set to zero. This induces a net supply at each node i with value

$$SPLYNT(i) = d_i - \sum_{j:(i,j) \in A} a_{ij} + \sum_{k:(k,i) \in A} a_{ki}.$$

For the network in Fig. 2, the values are shown in Table III. A feasible flow is formed by adding a dummy node as the root of the tree and dummy arcs between the dummy node and all the other nodes. These dummy arcs form the basis tree. The direction of the dummy arc in the tree is towards the root if the net supply of the node is nonnegative, and away from the root otherwise. The amount of flow is equal to the absolute value of the net supply of the node. The cost of the dummy arcs is set to be very large if the dummy arc points away from the root and is set to zero otherwise. The dummy arcs have a lower bound of zero and an upper bound of "infinity." The dual values are calculated by setting the dual variable for the root to zero and solving for the others using eq. (11). The initial basis tree for the example network in Fig. 2 is shown in Fig. 5 with basis array data in Table IV. Later stages of the algorithm serve to remove the dummy arcs from the basis. If the algorithm terminates with positive flow in a dummy arc, then there is no feasible solution to the original problem.

VI. ENTERING ARC

Suitable candidates for arcs to enter the basis are nonbasic arcs (i, j) , which are either at their lower bound with negative reduced cost, or at their upper bound with positive reduced cost, i.e., eq. (12) or eq. (13) is violated. Many strategies have been proposed and tested for

Table III—Values of the net supply for the network in Fig. 2

Node	1	2	3	4	5	6	7	8
SPLYNT	1	5	1	-1	-3	0	-2	-1

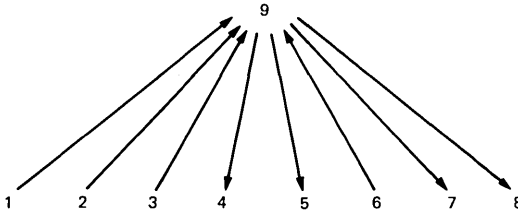


Fig. 5—Initial basis tree.

Table IV—Initial basis tree

Node	1	2	3	4	5	6	7	8	9
NPRED	9	9	9	9	9	9	9	9	0
NDIRECT	1	1	1	-1	-1	1	-1	-1	0
DUALV	0	0	0	∞	∞	0	∞	∞	0
FLOW	1	5	1	1	3	0	2	1	0
NDEPTH	2	2	2	2	2	2	2	2	1
LTHRED	2	3	4	5	6	7	8	0	1

selecting an arc to enter the basis; these range from choosing the first violating arc to choosing the most violating arc. We use a candidate stack approach^{14,16} which allows flexible strategies in controlling the choice of an incoming arc.

The usage of the candidate stack is illustrated in Fig. 6. The candidate stack is replenished during a major iteration whenever it is empty or when an upper bound MXITER on the number of consecutive minor iterations is reached. The stack is filled from the arc list which has all of the arcs out of a node grouped together. The reduced costs are computed for the arcs out of a node i , and the nonbasic arc (i, j) , with the largest violation (if any) among these, is placed on the stack. This is repeated for nodes $i + 1, i + 2, \text{etc.}$, until either all nodes have been processed or the stack has reached its maximum allowable size of MXSTAK. The next major iteration begins with the node where the last major iteration left off. This periodic examination of all arcs helps prevent "stalling," which is a long sequence of pivot exchanges that does not improve the cost of the solution.¹⁰

Once the stack has been formed in a major iteration, minor iterations are performed to choose the nonbasic arcs from the stack with the largest violation to enter the basis. At each minor iteration, the arcs on the stack are checked for violations. If an arc no longer has a violation, it is removed from the stack. Once the stack becomes empty, or MXITER consecutive minor iterations are performed, the stack is rebuilt in a major iteration.

VII. LEAVING ARC

A nonbasic arc to enter the basis tree is chosen because it violates eq. (12) or (13). This implies that moving its flow value away from its bound and updating the flow values of the arcs on the newly formed

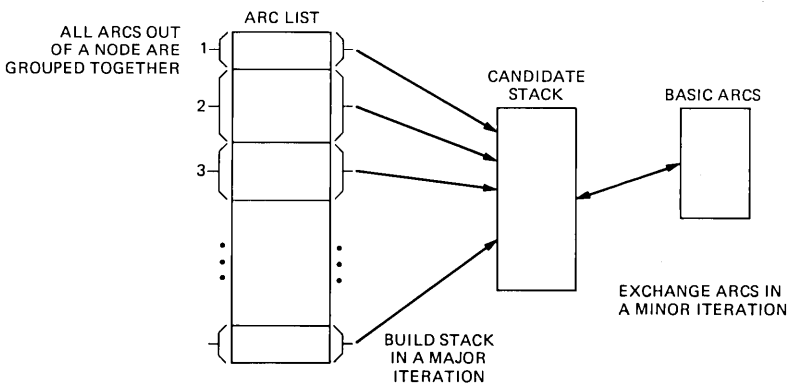


Fig. 6—Candidate stack.

loop strictly decreases the cost of the current solution. The flow is changed as much as possible until one of the arcs on the loop reaches its bound and is chosen to leave the basic solution. This is accomplished in one pass by tracing the loop using the predecessor and depth arrays.

To illustrate this, consider the basis tree in Fig. 4 with arc (6, 8) chosen as the entering arc. Arc (6, 8) can have its flow increased by one unit before reaching its upper bound. This induces a supply at node 8 and a demand at node 6. The path on the side of the loop with the induced supply is called the plus path, and the other side is called the negative path. The predecessor array is used to trace the paths from 6 and 8 towards the root, until the loop is formed where the paths join at node 3. Along the way, the amount of change in the flow value before an arc reaches its bounds is computed for each arc on the loop. The depth array is used to alternatively move up each of the two paths checking for a common node. The arcs in Fig. 4 are examined in the order (6, 7), (5, 8), (4, 7), (3, 5), and (3, 4); their maximum amount of change in flow before reaching a bound is 1, 1, 7, 7, and 8, respectively. Hence, arcs (6, 7), (5, 8), and the entering arc (6, 8) all reach their bound after a flow change of one unit. Any of these arcs could be chosen to leave the basis.

In our algorithm, the leaving arc is chosen by using Cunningham's rule⁹ which is designed to avoid "cycling" caused by degeneracy. This approach hinges upon maintaining basis trees that are "strongly" feasible; that is, the arcs in the basis tree directed towards the root are required to have flow values strictly less than their upper bounds, and arcs directed away from the root have flow values strictly greater than their lower bounds. This assures us that a positive amount of flow can always be pushed up the tree. We note that the initial solution procedure always constructs a strongly feasible tree and that the tree in Fig. 3 is strongly feasible.

In the case of a tie among several arcs as candidates to leave the basis, the choice is made using the following priority: First, choose the candidate arc which is closest to the root on the plus path (if any). Next, choose the entering arc, if it is a candidate. Finally, choose the arc on the negative path furthest from the root. In the example cited above, arc (6, 7) would be chosen. This rule provides the only choice which will result in the new basis tree remaining strongly feasible.

VIII. BASIS EXCHANGE

Exchanging the entering and leaving arcs requires updating the basic solution. For example, choosing arc (1, 4) to enter the basis tree in Fig. 4 results in the choice of arc (1, 3) to leave the basis. This forms a new basis tree as illustrated in Fig. 7. This changes the data arrays associated with the basic solution. Specifically, the nodes on the loop

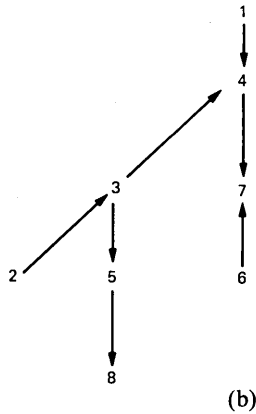
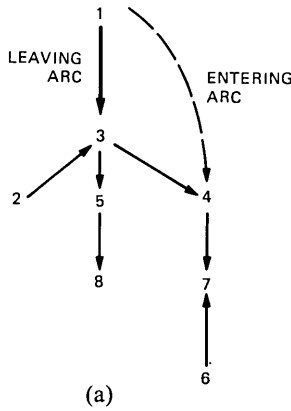


Fig. 7—Basis exchange. (a) Old basis tree. (b) New basis tree.

must be traced (as described before) to update the predecessor, direction, flow, and thread array (NPRED, NDIRECT, FLOW, and LTHRED) values. In the example, nodes 1, 3, and 4 are on the loop. In addition, the dual variable and depth array (DUALV and NDEPTH) values must be updated for the nodes in the subtree which is moved because of the basis exchange. In our example, the subtree moved is rooted at node 3 and consists of nodes 2, 3, 4, 5, 6, 7, and 8. The thread array LTHRED is used to identify the nodes in the subtree rooted at a node i as follows:

(i) Label the root node i to indicate that it is in the subtree. Let $j = \text{LTHRED}(i)$.

(ii) If $\text{PRED}(j)$ is labeled, then label j , and set $j = \text{LTHRED}(j)$, or stop with all nodes in the subtree labeled as such.

This procedure works because the nodes in the subtree appear

consecutively on the thread immediately after the root, and because the predecessor of a node always appears on the thread before the node itself does. The method used to update the basic solution values is an enhancement of a procedure described in detail by Jacobsen.¹⁷ The change in status of the entering and leaving arcs is reflected by updating their values in the KASE array. The new array values for the basic solution of Fig. 7 are shown in Table V. The optimality of this solution may be checked by noting that the flow and dual variables are feasible to PLP and DLP, respectively, and the complementary slackness conditions eqs. (11), (12), and (13) hold.

IX. EXTENSION TO OTHER COSTS

We have described an algorithm for finding a minimum cost flow in a capacitated network with linear costs. The current implementation actually handles piecewise-linear, convex costs or, equivalently, multiple parallel arcs between two nodes. We describe how this is accomplished implicitly without any additional work required.

Consider the piecewise-linear, convex arc cost shown in Fig. 8. It consists of three line segments with cost slopes equal to c_1 , c_2 , and c_3 , respectively. The lower bound on the allowable flow is b_0 , with three *break points* of b_1 , b_2 , and b_3 . This is equivalent to having three parallel

Table V—Data structure for the new basis tree of Fig. 7

Node	1	2	3	4	5	6	7	8
NPRED	0	3	4	1	3	7	4	5
NDIRECT	0	1	1	-1	-1	1	-1	-1
DUALV	0	-2	12	29	22	15	40	33
FLOW	0	3	1	2	3	1	3	1
NDEPTH	1	4	3	2	4	4	3	5
LTHRED	4	5	2	3	8	0	6	7

Arc Data													
Arc	1	2	3	4	5	6	7	8	9	10	11	12	13
KASE	-1	0	-1	1	-1	0	-1	-1	0	1	-1	-1	0

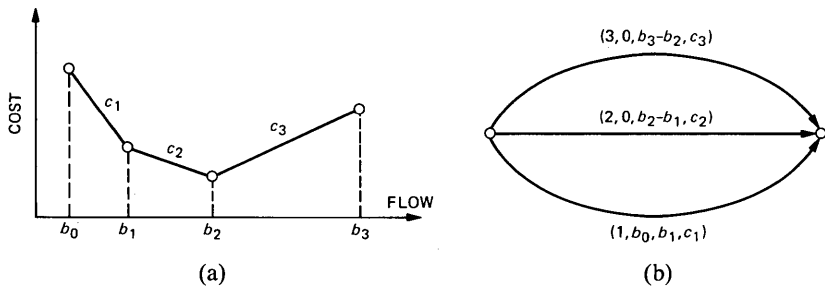


Fig. 8—Piecewise-linear, convex arc cost and equivalent parallel arc formulation.

arcs (one for each line segment) as shown in Fig. 8, with arcs labeled by arc no., lower bound, upper bound, and cost.

This situation can be handled implicitly by expanding the definition of the status of an arc LN as follows:

$KASE(LN)$

$$= \begin{cases} k & \text{if arc } LN \text{ is nonbasic with flow value } b_k \\ -k & \text{if arc } LN \text{ is basic with flow value between } b_{k-1} \text{ and } b_k \end{cases}$$

For this case, convexity and separability guarantees that at most one arc of each parallel arc group will be basic; therefore, we can now proceed with the algorithm as if only one arc exists between the nodes. The appropriate cost and bound values to use for this arc depend only on the status of the arc.

This feature is also useful for problems with convex arc costs. We can always approximate a convex cost function by a piecewise-linear, convex cost function as shown in Fig. 9. This can be used to obtain approximate solutions. Meyer's alternative method¹⁸ approximates the convex cost by a piecewise-linear, convex cost, with only two line segments whose breakpoints vary from one iteration to the next. Meyer's approach is guaranteed to converge to the optimal solution.

Concave arc costs model economies of scale and are discussed by Erickson et al.,¹⁹ where a dynamic programming solution procedure is proposed. An alternative method of solution is to use a branch-and-bound approach, solving the subproblems using a linear approximation to the concave cost. Such an approach has been applied successfully for fixed-charge transportation problems by Barr et al.²⁰

X. APPLICATIONS

Numerous applications of network-flow models can be found in the references provided. We briefly describe three applications in communication systems.

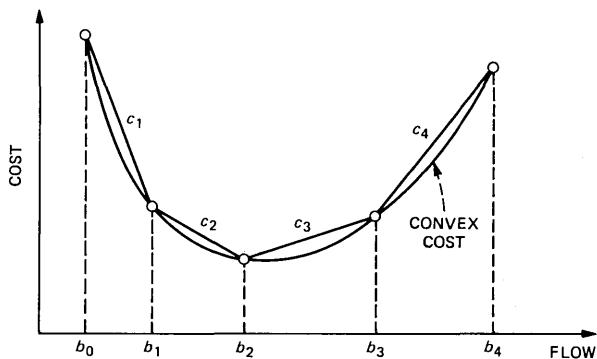


Fig. 9—Piecewise-linear approximation of a convex cost function.

Our first example illustrates a situation where piecewise-linear, convex arc costs arise in a natural way. Hammer and Segal²¹ formulated a model for handling "area transfers" in a local area. The area is subdivided into districts j which are served by wire centers i . Currently, w_{ij} working lines (or wire pairs) are in use between i and j , with additional s_{ij} spare lines unused. We let

$$d_j = \sum_i w_{ij}$$

represent the current demand at district j . Future demand for lines at district j can be satisfied from wire center i by using the spare lines at a cost of λ_{ij} per line or adding additional lines beyond the available spare at a larger cost of $\lambda_{ij} + \delta_{ij}$. Alternatively, an area transfer may occur if a wire center i 's capacity b_i on the number of lines it can serve is exceeded. This involves disconnecting a line from wire center i to district j at a cost of μ_{ij} per line and reconnecting it to another wire center. Given new demands $d_j + \Delta_j$ for lines at each district j , the problem of assigning customers to wire centers (with possible area transfers) at minimum total cost is a transportation problem with a piecewise-linear, convex cost structure for each i, j pair as shown in Fig. 10. The slope of the three line segments and the break points are indicated on the figure. Denote by x_{ij} the change in the line assignments between wire centers i and districts j , and by $c_{ij}(x_{ij})$ the separable, piecewise-linear cost functions of Fig. 10. Then, the problem is to minimize

$$\sum_i \sum_j c_{ij}(x_{ij}) \tag{14}$$

subject to

$$\left. \begin{aligned} \sum_i (w_{ij} + x_{ij}) &= d_j + \Delta_j & \forall j \\ \sum_j (w_{ij} + x_{ij}) &\leq b_i & \forall i \end{aligned} \right\} \tag{15}$$

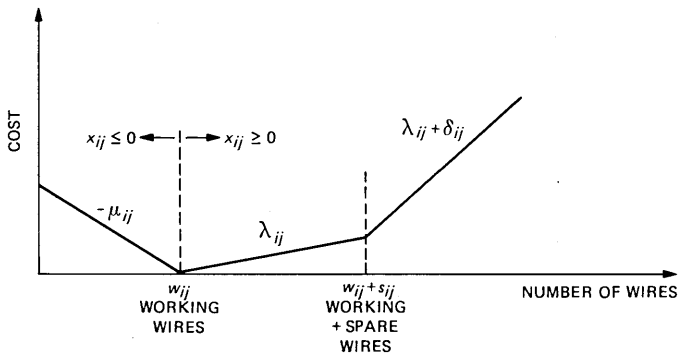


Fig. 10—Piecewise-linear, convex cost structure for the area transfer model.

$$-w_{ij} \leq x_{ij} \quad \forall_{i,j}. \quad (16)$$

In general, this formulation fits transportation models in which convex costs are incurred whenever one perturbs (increases or decreases) the established pattern of the distribution (w_{ij}). A project scheduling problem is formulated by Lawler⁵ as a network-flow problem with two piecewise-linear, convex cost segments.

A second example involves scheduling the collection of call records in private communication networks and is discussed in detail by Monma and Segal.²² A private communication network consists of tie trunks interconnecting various locations. Calls between two locations overflow to the toll network when all connecting tie trunks are busy. Each location is served by a Private Branch Exchange (PBX) which generates a call record for each call originating at its location.

A central PBX is equipped with several ports, each capable of simultaneously collecting records from different locations. According to a prescribed schedule, the central PBX initiates calls and begins transferring call records. This continues until all records stored at the start of the polling have been collected.

We describe a network-flow model used to find a good polling schedule by illustrating it in Fig. 11 for two offices (PBXs) and 48 polling periods in the day. Each period J is represented by a node J on the right side of the figure. Each office I is represented by a collection of 48 nodes arranged in a particular configuration as shown on the left side of the figure. Each node J in the configuration for office I represents the period J at the office. The arc directed horizontally into this node J indicates that a known number of records are generated during period J at office I . The arc directed from a period J to a following period $J + 1$ node signifies records in storage at the end of period J which are carried over to the start of period $J + 1$. We note that the records left in storage at the end of the last period in the day carry over to the first period of the following day.

The arc directed from the period J node of office I to the period J node on the right side of the figure indicates the polling of records from office I at the start of period J . The arc directed from the period J node to the sink node represents all of the records polled in period J among all offices. The arrow out of the sink node means that all records generated must be polled at some time during the day.

Capacities on the arcs depend on the amount of call-record storage space available at each office and the polling capacity of the ports at the central PBX. The cost per record for polling office I during period J depends on the probability that a call from the central PBX to office I will overflow to the toll network and the cost of such a call. This network-flow model is used in an interactive way to produce polling schedules (which are determined from the flows on the arcs from

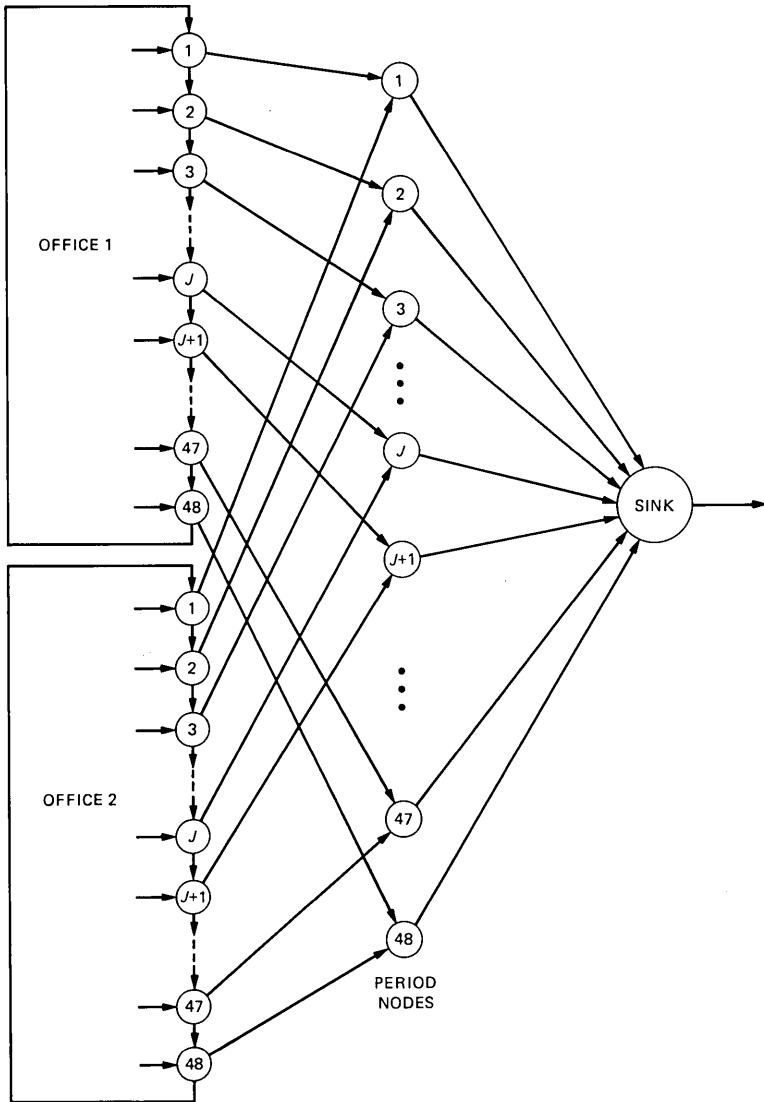


Fig. 11—Network-flow model for polling call records with two offices and 48 periods.

period J office I nodes to period J nodes) of minimum cost which avoid losing call records. (Call records may be lost if a PBX generates them faster than they are polled, thus, overflowing the storage capacity of the PBX.)

Our final example involves a capacity-expansion problem in the local network, which connects subscribers to the local switching office. Elken²³ discusses a mathematical programming formulation of this

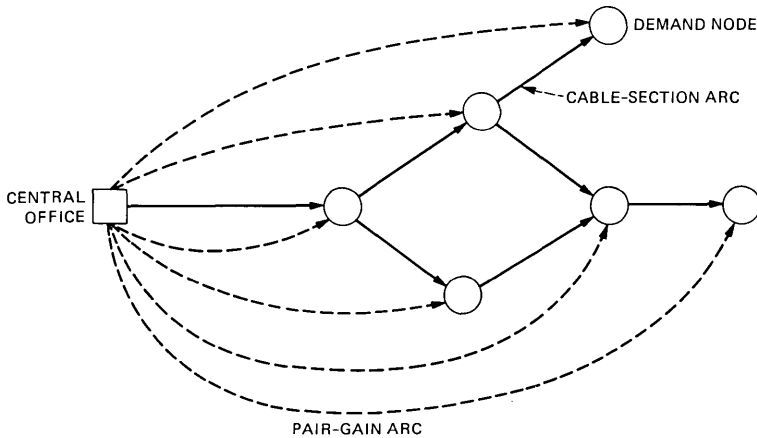


Fig. 12—Network-flow models for placement of pair-gain devices.

problem. We will describe a network-flow model by way of a stylized and simplified example. The network is composed of cable sections which connect pairs of nodes (see Fig. 12). The nodes represent demand points for groups of subscribers. The solid arcs represent cable sections. Each cable section may consist of several parallel existing or proposed cables of various sizes (and costs). The dashed arcs represent the possible placement of pair-gain systems (in which a small number of wire pairs are used to serve a larger number of customers by means of multiplexing or concentration). The piecewise-linear, convex costs arise from the multiple parallel cables in each cable section. A solution to the problem represents a least-cost expansion of cables and placement of pair-gain systems.

Finally, we mention some computational experience with the PNFC computer code. Elken²⁴ solved several examples of the previously described local network problem with about 50 nodes, 150 arcs, and 2 piecewise-linear sections. The average CPU time was 1.5 seconds. The scheduling of the call-records problem was solved hundreds of times for problems with about 500 nodes and 1000 arcs and required an average of 3.5 seconds. The largest example tested was a 400-node assignment problem with 40,000 arcs; this problem was solved in about 80 seconds of CPU time on the IBM Amdahl computer.

XI. ACKNOWLEDGMENT

We would like to thank A. T. Seery for an excellent job of programming and testing the PNFC.

REFERENCES

1. A. Charnes and W. W. Cooper, *Management Models and Industrial Applications of Linear Programming, I and II*, New York: John Wiley, 1961.

2. L. R. Ford and D. R. Fulkerson, *Flows in Networks*, Princeton, New Jersey: Princeton University Press, 1962.
3. G. B. Dantzig, *Linear Programming and Extensions*, Princeton, New Jersey: Princeton University Press, 1965.
4. G. H. Bradley, "Survey of Deterministic Networks," *AIEE Trans.*, 7, No. 3 (September 1975), pp. 222-34.
5. E. L. Lawler, *Combinatorial Optimization: Networks and Matroids*, New York: Holt, Rinehart, and Winston, 1976.
6. B. L. Golden and T. L. Magnanti, "Deterministic Network Optimization: A Bibliography," *Networks*, 7, No. 2 (Summer 1977), pp. 149-83.
7. P. A. Jensen and J. W. Barnes, *Network Flow Programming*, New York: John Wiley, 1980.
8. A. Charnes et al., "Past, Present, and Future of Large-Scale Transshipment Computer Codes and Applications," *Computers and Operations Res.*, 2, No. 2 (September 1975), pp. 71-81.
9. W. H. Cunningham, "A Network Simplex Method," *Math. Prog.*, 11, No. 2 (October 1976), pp. 105-16.
10. W. H. Cunningham, "Theoretical Properties of the Network Simplex Method," *Math. of Operations Res.*, 4, No. 2 (May 1979), pp. 196-208.
11. A. T. Seery, unpublished work.
12. *Ibid.*
13. F. Harary, *Graph Theory*, Reading, Massachusetts: Addison-Wesley, 1969.
14. G. H. Bradley, G. G. Brown, and G. W. Graves, "Design and Implementation of Large-Scale Primal Transshipment Algorithms," *Man. Sci.*, 24, No. 1 (September 1977), pp. 1-34.
15. J. M. Mulvey, "Testing of a Large-Scale Network Optimization Program," *Math. Prog.*, 15, No. 3 (November 1978), pp. 291-314.
16. J. M. Mulvey, "Pivot Strategies for Primal-Simplex Network Codes," *J. Assn. Computing Mach.*, 25, No. 2 (April 1978), pp. 266-70.
17. S. K. Jacobsen, "On the Use of Tree-Indexing in Transportation Algorithms," *Eur. J. Operational Res.*, 2, No. 1 (January 1978), pp. 54-65.
18. R. R. Meyer, "Two-Segment Separable Programming," *Man. Sci.*, 25, No. 4 (April 1979), pp. 385-95.
19. R. E. Erickson, C. L. Monma, and A. F. Veinott, Jr., unpublished work.
20. R. S. Barr, F. Glover, and D. Klingman, "A New Optimization Method for Large-Scale Fixed Charge Transportation Problems," *Operations Res.*, 29, No. 3 (May-June 1981), pp. 448-63.
21. P. L. Hammer and M. Segal, unpublished work.
22. C. L. Monma and M. Segal, unpublished work.
23. T. R. Elken, "The Application of Mathematical Programming to Loop Feeder Allocation," *B.S.T.J.*, 59, No. 4 (April 1980), pp. 479-500.
24. T. R. Elken, personal communication.

Improved Reconstruction of DPCM-Coded Pictures

By A. N. NETRAVALI and E. G. BOWEN

(Manuscript received August 21, 1981)

A new scheme for the reconstruction of DPCM-coded signals is presented. In this scheme, instead of assigning one representative level to the prediction error whenever it is in a range determined by the decision levels of a DPCM quantizer, surrounding local picture structure is used to improve the reconstruction. No extra transmission is required. Mean-absolute-reconstruction error is decreased by over 20 percent, and the picture quality is significantly improved in flat, as well as high, detailed areas of still pictures and sequences of pictures containing motion.

I. INTRODUCTION

In most picture communication systems that employ any type of quantized encoding, samples are sequentially encoded, transmitted by the channel and reproduced at the receiver. Pulse-Code Modulation (PCM) systems assign one of the many quantization levels to the amplitude of each sample, whereas differential pulse-code modulation (DPCM) systems assign a quantizer level to the prediction error of each sample.¹ Thus, in PCM systems, no use of the correlation between the adjacent picture samples is made either at the transmitter for coding or at the receivers for display. In DPCM, the "previously" coded sample values are used for computing the prediction of the "present" sample at the transmitter, and thus correlation of the present element with the previous pels is utilized. However, no use of the "future" samples is made at the transmitter or at the receiver.

In this paper, we present techniques for coding and display that use correlation between the present sample, and its past and future neighbors. At the transmitter, this improves the prediction; and at the receiver, this results in a more accurate reproduction of the intensity for display. The technique can be used at the receiver, or at the

transmitter, or both. For example, its use only at the receiver amounts to postprocessing of the coded data received from a standard DPCM transmitter. Each sample that is DPCM coded with a coarse quantizer is known at the receiver to be in a range that is determined by the prediction and the coarseness of the quantizer. Knowing the ranges of surrounding neighboring samples, a new representative value can be assigned to each sample.

We describe a technique for such an assignment and give results of computer simulations on still pictures, as well as a sequence of frames containing motion. Simulations show that in areas containing high-spatial correlation, improvement using our technique is the greatest. In DPCM systems, this corresponds to samples whose prediction error occupies the "inner" (close to zero) levels of the quantizer. Coarseness of the quantizer in these areas shows as granular noise, which is reduced by our technique. However, this reduction occurs without the blurring of high-detailed areas associated, for example, with low-pass filtering. Comparison of the quality of the pictures shows that edge busyness and slope overload are also reduced, but this improvement is not reflected proportionately in the mean-square-reconstruction error.

II. ALGORITHM

In the basic DPCM system, a prediction of the present sample (e.g., sample X in Fig. 1) is made from the previously encoded information that is already transmitted to the receiver. Thus, in Fig. 1, the intensity of pel X can be predicted by \hat{A} , or $(\hat{A} + \hat{D})/2$, where \hat{A} and \hat{D} are the reconstructed values of samples A and D . The error resulting from the subtraction of the prediction from the actual value of pel X is quantized into a set of discrete amplitude levels. Thus, a quantized form of $(X - \hat{A})$ may be sent if the so-called previous element predictor is used. The quantizer levels are represented as binary words of either fixed or variable length and sent to the channel for transmission. If the prediction error, e , falls within the two consecutive decision levels e_1 , and e_2 , then the receiver knows the intensity of the sample to be within the

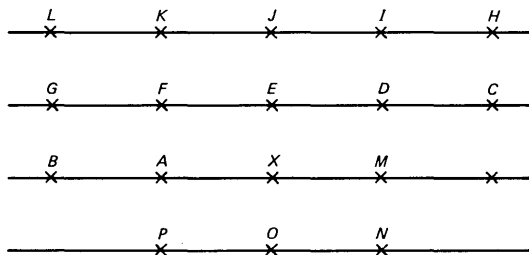


Fig. 1—Pel configuration for intraframe processing.

range $[(P + e_1), (P + e_2)]$, where P is the prediction value. Traditionally, a representative level e_r , is chosen to represent e in the range $[e_1 e_2]$ and the reconstruction at the receiver is taken to be $(P + e_r)$. Such a reconstruction is based on the representative level e_r , which is chosen to minimize certain average error.^{2,3,4} However, pictures are highly nonhomogeneous and nonstationary; therefore, benefit can be derived by choosing a representative level based on the local characteristics of the picture. However, if no additional information is transmitted to the receiver, the local characteristics have to be estimated based on the quantized information. The problem then is to estimate the intensity of pel X ,

(i) knowing that it is in the range $[P + e_1, P + e_2]$ and

(ii) knowing the ranges of the surrounding correlated elements, such as A, M, F, E, D, P, O, N , etc.

Since elements A, M, \dots, N are correlated with element X , their range information should give a better estimate of the pel intensity at X . Since an accurate model for the picture signal does not yet exist, we could not apply estimation theory. Instead, we tried several intuitively reasonable techniques, and the following appears to be the best for the set of pictures used. The following steps are used in the reconstruction algorithm.

1. Use a set of predetermined surrounding elements, e.g., A, M, F, E, D, P, O , and N .

2. Determine the normal (i.e., using a standard DPCM receiver) reconstructed value for X , and the surrounding elements.

3. Knowing p , the prediction of X , determine the range for X , i.e., $[p + e_1, p + e_2]$, in addition to its normal reconstructed value $p + e_r$.

4. Let n and m be the number of surrounding elements having normal reconstructed value less than and more than $(p + e_r)$, respectively. Then, the new reconstruction for element X is*

$$\begin{aligned} \hat{X} &= \frac{n(p + e_1) + m(p + e_r)}{(n + m)}, & \text{if } n > m \\ &= \frac{n(p + e_r) + m(p + e_2)}{(n + m)} & \text{if } n < m \\ &= p + (e_1 + e_2)/2 & \text{if } n = m. \end{aligned}$$

Thus, the new reconstruction is a weighted sum of the endpoints of the range, where the weights are determined by the surrounding elements. Since the new reconstruction maintains the value of the

* If n is close to m and changes slightly from sample to sample, the above reconstruction may show jumps from sample to sample. This provides a dithering effect that appears to improve the picture quality.

element X within the range $[P + e_1, P + e_2]$, the filtering action of the weighted averaging process does not blur the edges significantly. It is possible to choose the "surrounding" elements that have characteristics similar to the element X , so that the averaging does not produce any noticeable artifact.

The algorithm described above is primarily for postprocessing at the receiver for better reconstruction. It is also possible to use the algorithm for preprocessing at the transmitter. In traditional DPCM, reconstructed values are used for prediction. Therefore, it is possible to use only the previously transmitted pels to improve the reconstruction and then use this better-reconstructed value for prediction. The constraint that only previously transmitted values can be used for improved reconstruction limits the improvement when intraframe predictors are used. As an example, if previous element A is used for prediction of X , then better reconstruction of A can be performed by using only surrounding transmitted neighboring pels, such as B, E, F, A , etc. Since other neighbors, such as elements X, P , and O cannot be used, smaller improvement in reconstruction is obtained. However, in the case of frame-to-frame coding, substantial improvement is possible. For example, in Fig. 2, previous frame element, \bar{X} , can be reconstructed using all the elements in the 3×3 neighborhood, since they would be available at the receiver at the time of coding present element X .

III. SIMULATION RESULTS

We performed computer simulations to evaluate the improvements using our reconstruction techniques. The still frames used were 256×256 pel arrays with each pel quantized to 8 bits (levels 0 to 255). These are shown in Figs. 3 and 4. The sequence of frames containing motion, consists of 64 frames called "JUDY." Four frames from this sequence are shown in Fig. 4 of Ref. 5. For simulation with still frames, two predictors, A (previous element), $(A + D)/2$ (planar, two dimensional) were used. Three symmetric, even-level quantizers were used. Their positive decision levels are given below:

$$Q_1 : 0, 10, 255, \quad 4 \text{ levels.}$$

$$Q_2 : 0, 3, 9, 29, 255, \quad 8 \text{ levels.}$$

$$Q_3 : 0, 10, 25, 43, 255, \quad 8 \text{ levels.}$$

The mean-absolute-reconstruction error (i.e., the magnitude of the difference between the original and the reconstructed picture) was calculated for both pictures with standard DPCM and the improved DPCM described in the previous section. As mentioned before, since the intraframe coding does not allow significant improvements at the transmitter using our techniques, only postprocessing at the receiver

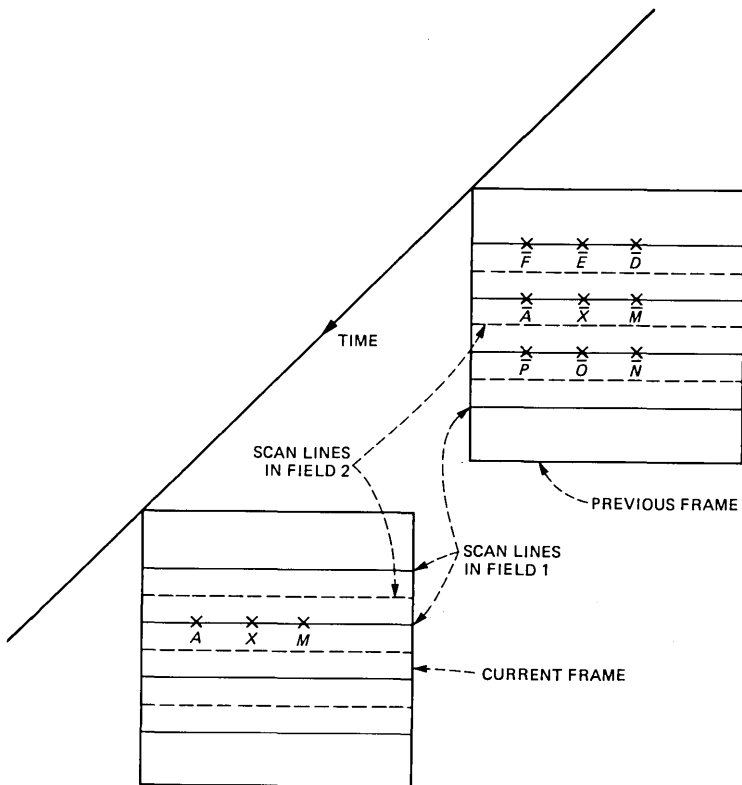


Fig. 2—Pel configuration for interframe processing.

was performed. Three cases were considered, depending on the number of neighbors used. Case 1 used three neighbors, *A*, *X*, and *M*; Case 2 used five neighbors, *A*, *X*, *M*, *E*, and *O*; and Case 3 used nine neighbors, *A*, *X*, *M*, *F*, *E*, *D*, *P*, *O*, and *N*. Tables I and II show the mean-absolute-reconstruction error for various cases. We note that a larger number of neighbors improves the performance of our postprocessing techniques. Large improvements in mean-absolute error are obtained for quantizers that have coarse inner levels. Thus, when quantizers Q_1 and Q_3 are used, we get about 20 percent improvement over the standard DPCM. Although the mean absolute error does not show improvement with quantizer Q_2 , the quality of the picture is improved considerably because of improved reconstruction of the low-contrast areas, as well as edges.

Quantizers for intraframe predictive coders usually contain fine inner levels to reduce the visible granular noise in flat areas. If only a small number of levels can be used, then one has to trade off granular noise for other distortions such as edge busyness. It may be possible

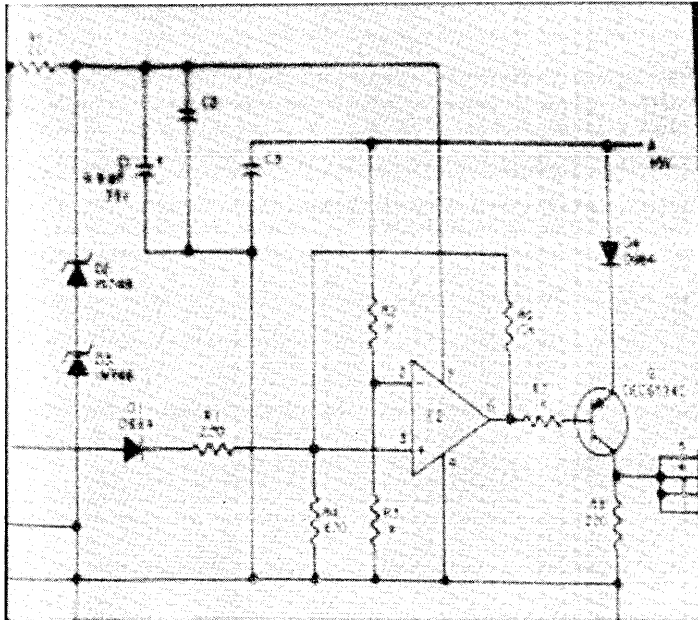


Fig. 3—Circuit diagram used for simulation.



Fig. 4—Checked girl used for simulation.

with our technique to use a quantizer with coarse inner levels so that better edge reproduction is possible, since granular noise would be mitigated to a large extent.

Simulations of our scheme for a sequence of frames involved an improved DPCM transmitter, as well as receiver. Thus, referring to Fig. 2, three types of schemes were simulated. In the first, conditional replenishment with previous frame predictor (i.e., \bar{X} for prediction of X) and a moving area threshold of 2 (out of 255) was simulated. This

Table I—Comparison of mean-absolute error for circuit diagram

		Number of Neighbors = 3		Number of Neighbors = 5		Number of Neighbors = 9	
		Predictor Used					
		A	$\frac{A + D}{2}$	A	$\frac{A + D}{2}$	A	$\frac{A + D}{2}$
Quantizer used: Q_1	Standard DPCM	5.77	4.81	5.77	4.81	5.77	4.81
	Improved DPCM	5.84	4.92	5.07	4.08	4.87	3.94
Quantizer used: Q_2	Standard DPCM	3.13	2.31	3.13	2.31	3.13	2.31
	Improved DPCM	3.18	2.72	3.07	2.45	3.01	2.40
Quantizer used: Q_3	Standard DPCM	2.92	3.09	2.92	3.09	2.92	3.09
	Improved DPCM	2.95	3.01	2.35	2.20	2.07	2.08

Table II—Comparison of mean-absolute error for checkered girl

		Number of Neighbors = 3		Number of Neighbors = 5		Number of Neighbors = 9	
		Predictor Used					
		A	$\frac{A + D}{2}$	A	$\frac{A + D}{2}$	A	$\frac{A + D}{2}$
Quantizer used: Q_1	Standard DPCM	5.73	3.74	5.73	3.74	5.73	3.74
	Improved DPCM	5.72	3.78	5.21	3.17	5.07	3.13
Quantizer used: Q_2	Standard DPCM	2.96	1.71	2.96	1.71	2.96	1.71
	Improved DPCM	3.04	1.98	2.95	1.79	2.94	1.80
Quantizer used: Q_3	Standard DPCM	2.96	2.79	2.96	2.79	2.96	2.79
	Improved DPCM	3.24	2.80	2.96	2.20	2.44	2.20

was used for comparison. The second scheme was identical to the first, except that the reconstruction of X was done by using the 3×3 neighborhood only when X was a moving area pel. If X is not a moving area pel, then it is reconstructed by using its previous frame value. Thus, only postprocessing at the receiver is used. The third scheme used an improved reconstruction value from the previous frame also for prediction. All three schemes used quantizer Q_3 . The results are shown in Figs. 5, 6, and 7. Figure 5 shows the mean-absolute-reconstruction error averaged over all the pels as a function of the frame number. It is easy to see that there is about 20 percent reduction in mean-absolute error because of the improved reconstruction (scheme 2). Also, the improved prediction and reconstruction (i.e., scheme 3) reduces the error further by about 10 percent. Figure 6 shows the improvement when restricted to moving area pels. Since the number of moving area pels differs for the three schemes, total reconstruction error is shown. Considerable improvement is now seen by postprocessing alone and pre- and postprocessing. The total prediction error for all the moving area pels for schemes 1 and 3 are plotted in Fig. 7. Thus, instead of using \bar{X} for prediction as in scheme 1, if we improved the

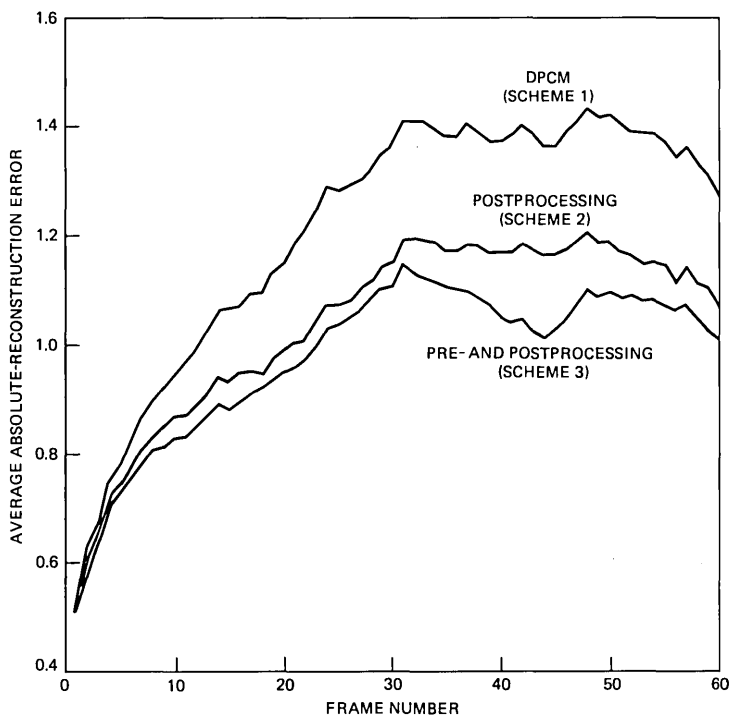


Fig. 5—A plot of the mean-absolute-reconstruction error as a function of the frame number.

predictor using the 3×3 surrounding elements around \bar{X} , the prediction is improved by over 15 to 20 percent. However, much of this improvement is apparently included in only postprocessing with no change in predictor (scheme 2). The pictures produced by the three schemes were viewed in informal sessions. It was concluded that the "dirty window" effect in moving areas associated with coarse quantization (scheme 1) was removed to a large extent by improved post-processing (scheme 2). In many cases, the blur in areas of high-contrast edge motion, resulting from a quantizer with insufficient dynamic

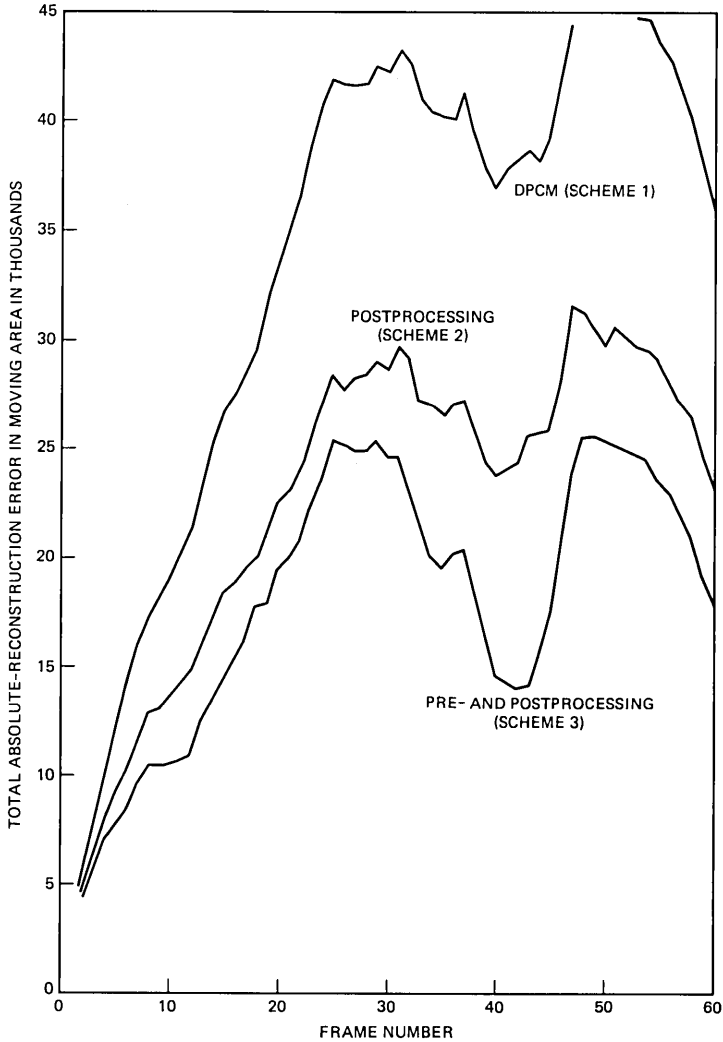


Fig. 6—A plot of the total error in the moving area versus the frame number.

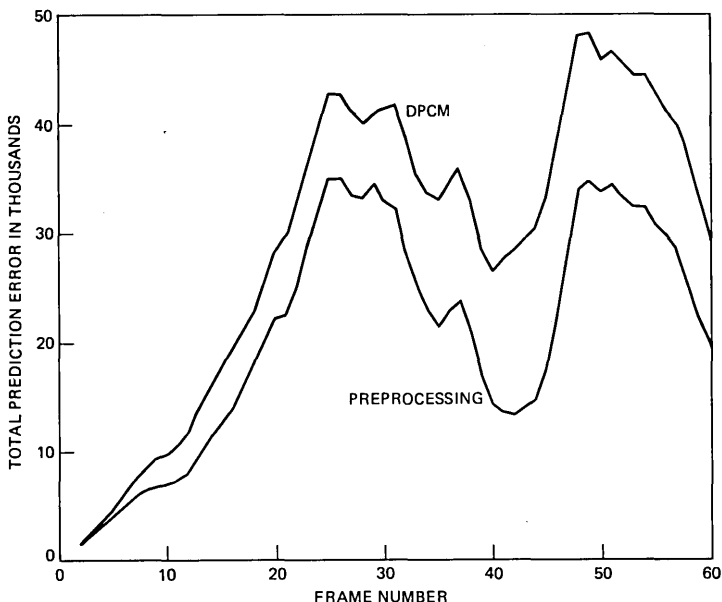


Fig. 7—A plot of the total absolute-prediction error as a function of the frame number.

range, was also reduced. Although the results are not shown when quantizer Q_2 was used, we found that there was improvement in absolute-reconstruction error, and the picture quality showed significant improvements.

IV. SUMMARY AND CONCLUSIONS

We have presented a new method for reconstruction of DPCM-coded samples. Instead of using one representative level whenever the prediction error is within a range, we use local properties of the picture signal to derive an improved reconstruction. No extra transmission is required. Reconstruction error is decreased by over 20 percent, and picture quality is improved significantly. It is possible to use quantizers that have coarse inner levels and to use our techniques to reduce the visible granular noise. Therefore, quantizers with fewer levels can be used. Improvement is obtained for coding of still frames, as well as sequence of frames containing motion.

V. ACKNOWLEDGMENTS

The authors would like to thank N. S. Jayant and P. Pirsch for comments on an earlier draft.

REFERENCES

1. A. N. Netravali and J. O. Limb, "Picture Coding: A Review," Proc. IEEE, 68 (March 1980), pp. 366-406.
2. J. Max, "Quantizing for Minimum Distortion," IEEE Trans. Inform. Theory, IT-6 (March 1980), pp. 7-12.
3. D. K. Sharma and A. N. Netravali, "Design of Quantizers for DPCM Coding of Pictures," IEEE Trans. Commun., Com-25 (November 1978), pp. 1267-74.
4. P. Pirsch, "Design of DPCM Quantizers for Video Signals Using Subjective Tests," IEEE Trans. Commun., 29 (July 1981), pp. 990-1000.
5. A. N. Netravali and J. D. Robbins, "Motion Compensated Television Coding," B.S.T.J., 58, No. 3, Part I (March 1979), pp. 631-70.

An Improved Training Procedure for Connected-Digit Recognition

By L. R. RABINER, A. BERGH, and J. G. WILPON

The "conventional" way of obtaining word reference patterns for connected-word recognition systems is to use isolated-word patterns, and to rely on the dynamics of the matching algorithm to account for the differences in connected speech. Connected-word recognition, based on such an approach, tends to become unreliable (high-error rates) when the talking rate becomes grossly incommensurate with the rate at which the isolated-word training patterns were spoken. To alleviate this problem, an improved training procedure for connected-word (digit) recognition is proposed in which word reference patterns from isolated occurrences of the vocabulary words are combined with word reference patterns extracted from within connected-word strings to give a robust, reliable word recognizer over all normal speaking rates. The manner in which the embedded-word patterns are extracted was carefully studied, and it is shown that the robust training procedure of Rabiner and Wilpon can be used to give reliable patterns for the embedded, as well as the isolated, patterns. In a test of the system (as a speaker-trained, connected-digit recognizer) with 18 talkers, each speaking 40 different strings (of variable length from 2 to 5 digits), median-string error rates of 0 and 2.5 percent were obtained for deliberately spoken strings and naturally spoken strings, respectively, when the string length was known. Using only isolated-word training tokens, the comparable error rates were 10 and 11.3 percent, respectively.

I. INTRODUCTION

Recently, several algorithms for recognizing a connected string of words based on a set of discrete word reference patterns have been proposed.¹⁻⁵ Although the details and the implementations of each of these algorithms differ substantially, basically they all try to find the optimum (smallest distance) concatenation of isolated-word reference patterns that best matches the spoken word string. Thus, the success

of all these algorithms hinges on how well a connected string of words can be matched by concatenating members of a set of isolated-word reference patterns. Clearly, for talking rates that are comparable to the rate of articulation of isolated words [e.g., on the order of 100 words per minute (wpm)], these algorithms have the potential of performing quite accurately.¹⁻⁶ However, when the talking rates of the connected-word strings become substantially larger than the articulation rate for isolated words, for example, around 150 wpm, then all the pattern-matching algorithms tend to become unreliable (yield high-error rates). The breakdown mechanism is easily understood in such cases. The first effect of a higher talking rate is a shortening of the duration of the word within the connected-word string. This shortening is highly nonlinear (i.e., vowels and steady fricatives are first shortened and then they are reduced, whereas sound transitions are substantially unaffected) and is not easily compensated by the dynamic time warping (DTW) alignment procedure, which has its own inherent local and global warping path constraints. The second pronounced effect is the sound coarticulation that occurs at the boundaries between words in the string. As the talking rate increases, the amount of coarticulation increases to the point where the isolated-word reference patterns no longer adequately match the words in the sequence, especially at the beginning and end of words.

The above discussion emphasizes the fact that the currently available connected-word recognition systems are inadequate for most reasonable talking rates; i.e., only a highly motivated talker who spoke the connected-word strings in a careful, deliberate manner, would achieve high accuracy. The next question then is what can be done to increase the reliability of the connected-word recognizer at normal talking rates? The answer to this question is the topic of this paper. The proposed solution is an improved training procedure in which the isolated-word reference patterns are supplemented with word reference patterns extracted from connected-word strings. Although there has been no publication on the use of embedded word training patterns for connected-word recognition, the Nippon Electric Company's DP-100 training procedure has, in demonstrations, used embedded digits, obtained as the middle digit of three-digit strings, to supplement the isolated digits in the training set.^{7,8}

The purpose of this paper is to show how word reference patterns for a connected-word recognizer can be obtained in a reliable and robust manner from connected-word strings. We also show how such embedded training patterns can be combined with standard isolated-word reference patterns to provide a training set which is capable of recognizing connected-word strings spoken at normal talking rates. In particular, we consider recognition of connected-digit strings of from

two to five digits. It is shown that in a speaker-trained test, the connected-digit recognizer achieved a 97.5 percent median-string accuracy on normally spoken digit strings using the improved training set, whereas an 88.7 percent median-string accuracy was obtained using only isolated-digit templates.

The outline of this paper is as follows. In Section II, we describe the improved training procedure and discuss the important issue of how to extract an embedded-word reference pattern that is reliable and robust. In Section III, we describe and give the results of an experiment to independently evaluate the automatic training procedure of Section II. In Section IV, we present results of a connected-digit recognition test using 18 talkers, each of whom used the improved training procedure. Finally, in Section V, we summarize our results, and discuss alternative procedures for improving the connected-digit recognition algorithm.

II. THE IMPROVED CONNECTED-WORD TRAINING PROCEDURE

To understand the improved connected-word training procedure, we must first review briefly our current implementation of the connected-word recognizer. Thus, we will focus on the level-building (LB) algorithm of Myers and Rabiner,^{5,6,9} as this is the algorithm for which all results will be given.

2.1 Connected-word recognition using a LB approach

Assume we are given a test string $\mathbf{T} = \mathbf{T}(m)$, $m = 1, 2, \dots, M$, where \mathbf{T} represents a string of words of unknown length. The connected-word-recognition problem consists of finding the sequence of reference patterns, $\mathbf{R}^s = \mathbf{R}_{q(1)} \circledast \mathbf{R}_{q(2)} \circledast \dots \circledast \mathbf{R}_{q(L)}$ of arbitrary length L which best matches (minimum distance) the test string \mathbf{T} . (The operation \circledast is a concatenation operator). The sequence \mathbf{R}^s defines the L reference patterns, $\mathbf{R}_{q(1)}, \mathbf{R}_{q(2)}, \dots, \mathbf{R}_{q(L)}$, which, when concatenated, best matches (over all lengths L and over all possible reference patterns) the unknown test sequence \mathbf{T} .

The basic procedure for finding \mathbf{R}^s is to solve a time-alignment problem between \mathbf{T} and \mathbf{R}^s using DTW methods. The LB algorithm is basically an efficient procedure for solving the associated DTW minimization.^{5,6} Although the details of the exact procedure need not be reviewed here, there are several important properties of the LB algorithm that will be used in this paper. Therefore, we first enumerate these properties, which include:

(i) The LB algorithm finds the optimum matching string of every length, L words, from $L = 1$ to $L = \text{LMAX}$ (as set by the user).

(ii) For each string match found by the LB algorithm, a segmentation of the test string into appropriate matching regions for each

word in the string is provided. (We will rely on this property to formulate the embedded training procedure).

(iii) For every string length, L words, a list of the best Q strings (i.e., the Q lowest distance L -word strings) can be obtained.

(iv) By using the flexible parameters of the LB algorithm, namely δ_{R_1} (a range of frames at the beginning of a reference pattern which can be skipped), δ_{R_2} (a range of frames at the end of a reference pattern which can be skipped), and δ_{END} (a range of frames at the end of the test that can be skipped), modifications of the reference patterns, or, equivalently, large discrete jumps in the warping path, can be made to partially account for word-boundary and word-shortening effects.

Figures 1 and 2 summarize the above properties in a fairly concise manner. Figure 1 shows a sequence of DTW paths corresponding to the best L -word sequence, the best $L-1$ word sequence, etc. For the best L -word sequence, the segmentation points corresponding to the bound-

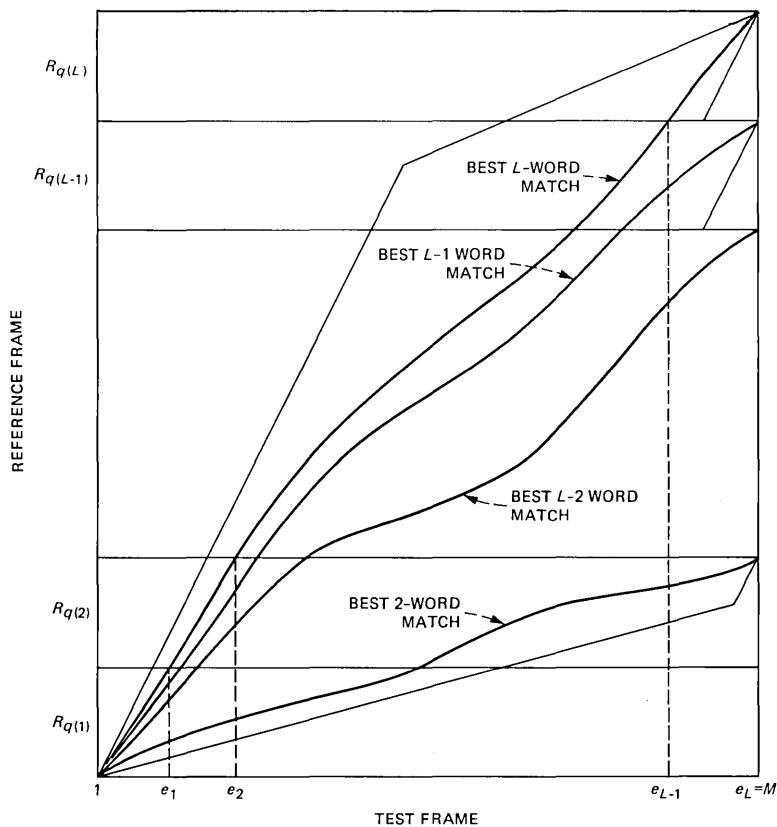


Fig. 1—Sequence of LB DTW warps to provide best word sequences of several different lengths.

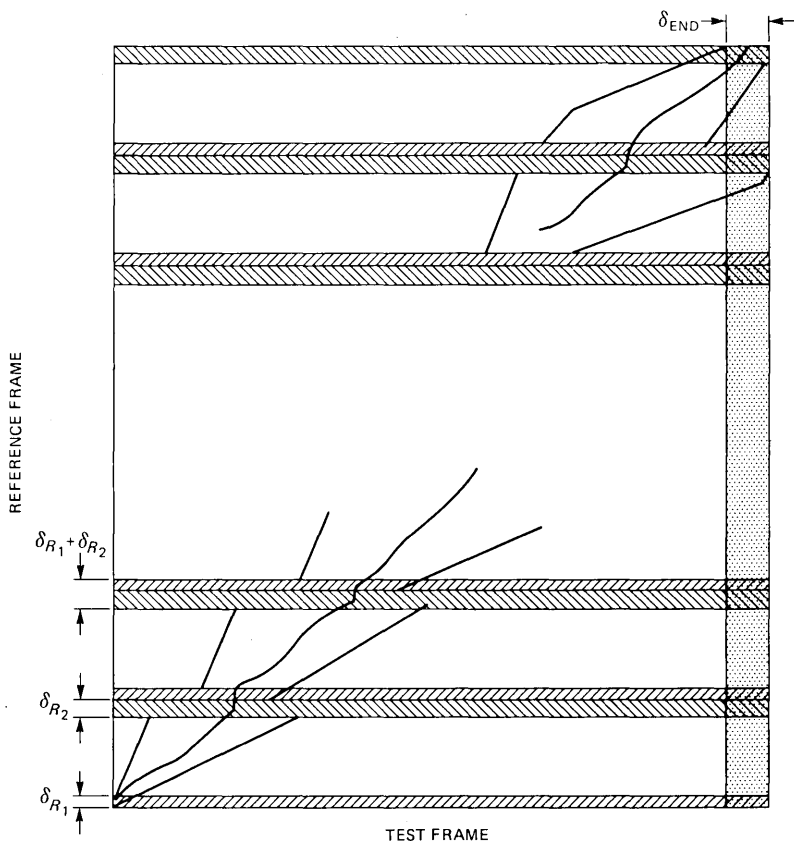


Fig. 2—Summary of flexible LB parameters.

aries of each of the L words in the test string are also shown. It should be clear that the best string of length q need not (and generally won't) contain the same words as the best string of length $q + 1$.

Figure 2 shows a summary of how the LB parameters δ_{R_1} , δ_{R_2} , and δ_{END} can affect the warping path. It shows that the DTW path can literally jump over up to $(\delta_{R_2} + \delta_{R_1})$ frames of the pattern R^s at each discrete word boundary within R^s . In this manner, a certain degree of word coarticulation and word shortening can be directly accounted for in obtaining the best matches to the test pattern. It has been shown previously^{6,7} that judicious use of the LB parameters greatly improves the performance of the LB algorithm for several connected-word recognition tasks.

2.2 Isolated-word training for connected-word recognition

The "standard" reference set for the LB algorithm for speaker-trained use is the set of isolated-word patterns obtained via the robust

training procedure of Rabiner and Wilpon.¹⁰ Thus, for each word in the vocabulary, a single-reference token was obtained as the time-warped average of two versions of the word which was deemed sufficiently similar (based on the recognizer-distance measure).

As discussed previously, the major disadvantage of isolated-word reference patterns is that when the talking rate of the test strings becomes much higher than the talking rate of the isolated-word patterns, reliability and accuracy of the connected-word recognizer fall dramatically. To alleviate this problem, we now describe the embedded-word training procedure.

2.3 Embedded-word training for connected-word recognition

The basic idea behind the embedded-word training procedure is that an "improved" set of word reference patterns could be obtained by combining the isolated-word reference patterns with word reference patterns extracted from actual connected-word strings. A second important and related problem is deciding from which strings (i.e., which sequence of words) such patterns should be extracted. Finally, a third related problem is controlling the rate at which the talker speaks the strings from which the embedded words are extracted.

Before describing the training procedure that was studied, it is worthwhile discussing the three points made above. The first point is perhaps the most fundamental one. In connected-word sequences, it is often difficult, if not impossible, to assign boundaries to words in the string. For example, in the sequence /one-nine/, the nasal boundary between the one and the nine is a shared boundary and can arbitrarily be assigned to either digit. As the rate of talking goes up, this problem generally is compounded.

The second problem in implementing an embedded-word training procedure, namely, the choice of strings from which to extract the patterns, involves deciding whether or not to use strings with heavy word coarticulation. (Clearly, this problem is intimately related to the first problem.) For example, the string /616/ will provide a markedly different embedded digit one from the string /219/. Which of these sequences would provide the most useful output, in terms of providing an improved reference pattern for the digit 1, is unclear, and is a topic of investigation in Section III.

The third problem, namely, the talking rate of the talker, again determines the difficulty in extracting the embedded-reference pattern. We will see later in this section that it is reasonable to consider both deliberate (i.e., careful articulation of words) and natural (i.e., normal articulation of words) talking rates for extraction of reference words, and that different analysis procedures should be applied in both cases.

Based on the above discussion, a block diagram of the embedded-

reference word training procedure is given in Fig. 3. The philosophy of the training procedure is similar to that of the robust training procedure for isolated words.¹⁰ For each word in the vocabulary, a sequence generator (i.e., a talker) produces a string of words in which the desired word appears. The choice of word sequences will be discussed below. A DTW alignment procedure matches a set of concatenated word references, corresponding to the words in the string, to the test string T , thereby providing a segmentation of T . The pattern for the appropriate reference word is extracted from T , based on the segmentation, and stored in a temporary word store. It is then compared to all previous occurrences of that word in the store, using another DTW alignment procedure. For each such comparison, a distance score is obtained. If any distance score falls below a specified threshold, then the pair of tokens giving the minimum distance among all versions in the store are averaged, after time alignment, and the resulting reference pattern is saved in an embedded-word store. This procedure is iterated until an embedded pattern is obtained for each word in the vocabulary.

The only unspecified aspect of the embedded-training procedure is the word sequence generator. Since we have tested the improved training procedure only on digit sequences, we will focus our attention solely on this vocabulary. We have considered two sequence generators—a noncoarticulated (NC) sequence generator, and a coarticulated (CO) sequence generator. For both cases, the desired digit was the middle digit of a 3-digit sequence. The NC sequences had the property that, at the boundary, the preceding and following digits had different manners of production than the middle digit. Similarly, the CO sequences had the property that either the preceding or the following

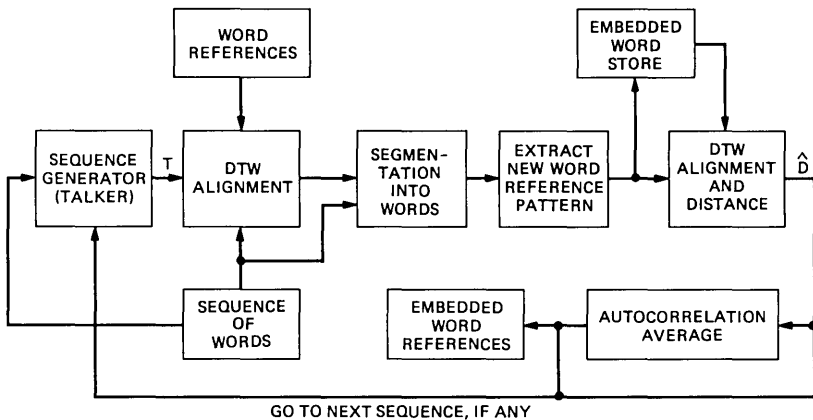


Fig. 3—Block diagram of embedded-digit training procedure.

Table I—Training sequences for embedded digits

NC Sequences			CO Sequences		
614	615	616	919	119	019
123	725	327	020	729	421
234	436	633	438	638	738
346	343	645	341	648	349
256	253	155	651	458	251
261	168	569	866	663	766
173	475	577	671	678	672
668	468	768	668	468	768
693	695	697	191	991	198
104	106	103	601	708	009
681	688	689	388	387	389
617	613	617	011	918	118
624	526	426	921	628	529
335	537	737	531	831	839
247	544	746	549	741	548
357	454	655	759	350	059
369	461	768	667	664	867
974	376	274	679	670	776
568	368	168	568	368	168
694	696	693	199	999	998
903	907	906	309	101	408
689	681	688	386	381	383

digit, or both, had a similar manner of production as the middle digit. Table I shows the actual training sequences for both the NC and CO cases. A total of 66 sequences* were defined for each case representing different environments for each of the digits in strings of a given type.

III. EVALUATION OF THE EMBEDDED-WORD TRAINING PROCEDURE

To study the effectiveness of the embedded-word training procedure, four talkers (two male, two female) each trained a connected-digit recognizer in the following manner:

(i) A set of isolated-digit templates was created for each talker using the robust training procedure of Rabiner and Wilpon.¹⁰ A single template was created for each of the ten digits. An eleventh template was created for the digit 8 in which the talker was requested to speak the digit 8 without releasing the final /t/. For the normal 8 template, each talker was told to release the final /t/. We designate the isolated-digit training set as IS.

(ii) Four sets of embedded templates were created for each talker, using the robust training procedure of Fig. 3. The four sets of templates differed in speed at which the talker spoke the three-digit training sequences (normal—NR, and deliberate—DL), and the degree of digit coarticulation (coarticulated—CO, and noncoarticulated—NC). Thus,

* For the digit 8, we considered both medial sequences (in which no release of the final t was made) and final sequences (in which the final t was asked to be released). For final sequences the digit 8 was extracted as the third digit in the string.

the four embedded training sets were denoted as CO.DL, CO.NR, NC.DL, and NC.NR.

The composite reference sets used for testing were created by considering various combinations of the isolated-digit set with one or more of the embedded-digit sets.

Two test sets (TS) of testing data were obtained. The first set, denoted as TS.DL, consisted of 40 randomly chosen (i.e., a different set of 40 strings for each talker) digit strings of varying length from two to five digits, each string spoken deliberately, that is, carefully articulated. The second set, denoted as TS.NR, consisted of the same 40-digit strings for each talker as in TS.DL but, instead, spoken at a normal rate.

Before presenting the results of the evaluation tests, one point is worth noting. Because of the difficulty in accurately finding digit boundaries of a digit embedded in a string of digits, the accuracy of the entire training procedure is suspect since the test recognition scores could be poor because of unreliable embedded-digit boundaries. To check this premise, the test strings used in the embedded-digit training procedure were processed manually, as well as by the automatic algorithm. The manual processing consisted of examining energy plots of the 3-digit string and listening to synthetic versions of the processed digits. This processing was performed iteratively on each string until the experimenter found the most acceptable boundaries for each digit. At this point, the automatic processing of the training procedure took over the rest of the template creation process.

A simple check on the accuracy of the automatic-word extraction process was made by comparing the word boundary frames of the automatic procedure with those of the manual procedure. Histograms were made for each talker for both the initial and final frames of the embedded digit. Typically, the frame error was less than one frame in about two-thirds of the cases, with somewhat larger errors for the remaining one-third of the cases. Figure 4 shows examples of such histograms for one talker. Shown in this figure are the histograms for the initial and final frame errors for two of the embedded-training sets.

A further check on the accuracy of the fully automatic technique was obtained by processing, for recognition, both the automatically obtained embedded-digit reference sets, and the manually obtained embedded-digit reference sets. We now discuss the recognition test results.

3.1 Connected-digits test evaluation of the training sets

For each of the two test sets (TS.DL and TS.NR) and for each talker, the following reference sets were used and tested:

1. IS—Isolated digits only, one template per digit, eleven digits.
2. CO.DL—Embedded digits only, obtained from coarticulated strings, deliberately spoken.

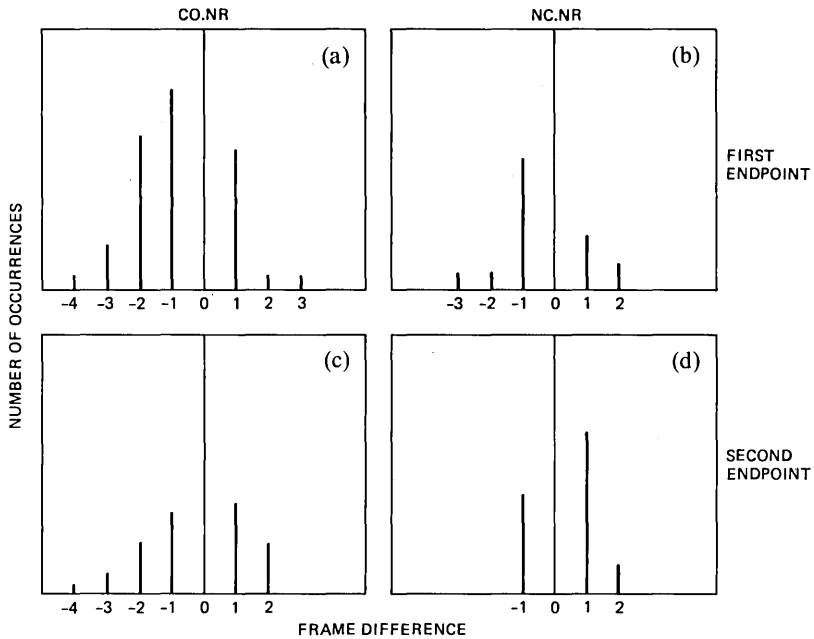


Fig. 4—Histograms of word boundary error (for one of the talkers) between manually and automatically determined boundaries for both (a) and (b) initial and (c) and (d) final boundaries for (a) and (c) CO.NR and (b) and (d) NC.NR.

3. NC.DL—Embedded digits only, obtained from noncoarticulated strings, deliberately spoken.

4. IS \oplus CO.DL—IS combined with CO.DL.

5. IS \oplus NC.DL—IS combined with NC.DL.

6. IS \oplus CO.NR—IS combined with CO.NR.

7. IS \oplus NC.NR—IS combined with NC.NR.

(Sets 4 to 7 had two templates per digit, eleven digits)

8. IS \oplus CO.NR \oplus CO.DL.

9. IS \oplus CO.NR \oplus NC.DL.

10. IS \oplus NC.NR \oplus CO.DL.

11. IS \oplus NC.NR \oplus NC.DL.

(Sets 8 to 11 contained three templates per digit, eleven digits).

For reference sets 2 to 11 both automatically and manually obtained templates were used.

Notice that not all single, and double combinations of the embedded sets were used. The sets that were omitted (e.g., CO.NR or NC.NR alone) were found to have high-error rates in preliminary tests; therefore, they were not fully evaluated.

The results of the recognition tests are given in Tables II and III. Table II gives results for TS.DL (the deliberately spoken strings) and

Table II—Recognition results (number of string errors) for different reference sets for TS.DL strings

	Talker Number	Single-Training Sets			Double-Training Sets				Triple-Training Sets			
		IS	CO.DL	NC.DL	IS ⊕				IS ⊕			
					CO.DL	NC.DL	CO.NR	NC.NR	CO.NR ⊕	NC.NR ⊕	CO.NR ⊕	NC.NR ⊕
Automatic endpoints— known-length strings	1	0	5	0	1	0	0	0	1	0	1	0
	2	4	2	2	0	2	2	0	0	1	0	1
	3	5	10	6	4	1	3	3	2	0	2	0
	4	2	0	2	2	2	2	2	2	2	2	2
	Total	11	17	10	7	5	7	5	5	3	5	3
Automatic endpoints—best string	1	0	15	1	2	2	0	1	2	1	3	3
	2	4	9	2	0	2	2	0	1	1	0	1
	3	6	20	10	7	5	9	13	7	6	7	6
	4	9	2	11	8	10	8	9	7	9	8	10
	Total	19	46	34	17	19	19	23	17	17	18	20
Manual endpoints—known- length strings	1	—	2	2	0	0	1	0	0	1	0	0
	2	—	4	1	0	0	0	0	0	0	0	0
	3	—	3	5	2	2	3	2	1	1	1	1
	4	—	0	3	2	2	2	2	2	2	2	2
	Total	—	9	11	4	4	6	4	3	4	3	3
Manual endpoints—best string	1	—	15	9	1	1	3	0	2	1	1	1
	2	—	10	3	3	3	0	0	2	2	2	2
	3	—	11	8	6	5	11	7	5	4	5	4
	4	—	0	11	7	9	8	10	6	8	7	10
	Total	—	36	31	17	18	22	17	15	15	15	17

Table III—Recognition results (number of string errors) for different reference sets for TS.NR strings

	Talker Number	Single-Training Sets			Double-Training Sets				Triple-Training Sets			
		IS	CO.DL	NC.DL	IS ⊕				IS ⊕			
					CO.DL	NC.DL	CO.NR	NC.NR	CO.NR ⊕	CO.NR ⊕	NC.NR ⊕	NC.NR ⊕
CO.DL	NC.DL	CO.DL	NC.DL	CO.DL	NC.DL	CO.DL	NC.DL					
Automatic endpoints— known-length strings	1	2	6	2	1	1	0	0	1	0	0	0
	2	10	5	5	1	3	6	2	1	3	1	1
	3	7	3	5	2	2	2	4	3	2	2	1
	4	4	3	5	4	1	3	1	4	1	1	1
	Total	23	17	17	8	7	11	7	9	6	4	3
Automatic endpoints—best string	1	2	13	5	2	1	1	0	2	0	0	0
	2	11	7	5	1	3	6	2	1	3	1	1
	3	11	6	12	4	6	8	9	7	8	5	6
	4	4	3	6	5	2	5	2	6	4	3	3
	Total	28	29	28	12	12	20	13	16	15	9	10
Manual endpoints—known- length strings	1	—	3	2	0	0	1	1	0	0	0	0
	2	—	3	3	1	3	2	2	1	3	1	2
	3	—	4	5	3	2	4	3	2	2	3	1
	4	—	8	6	3	1	2	1	3	1	1	1
	Total	—	18	16	7	6	9	7	6	6	5	4
Manual endpoints—best string	1	—	5	5	1	0	1	1	1	0	0	0
	2	—	7	3	1	3	3	2	1	3	1	2
	3	—	6	7	6	6	12	7	11	10	7	6
	4	—	9	7	3	2	4	2	3	3	1	2
	Total	—	27	22	11	11	20	12	16	16	9	10

Table III is for TS.NR (normally spoken strings). Results are given in this table as the number of string errors (out of a possible 40 strings) when evaluated using the LB DTW string recognizer. The results are given for the best string, regardless of actual string length, and for the best string with string length assumed to be known (KL) a priori. Scores are given for each talker, and a sum of total errors is given at the bottom of each table. A comparison is also provided, when possible, between manually (M) and automatically (A) embedded template sets.

The results of Tables II and III show conclusively that neither isolated- nor embedded-word templates, alone, are adequate for reliable recognition of connected-digit strings spoken at either deliberate or normal rates. It can be seen that the best overall scores were obtained by the triple combination sets with some small variations among them depending on the test set, and the talker. The double combinations provided scores almost as good as the triple combinations.

For the question as to whether to use coarticulated or noncoarticulated sequences in the training, the results of Tables II and III are essentially ambiguous. The scores on the double and triple combinations favor neither type of sequence over the other for both test sets. Similarly, the question as to whether to use deliberately or normally spoken strings in the training set is also left unresolved by the data in Tables II and III. In the next section, we investigate these issues further in a larger test of the overall procedure.

Perhaps the most significant conclusion from Tables II and III is that the error scores from the automatically extracted digit templates are essentially identical (to within small errors) to those of the manually extracted digit templates for all reference sets giving good recognition scores. This result indicated that the automatic training procedure was a useful one for obtaining embedded-digit templates for connected-digit recognition systems.

IV. LARGE-SCALE EVALUATION OF THE IMPROVED TRAINING PROCEDURE

The results of the preliminary test indicated that the improved training procedure led to a reliable set of embedded-digit templates, and that when combined with the normal set of isolated-digit templates, connected-digit, string-recognition scores greatly improved at normal speaking rates over those obtained using isolated-digit templates alone.

To provide a better understanding of the limitations of the improved training procedure, a larger evaluation test was performed in which 18 talkers (nine male, nine female) each used the improved training procedure to provide digit reference patterns. Only two sets of embed-

ded patterns were extracted, namely, NC.DL and CO.NR. The training sets studied in the evaluation included:

(i) All three single trainings sets, namely, IS, NC.DL, and CO.NR, each of which consisted of 11 patterns (including the unreleased eight).

(ii) The two combinations of isolated and embedded references, namely, $IS \oplus NC.DL$ and $IS \oplus CO.NR$. These sets consisted of 22 patterns.

(iii) The triple combination of $IS \oplus NC.DL \oplus CO.NR$. This set consisted of 33 patterns.

As in the previous test, each talker provided two test sets of 40 randomly selected connected-digit strings of from two to five digits. One set was spoken deliberately (TS.DL), the other set was spoken at a normal rate (TS.NR). The digit strings in both sets for the same talker were identical. Different talkers spoke different randomly chosen sets of digit strings.

The recognition test consisted of using the LB-based DTW algorithm to match the spoken test strings by the best sequence of reference patterns, regardless of length. In performing the matches, the parameters of the LB algorithm were set as follows:

(i) For all references and test sets, the parameters δ_{END} , M_T , and ϵ were given values of $\delta_{END} = 4$, $M_T = 1.6$, and $\epsilon = 20$.*

(ii) The parameters δ_{R_1} and δ_{R_2} were made to vary with each subset of reference patterns in the following manner. For isolated-digit patterns in all reference sets, the values $\delta_{R_1} = 4$ and $\delta_{R_2} = 6$ were used. For NC.DL reference patterns, the values $\delta_{R_1} = 2$ and $\delta_{R_2} = 3$ were used. For CO.NR reference patterns, the values $\delta_{R_1} = \delta_{R_2} = 0$ were used.

The logic for this choice was that the NC.DL patterns could be shortened somewhat, but not as much as the isolated patterns. However, the CO.NR patterns could not be shortened at all since they came from highly reduced, normally spoken digit sequences.

Before presenting results of the recognition tests, we first give some statistics on each talker's rate of talking.

4.1 Talking rate statistics

The statistics on average talking rate for each of the 18 talkers for both TS.DL and TS.NR strings are given in Table IV, and a summary of the overall average rate (as a function of number of digits in the string) is given in Fig. 5. The talking rates are given in terms of wpm. It can be seen that, for deliberately spoken strings, the average talker's rate varies from 99 to 156 wpm (across the 18 talkers). Thus, a high degree of rate variability exists across talkers for deliberately spoken strings of digits. For naturally spoken digit strings, the average talking rates

* These parameter values were chosen based on preliminary runs on connected-digit strings, as reported in Ref. 6.

Table IV—Average talking rates (wpm) for strings of varying length for TS.DL and TS.NR data

Talker	TS.DL				TS.NR			
	Number of Digits in String				Number of Digits in String			
	2	3	4	5	2	3	4	5
1	118	140	138	143	149	182	176	180
2	125	128	123	128	160	175	160	165
3	124	137	141	142	139	176	179	163
4	108	125	132	127	127	147	154	153
5	124	115	117	121	129	134	141	144
6	106	117	116	117	126	144	140	144
7	121	118	117	111	136	150	159	139
8	125	132	137	139	139	151	155	171
9	130	138	156	148	140	156	169	169
10	105	111	121	122	118	138	135	140
11	147	149	149	142	181	181	182	179
12	107	112	114	123	121	137	147	154
13	110	117	123	120	135	147	153	150
14	121	123	128	129	160	178	181	189
15	123	123	114	119	154	193	171	174
16	99	106	103	110	159	181	183	195
17	151	139	144	137	162	156	162	154
18	107	114	118	128	120	131	158	157
Average	126	131	134	135	150	166	170	171

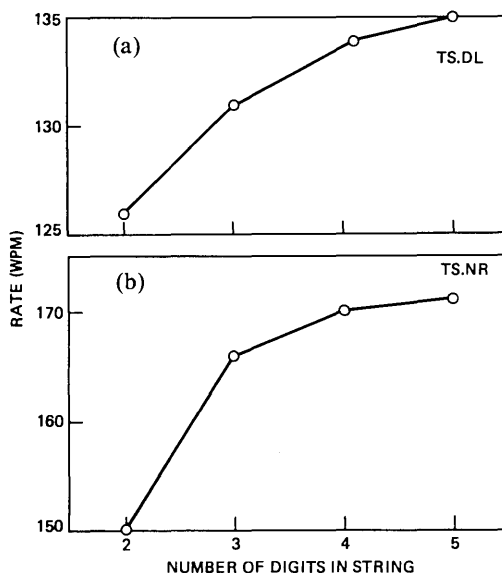


Fig. 5—Plot of average talking rate as a function of the number of digits in the string for (a) TS.DL and (b) TS.NR data.

vary from 118 to 193 wpm (across the 18 talkers), again pointing out the high degree of variability in normal talking rates.

However, the plots in Fig. 5 show that when averaged across talkers, the talking rate for different length strings does not vary as markedly

as for different talkers. For deliberately spoken digit strings, the slowest average rate is 126 wpm for two-digit strings, and the average rate increases to 134 wpm for four-digit strings. Almost no increase in average talking rate is found for five-digit strings over that for four-digit strings. For normally spoken digit strings, the same trends of the average talking rate are seen across different length strings. Thus, the average rate for two-digit strings is 150 wpm and it increases to 170 wpm for four-digit strings. However, the average rate for five-digit normally spoken strings (171 wpm) is essentially the same as for four-digit normally spoken strings.

4.2 Recognition test results on large data base

The results of the recognition tests on the 18-talker data base are given in Tables V and VI, and are plotted in Fig. 6. Tables V and VI give average- and median-string error rates (averaged over talkers and

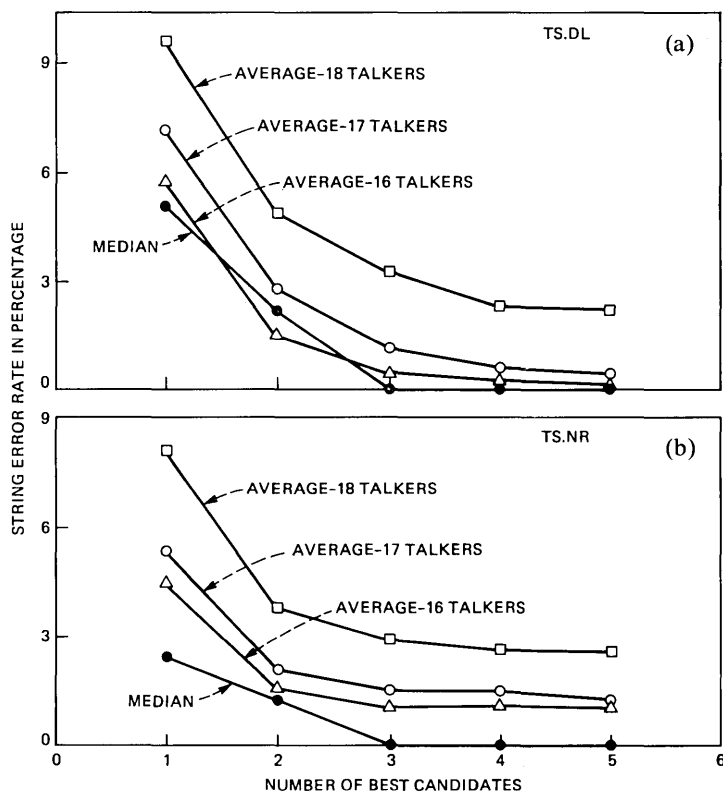


Fig. 6—Plots of string error rates versus number of best candidates for (a) TS.DL and (b) TS.NR data using reference set IS \oplus NC.DL \oplus CO.NR.

Table V—Average- and median-string error rates (percentage errors) for TS.DL data for the three reference sets

Reference Set	Statistic	TS.DL					
		Number of Best Candidates					
		KL	1	2	3	4	5
IS	Median	10.0	16.3	8.8	6.3	5.0	5.0
	18 Talkers	11.4	20.0	11.8	9.9	8.5	8.3
	17 Talkers	9.1	17.6	9.3	7.8	6.6	6.5
	16 Talkers	7.5	16.3	8.3	6.4	5.5	5.3
IS ⊕ NC.DL	Median	2.5	10.0	2.5	2.5	2.5	2.5
	18 Talkers	5.7	14.1	7.4	5.3	5.0	4.9
	17 Talkers	3.1	12.2	4.9	3.1	2.9	2.8
	16 Talkers	2.0	10.5	3.4	2.0	1.9	1.9
IS ⊕ NC.DL ⊕ CO.NR	Median	0	5.0	2.5	0	0	0
	18 Talkers	3.3	9.7	4.9	3.3	2.6	2.5
	17 Talkers	1.3	7.2	2.8	1.2	0.6	0.4
	16 Talkers	1.1	5.8	1.9	0.5	0.3	0.2

Table VI—Average- and median-string error rates (percentage errors) for TS.NR data for the three reference sets

Reference Set	Statistic	TS.NR					
		Number of Best Candidates					
		KL	1	2	3	4	5
IS	Median	11.3	13.8	10.0	7.5	7.5	7.5
	18 Talkers	16.3	19.0	11.7	10.3	10.1	9.7
	17 Talkers	13.1	15.9	9.3	8.1	7.9	7.5
	16 Talkers	13.0	15.5	9.1	8.0	7.8	7.3
IS ⊕ NC.DL	Median	5.0	7.5	3.8	3.8	3.8	3.8
	18 Talkers	8.3	11.5	6.4	5.8	5.4	5.3
	17 Talkers	5.3	8.4	4.0	3.7	3.2	3.1
	16 Talkers	4.8	7.8	3.3	3.1	2.7	2.7
IS ⊕ NC.DL ⊕ CO.NR	Median	2.5	2.5	1.3	0	0	0
	18 Talkers	5.8	8.1	3.8	2.9	2.6	2.5
	17 Talkers	3.7	5.4	2.1	1.5	1.5	1.3
	16 Talkers	3.4	4.5	1.6	1.1	1.1	1.1

various length strings) for three of the reference sets studied* (IS, IS ⊕ NC.DL, IS ⊕ NC.DL ⊕ CO.NR) for TS.DL data (Table V) and TS.NR data (Table VI). Included in the table are string error rates based on the top 1, 2, 3, 4, and 5 candidates (regardless of string length) and for the case in which the string length was known a priori (KL); that is, we only considered strings of the proper length. Results are given for the median error rate, the average error rate for all 18 talkers, the average error rate for 17 of the 18 talkers (omitting the one with the highest

* These three reference sets were chosen as they gave the best recognition rates and were representative of previously used training methods.

error rate), and the average error rate for 16 of the 18 talkers (omitting the two talkers with the highest error rates).

Figure 6 shows plots of the average and median error rates as a function of the top n candidates ($n = 1, 2, 3, 4, 5$) for both TS.DL and TS.NR data using the reference set $IS \oplus NC.DL \oplus CO.NR$, which provided the best overall results.

The results of Tables IV and V and Fig. 6 show the following:

(i) For deliberately spoken strings (TS.DL), the median-string error rate is 5 percent on the top candidate and falls to 2.5 percent on the top two candidates for reference set $IS \oplus NC.DL \oplus CO.NR$. Using reference set IS alone, the median error rate is 16.3 percent on the top candidate and is still 8.8 percent on the top two candidates. Using reference set $IS \oplus NC.DL$, the median error rate is 10.0 percent on the top candidate and 2.5 percent on the top two candidates.

(ii) For deliberately spoken strings, the median error rates with known-length strings are 0 percent for reference set $IS \oplus NC.DL \oplus CO.NR$, 10 percent for reference set IS , and 2.5 percent for reference set $IS \oplus NC.DL$.

(iii) For deliberately spoken strings, the average error rate scores for all 18 talkers are significantly larger than the median error rate scores. However, when the talker with the highest error rate is omitted, i.e., only 17 talkers are used), the average and median error rate scores are comparable.

(iv) For normally spoken strings (TS.NR), the median-string error rate is 2.5 percent on the top candidate and falls to 1.3 percent on the top two candidates using reference set $IS \oplus NC.DL \oplus CO.NR$. Using reference set IS alone, the median error rate is 13.8 percent on the top candidate and 10 percent on the top two candidates. Using reference set $IS \oplus NC.DL$, the median error rates are 7.5 percent on the top candidate and 3.8 percent on the top two candidates.

(v) For normally spoken strings, the median error rates with known-length strings are 2.5 percent, 11.3 percent, and 5.0 percent, for reference sets $IS \oplus NC.DL \oplus CO.NR$, IS , and $IS \oplus NC.DL$, respectively.

(vi) For normally spoken strings, the average error rate scores for all 18 talkers are significantly larger than the median error rate scores. Again, when the talker with the highest error rate is omitted (the same one as for deliberate strings), the average and median error rate scores become comparable.

From the above set of results, we can draw the following conclusions:

(i) The inclusion of embedded-digit training led to significant improvements in digit-recognition accuracy for both deliberately and normally spoken digit strings.

(ii) Somewhat better recognition accuracy was obtained when the string length of the test sequence was known than when no knowledge

of string length was used. This is due to the high probability of inserting extraneous short digits (the embedded twos and eights) in deliberately, and often naturally, spoken strings.

(iii) The accuracy with which connected-digit strings could be recognized can be made essentially independent of the talking rate, especially if one can take advantage of knowing in advance the length of the digit string.

(iv) Both coarticulated and noncoarticulated embedded-digit training patterns aid in recognizing connected strings of digits.

(v) There are some talkers (1 of the 18 tested here) for whom all the training procedures failed. For this one talker, the string error rate exceeded 50 percent on all reference and test sets. No obvious or clear explanation is available for this result, except for the fact that all the training procedures indicated a high degree of variability in speaking digits for this talker; that is, it took the maximum number of iterations to obtain each template set. This high degree of variability basically implied that no single set of reference patterns could adequately match the digits of this talker. Hence, highly inaccurate connected-digit recognition resulted.

The above results and the conclusions drawn from them indicated that the improved training procedure provided, in general, robust, reliable digit patterns that greatly aided the connected-digit recognizer in recognizing connected-digit strings for these talkers at essentially any reasonable talking rate.

4.3 Speaker-independent recognition using only isolated-digit training

Although the improved training procedure could be incorporated into a clustering analysis to provide speaker-independent, embedded-digit patterns, such an effort has not yet been undertaken. However, to provide a yardstick for comparison, a speaker-independent reference

Table VII—Median- and average-string error rates for speaker-independent recognition of connected digits

Statistic	Number of Best Candidates					
	KL	1	2	3	4	5
	TS.DL					
Median	5.0	12.5	5.0	2.5	2.5	0
18 Talkers	6.7	14.3	5.3	3.9	3.3	2.4
17 Talkers	6.0	12.9	4.3	3.2	2.7	1.8
16 Talkers	5.3	12.0	3.6	3.0	2.3	1.7
	TS.NR					
Median	12.5	20.0	10.0	5.0	2.5	2.5
18 Talkers	14.2	10.3	10.3	8.1	6.3	5.7
17 Talkers	12.7	16.8	8.7	6.6	5.0	4.4
16 Talkers	10.9	14.8	7.5	5.3	3.9	3.4

set consisting of 12 isolated-digit templates for each digit was used in the LB-based DTW recognizer using TS.DL and TS.NR data. The results of these recognition tests are given in Table VII. It can be seen that for TS.DL, the average- and median-string error rates for the 18-talker population are comparable to those of the speaker-trained sets of Table V. (This result is expected since the variability of the 12 patterns of each digit is adequate for representing inherent digit variations in deliberately spoken strings.) However, for TS.NR, the average- and median-string error rates using speaker-independent, isolated-digit references are much larger (on the order of 2:1) than those of Table VI for the speaker-trained case. These results again demonstrate the effectiveness of the embedded-digit training for recognizing digits in normally spoken strings.

V. DISCUSSION

The results given in Section IV show that for speaker-trained, connected-digit recognition, high reliability and accuracy can be obtained across a fairly broad range of talking rates by combining embedded-digit training patterns with the standard isolated-digit training patterns. The question that now remains is how useful is such a procedure for real-world applications, and what general types of problems remain. The answer to the first part of the question seems clear. For talkers who are fairly repeatable in the way in which they speak digits, both in isolation and in sequences, this improved training procedure should make connected-digit recognition a viable procedure. For the remaining talkers (e.g., the talker who had substantial digit variability), this procedure is too simplistic and cannot adequately represent the variations in pronunciation of digits. An analysis of the errors made in trying to recognize the strings of such talkers shows no consistent error pattern; that is, the method basically breaks down because of the high variability in the spoken-digit strings. In a sense, the entire training procedure has broken down for such talkers; therefore, the matching procedure is doomed to failure.

The answer to the second part of the main question as to what general types of problems remain is not at all clear. A detailed examination of the types of errors that occurred in all the test sets indicates a fairly broad mix of digit insertions, digit deletions, and digit substitutions. It would appear that for most of these errors there is no simple fix. In these cases, we are basically at or near the limits at which a matching procedure can operate. In such cases, a feature-based, connected-digit recognizer would appear to offer more promise in that it would be less sensitive to parametric variability so long as the detected features remain in the acoustic signal. Since all spoken strings were highly intelligible to the experimenters, it would seem that the promise

of perfect-digit recognition needs a less-sensitive parameterization, i.e., one more closely related to phonetic features, to be fulfilled.

VI. SUMMARY

An improved training procedure for extracting reference-word templates for connected-word recognition systems has been described. The resulting reference patterns essentially model the word characteristics when embedded in connected-word strings. Hence, a reference set consisting of both isolated-word patterns and embedded-word patterns has the capability of providing reliable recognition of connected-word strings spoken at natural rates. In an evaluation of this procedure and using a digit vocabulary, it was shown that high-string accuracy could be obtained, if the length of the digit string was known a priori, for deliberately and naturally spoken digit strings. If the length of the digit was not known, the string error rate was somewhat higher due to the problem of inserting short digits into the matching sequence.

REFERENCES

1. T. K. Vintsyuk, "Element-Wise Recognition of Continuous Speech Composed of Words from a Specified Dictionary," *Kibernetika*, 2 (April 1971), pp. 133-43.
2. J. S. Bridle and M. D. Brown, "Connected Word Recognition Using Whole Word Templates," *Proc. Inst. Acoustics, Autumn Conf.* (November 1979), pp. 25-8.
3. H. Sakoe, "Two Level DP-matching—A Dynamic Programming Based Pattern Matching Algorithm for Connected Word Recognition," *IEEE Trans. Acoustics, Speech, and Signal Processing, ASSP-27*, No. 6 (December 1979), pp. 588-95.
4. L. R. Rabiner and C. E. Schmidt, "Application of Dynamic Time Warping to Connected Digit Recognition," *IEEE Trans. Acoustics, Speech, and Signal Processing, ASSP-28*, No. 4 (August 1980), pp. 377-88.
5. C. S. Myers and L. R. Rabiner, "A Level Building Dynamic Time Warping Algorithm for Connected Word Recognition," *IEEE Trans. Acoustics, Speech, and Signal Processing, ASSP-29*, No. 2 (April 1981), pp. 284-97.
6. C. S. Myers and L. R. Rabiner, "Connected Digit Recognition Using a Level Building DTW Algorithm," *IEEE Trans. Acoustics, Speech, and Signal Processing, ASSP-29*, No. 3 (June 1981), pp. 351-63.
7. S. Tsuruta et al., "Connected Speech Recognition System DP-100," *NEC Res. and Dev.*, 56 (January 1980), pp. 88-93.
8. S. Tsuruta, "DP-100 Voice Recognition System Achieves High Efficiency," *J. Eng. Ed.*, (July 1978), pp. 50-4.
9. C. S. Myers and L. R. Rabiner, "A Comparative Study of Several Dynamic Time Warping Algorithms for Connected Word Recognition," *B.S.T.J.* 60, No. 7 (September 1981), pp. 1389-09.
10. L. R. Rabiner and J. G. Wilpon, "A Simplified, Robust Training Procedure for Speaker Trained, Isolated Word Recognition," *J. Acoust. Soc. Am.*, 68, No. 5 (November 1980), pp. 1271-6.

Simulation and Design Studies of Digital Subscriber Lines

By S. V. AHAMED

(Manuscript received July 14, 1981)

To investigate the feasibility of transmitting data bidirectionally between 56 and 144 kb/s, an extensive simulation and experimental study was undertaken. The computational techniques for the study have been developed and coupled to a large data base, which contains the individual loop configurations of a statistically significant population of the Bell System loop plant. Two modes of transmission (the hybrid and the time-compression multiplexing) are investigated thoroughly by computational techniques, and the simulated plots are compared with experimentally generated oscillograms. These results are displayed graphically by eye diagrams for individual loops and by scatter plots for all the loops in the data base. Different varieties of scatter plots display different attributes of eye diagram. Broad spectrums of such results are cross-compared to choose optimal systems and circuit configurations for a particular mode of transmission at a particular bit rate. Effects of varying terminating networks are also studied and the extent of echo cancellation necessary is investigated by studying the amplitude and the shape of near-end reflections. Various codes are investigated even though the primary emphasis has been on the bipolar code. Major conclusions are summarized in the concluding remarks.

I. INTRODUCTION

Digital data transmission over existing loop plant facilities has been envisioned by numerous organizations around the world. In Japan,^{1,2} initial designs for digital data transmission rates up to 64 kb/s are being investigated. In Switzerland, there has been initial interest³ to provide an overall transmission rate of up to 160 kb/s. In Sweden, an 80-kb/s burst system, operating at 256 kb/s in 125- μ s slots has been investigated.⁴ In Norway,⁵ digital pulse-code modulation (PCM) hybrid

transmission rates greater than 64 kb/s (up to 80 kb/s) have been analyzed. In Great Britain, hybrid 64-kb/s channels have been proposed^{6,7} by superimposing them over the baseband analog telephone communications. Other Western European countries^{8,9} (Germany, France, and Italy) have started discussion of high-speed digital transmission.

In the Bell System, the results of preliminary investigations have been reported.^{10,11,12} This paper presents the computer simulations and the entire cross section of results obtained from the extensive simulations that have been performed using a loop plant data base in conjunction with specific terminal systems. The simulations test the functioning of any given system with existing loops from the 1973 Loop Survey,¹³ they test the effects of component design variations, and variations of such factors as temperature, loop configuration, etc., and, finally, they verify the eye opening performance at different bit rates.

The paper also presents the results of such simulations under two major modes of transmission: (*i*) a full-duplex simultaneous bidirectional transmission of data with a hybrid and active echo canceler (hereafter referred to as the hybrid system), and (*ii*) the time-compression multiplex ["burst" or the "ping-pong" system (hereafter referred to as the TCM system)].

The remainder of the paper covers five major sections. Each section addresses a specific issue in the overall design. Section II gives the simulation techniques and data base organization. (The Appendixes contain the mathematical framework of the computation.) In Section III, the electrical characteristics of the loop plant, as they pertain to the transmission of data (2.4 to 324 kb/s), are tabulated. Some of the physical data are also given to indicate the wide variety of loops in the plant. Section IV described the time-domain simulations (with numerous codes) which yield wave shapes and eye diagrams at the receiver. Section V compares the performances of different systems at different rates between 56 to 324 kb/s. Results are summarized as scatter plots, each showing an attribute of the eye diagrams for all the loops in the data base. Section VI describes a computer-aided design technique for evolving an optimal equalization strategy. The effects of different equalizer designs on the eye openings at the receiver is also documented. Finally, the concluding remarks give the overall summary of findings.

II. TECHNIQUES: SIMULATION, DATA BASE, AND ORGANIZATION STRATEGY

2.1 Introduction

Any repetitive periodic phenomenon may be analyzed by Fourier analysis. To study the transmission system response, we resort to a

long periodic sequence (48 pulses) of randomly distributed data. The flexibility of analyzing the system performance in the spectral domain becomes available before inverting the Fourier series to obtain the time-domain response. The process is carried out independently for the two directions of data transmission over one pair of wires. Simultaneous bidirectional transmission performance evaluation in the hybrid system entails calculation of reflections arising because of cable and termination mismatch at all the harmonics of the overall repetitive period. The transmission rate is the line rate. The TCM transmission, however, is unaffected by near-end reflections since data transmission is multiplexed in the time domain by increasing the transmission rate to 2.25 times the information rate.

To evaluate the system performance on individual loops, it is necessary to access data bases which store statistical samples of loop compositions of the existing loop plant. Thus, the simulation capability performs four functions: computations, data base manipulations, generation of graphical displays, and provision of a capability for evaluation and optimization of the system components. The first three of these functions need minimal operator intervention, and the last function is interactive with the system designer.

2.2 The Basic concepts in time-domain simulations

Transmission of digital data is a time-domain phenomenon. However, electronic circuitry and cable characteristics are better defined in the spectral domain. Hence, to simulate the entire physical process of the data transmission, we resort to a limit-cycle¹⁴ approach. The entire system—the electronic circuitry and the individual loop under study is forced into a periodic function in which the boundary conditions at the beginning and the end of a predefined period are identical. The approach facilitates the transformation of the cyclic time-domain phenomenon into its harmonic spectral-domain components by Fourier series. Enough flexibility is provided to alter the mode of excitation to correspond to any random or specified pulse pattern within a sufficiently long period.

2.3 Spectral-domain considerations

Spectral-domain responses are essential subsets that can be isolated from time-domain simulations. To provide systematic computations, the spectral-domain and time-domain simulations access identical data bases and subprograms. The data base generation and display programs are separate. They have been completely automated to generate and graphically display predefined component and system characteristics.

2.4 Representational techniques

2.4.1 Excitation signals

A 48-pulse period* spans the repetitive cyclic time. Any random or prespecified pattern of pulses are transmitted in either direction. Delta function or finite-width pulses have been simulated with different coding (alternate bipolar, ternary, polar, etc.) options.

Sixty-four Fourier harmonics represent the pulses. This choice reflects the presence of filters with a sharp roll-off beyond the system cutoff frequency. The truncation at 1-1/3 bit rate (i.e., 64/48) has little effect on the accuracy of the simulation, but cuts the core requirement and execution time.

2.4.2 Component representation

Bidirectional data transmission systems generally have a transmitter, a loop, a filter, an equalizer, a terminating impedance, and a device to limit the near-end reflections.[†] For the delta functions or finite pulse-width multilevel pulses at the transmitter, the excitation functions are defined in Appendix A. The loop (Section 2.4.3) is characterized by ABCD matrices (one set for each harmonic frequency). The filter is represented by standard transfer functions. The equalizer is programmed by the distribution of poles and zeros. The matching impedance being passive has a simpler characterization. Finally, the isolating device which separates the received and transmitted signal is represented in the frequency domain (for frequency-domain cancellation circuits) or in the time domain (for CCD-type transversal filter circuits). The technique of the computation of the cancellation signal varies appropriately. In the TCM mode of transmission, the contaminating signal is ignored because the transmitter is inactive during the reception of the signal and vice versa.

2.4.3 Loop representation

The loop constitutes the most variable component in the entire system. A summary of Bell System loop statistics has been reassembled in a dedicated data base. Composite loops (with numerous loop sections and bridged taps) are represented by their individual ABCD matrices at each harmonic frequency. The temperature of cable (aerial vs. buried) sections can vary drastically. Hence, temperature distributions are also permitted in the simulation by an identifier scheme to indicate particular lengths which experience the differential temperatures.

* The 48-pulse period is an arbitrary duration. The limited core capacity of the dedicated computer was the primary reason for the choice. More recently, we have been able to extend the simulations to 480 pulses and 1200 harmonics.

[†] Typical examples are echo cancelers, hybrids, frequency-domain cancellation circuits, or time-division switches.

The R, L, G, and C parameters, at different temperatures for different lengths, are calculated by accessing a separate data base, storing the primary parameters¹⁵ and their temperature variations.

2.5 Computational techniques

2.5.1 System components

Conventional circuit analysis of components is performed by accepting critical resistors, capacitors, and transistor data. Noncritical components are represented by transfer functions. When the sensitivity analysis is performed, individual components are perturbed. When the sensitivity of system blocks is analyzed, the transfer functions are perturbed. Cascading appropriate ABCD matrices for the loop sections leads to composite loop ABCD parameters (see Appendix B). These parameters are generated from the central office to the subscriber, and the A and D terms are interchanged for the other direction, thus reducing the core requirements and execution time. The terminating impedance effects are computed by multiplying the ABCD matrix of the cable (with adequate attention to the direction of transmission) by the ABCD matrix of the terminating impedance.

2.5.2 Restoration to time domain

The excitation function has obvious poles at $p = 2\pi im/T$ ($m = 1, 2, \dots, M$) and the computational technique for evaluating the normal Fourier integral becomes converted to the summation of (M) harmonics responses over K pulse periods (see Appendix C). The two highlights before the double summation in eq. (10) (see Appendix C) are (i) the entire transfer function of the total system including filters, equalizers, and any echo cancelers [i.e., $\zeta(p)$, see eq. (6), Appendix C] can be obtained after finding the composite ABCD parameters for both directions of transmission, and (ii) the use of L'Hôpital's rule in evaluating the residues at the M poles [see eq. (9), Appendix C].

2.5.3 Simulation of echo cancellation

During simultaneous bidirectional transmission of data, the near-end echo adds to the received signal within the hybrid. There are two ways of simulating the echo-canceler function. The first one consists of computing the total signal (reflections and the received pulses), and then subtracting the reflection out systematically. The second method consists of systematically dropping all, or a large fraction, of the frequency-domain reflected signal before summing the Fourier components.

2.5.4 Echo cancellation signal from single-pulse response

The reflections of a single-pulse excitation from the Central Office

(co) side and then from the subscriber (s) side are stored. There are 240 time positions covering the 48-pulse period. These responses are then shifted by the same amount that any new pulse is shifted from the original pulse that gave the first reflection. The response of the pulses occupying the 48 time slots of random excitation is obtained as a summation of all the responses suitably displaced from the location of the original pulse. Since the excitation is assumed to be periodic, any overflow beyond the 240 time positions is reaccumulated at the beginning of the period.

The subtraction of the reflected signal from the total signal by the echo canceler is carried out by either of two ways: (i) prespecified fraction (between 90 to 99 percent) of the total reflected signal is systematically subtracted from the total signal at the received end, and (ii) a randomly varying fraction averaging to a prespecified number (90 to 99 percent) of the total reflected signal is subtracted from the total received signal. The reason for the use of a second procedure was to reflect the uncertainties caused by the convergence in the tap weight setting of a real echo-canceler device. These settings can change slightly because of the number of iterations the device has experienced at any instant of time. Being an adaptive device, the setting varies by small increments around the average value with time, and the second computational procedure reflects this uncertainty. For the illustrations presented here, the first procedure of echo cancellation is used since the second one causes a small random perturbation of the data* obtained in the first.

2.5.4.1 Simplified echo cancellation. The simulation of the echo canceler is done by suppressing the addition of the reflected signal in the frequency domain before summing the Fourier components. The inaccuracy of this technique is because the time events are only approximated by the Fourier expansion in view of the truncation of the harmonics. These inaccuracies are not consistent in the representation of the limit cycle encompassing a finite number of pulses (48 in this case) with the inaccuracies in the representation of a single pulse whose reflection was determined in the former case. In the latter case, only a percentage (90 to 99 percent, depending on the quality of the echo canceler) of each of the harmonics of the entire 48-pulse period is subtracted. In the former case, the specified percentage of the total reflected signal in the time domain was subtracted out. However, the simplicity of the simulation procedure has prompted the use of the latter method in most cases after determining that the difference of the echo suppressions by the two methods does not cause more than

* Very marginal eyes are occasionally closed, and an occasional error of the marginal bit occurs.

a 2- to 3-percent change in the eye openings in either the CO side or the S side.

2.6 Establishment of permanent bases

The primary data bases consist of three permanent files: (i) the cable characterization, (ii) the Loop Survey files holding the loop composition of all the 1973 survey loops up to the 18-kft loop without bridged taps, and (iii) the files containing the same loops including details of bridged-tap locations and composition.

2.6.1 Access and reuse of selected bases

Very long computations yield large files, and unless some systematic steps are taken to conserve the disc space, results obtained from different systems of different components cannot be easily cross-compared. Hence, certain disc files or a group of files are reused continuously. A typical group of such files holds excitation pulse patterns and their harmonics, filter transfer functions, equalizer transfer function (if it is amenable to such a representation), single-pulse response function (if it is to be used in conjunction with an echo canceler), etc. It is also necessary for the intermediate computations to be completed before the reuse of the allocated disc space. A typical example of such a situation is after the generation of the time-domain received pulse data from the spectral domain. The eye statistics (eye openings, top, central, bottom-eye thicknesses, and the eye height) have to be computed from a separate program before the files holding the time-domain response can be reused. Hence, the use or reuse of intermediate data bases needs special consideration in the overall architecture of the system.

2.7 Conclusions

In Section II, the major highlights of the software simulation system are presented. Numerical algorithms, computations, and functions are organized independently of the major housekeeping and file management functions. The entire system has been tailored to work efficiently and smoothly on dedicated minicomputers. System capabilities range from simply analyzing the data for statistical characteristics from the data bases to the entire system simulation under data transmission and the analysis of failure rates, details of eye closure, and sensitivity analysis of components.

III. FUNDAMENTAL LOOP PLANT STATISTICS FOR DIGITAL DATA TRANSMISSION

3.1 Introduction

Possible data transmission rates envisioned for the future range

from 56 to 324 kb/s. A set of seven bit rates (2.4, 4.8, 9.6, 64, 144, 216, and 324 kb/s) is chosen to span the range of interest. The 1973 Loop Survey presents a cross section of loops that may be expected to carry the data traffic. However, they may be generally limited to a loop length of 18 kft because of the presence of loading coils beyond this distance. This section presents characterization of the loops in two loop configurations: (i) with all bridged taps stripped, and (ii) with all bridged taps intact. Image impedances (at the half-bit-rate frequencies 1.2, 2.4, 4.8, 32, 72, 108, and 162 kHz) are also presented. The physical statistical data are presented in condensed form and selected electrical parameters are also tabulated.

3.2 Organization of results (loops with bridged taps stripped)

3.2.1 Physical characteristics

Eliminating loops longer than 18 kft, those with loading coils, and nonstandard cable sections, about 76 percent (831* loops) of the 1098*-loop population surveyed¹³ constitutes the truncated data base over which the digital data transmission studies are based. A histogram relating the population to distribution of the loops by their length and the number of cable section(s) is shown in Fig. 1a. The typical overall composition of an average loop (in the truncated population), which is 7748.63 ft long, has 4500.59 ft of No. 26 AWG cable with 2408.47 ft of No. 24 AWG cable, 797.52 ft of No. 22 AWG cable and, finally, with 42.03 ft of No. 19 AWG cable. Figure 1b shows the average composition of the loops in each kft band between 0 to 18 kft.

3.3 Typical results generated at 32 kHz for 64-kb/s rate (loops with bridged taps stripped)

There are three sets of results for the three temperatures (140°F, 60°F, and 0°F) at which the simulation is done over all the loops in the data base. This section gives the typical results at 60°F. In Figs. 2 and 3, the loop attenuations are shown as scatter plots of the individual attenuation of each loop. Figure 3 gives the data when the attenuation is plotted against the converted loop length. The conversion of the actual loop length to its equivalent No. 22 AWG cable length is done by first determining the equivalency numbers between cable length for a given attenuation and then by cumulating the length of each loop section in terms of its equivalent length.

In Figs. 4 and 5 the resistive component of the impedance is plotted against the reactive component for each of the loops at 32 kHz and 60°F. Denser clusters of points are detected around the impedance

* For clarification, "loop survey" refers to the 831-loop data base, and "Loop Survey" refers to the original 1098-loop data base.

(147-j94) ohms of No. 26 AWG cable. This result reinforces the dominance of No. 26 AWG cable also represented in Fig. 1a.

3.4 Summary of results (loops with bridged taps stripped)

At each frequency and at each temperature, the high, low, and average values of the most important parameters are tabulated (see Table I). In addition, two specific parameters evolve from this computation: (i) the gauge conversion factor for equalization, and (ii) the temperature length equivalency number. The first parameter becomes critically important while determining the equalization required to compensate for mixed gauge loops at any particular frequency. For the digital transmission, we have found that if the conversion numbers estimated at half-baud-rate frequency are used consistently at all harmonic frequencies of the pulse pattern, the eye diagrams predicted after the analysis very closely match those obtained by an experimental procedure. Hence, for data transmission at 216 kb/s, 1 kft of Nos. 19, 24, and 26 AWG cables yield the same loss as 0.648, 1.408, and 1.923 kft of the No. 22 AWG cable. These results are obtained by plotting the loss of the various gauges at 108 kHz, and then proportioning the lengths.

The second conversion number is also obtained by a similar procedure. The equivalent change in the length, caused by every degree change in temperature, is evaluated by plotting the losses at numerous temperatures, and then a coefficient of temperature sensitivity is obtained by proportioning the length accordingly.

This coefficient α , which relates the length (l_2 in feet) at temperature $t_2^\circ\text{F}$ and the length (l_1 in feet) at temperature $t_1^\circ\text{F}$, is defined as

$$l = l_1[l + \alpha(t_2 - t_1)] \text{ ft.}$$

Coefficient α has been evaluated as 2.135×10^{-3} per degree F, at 108 kHz. This number becomes important in determining the equivalent length of loops in terms of No. 22 AWG cable at 55°F .

3.5 Organization of results (loops with bridged taps intact)

3.5.1 Physical characteristics

The truncated data base consisting of 831 loops has a total of 1365 bridged taps. The average loop is 7748.63 ft long, has approximately four sections, and has 1.64 bridged taps on it. The length of an average tap is 922.42 ft, consisting of about 54 percent of No. 26 AWG, 33 percent of No. 24 AWG, 12 percent of No. 22 AWG, and less than 1 percent of No. 19 AWG cable composition. The median distance between the CO and the first tap is 6523 ft, and the median distance between the first and second taps is 1071 ft. Loops between 0 to 1 kft have the longest average length of bridged tap—1333.3 ft, with 1.15

Table I—Maximum, minimum, and average values of loop impedances at different frequencies (no bridged taps)

kb/kHz	Degrees	Central Office Side of Loops (Zin)						Subscriber Side of Loops (Zin)					
		Maximum		Minimum*		Average		Maximum		Minimum*		Average	
		Re	Im	Re	Im	Re	Im	Re	Im	Re	Im	Re	Im
2.4/1.2	140	744	-696	400	-400	649.3	-628.8	720	-544	416	-380	632.0	-634.1
	60	680	-644	376	-376	607.6	-586.9	664	-660	388	-352	593.9	-592.3
	0	632	-616	368	-332	572.7	-552.0	640	-616	352	-344	561.7	-557.0
4.8/2.4	140	544	-500	272	-270	466.4	-443.1	512	-500	264	-265	446.6	-443.8
	60	504	-456	256	-256	437.1	-412.5	480	-456	264	-240	420.4	-414.4
	0	480	-432	240	-240	412.5	-387.0	456	-344	256	-228	398.2	-389.6
9.6/4.8	140	400	-365	190	-180	336.6	-311.2	380	-350	180	-190	318.5	-307.1
	60	370	-325	190	-160	316.7	-288.7	360	-325	165	-160	300.4	-286.1
	0	360	-300	180	-155	299.9	-269.8	340	-290	162	-155	285.2	-268.4
64/32	140	170	-110	97	-22	144.6	-93.1	170	-110	85	-16	138.3	-86.8
	60	170	-101	92	-16	140.4	-83.9	165	-100	85	-14	134.4	-78.2
	0	168	-94	92	-14	136.9	-76.3	160	-96	85	-12	131.3	-70.9
144/72	140	145	-67	90	-17	120.4	-51.3	150	-70	90	-8	117.4	-47.2
	60	145	-60	90	-15	119.4	-45.3	147	-61	86	-7	116.6	-41.7
	0	145	-55	90	-11	118.7	-40.5	145	-37	83	-6	116.1	-37.1
216/108	140	134	-54	85	-6	114.1	-37.4	140	-50	89	-6	112.0	-34.7
	60	134	-50	86	-5	114.0	-32.9	140	-46	90	-4	112.1	-30.5
	0	134	-45	86	-4	114.1	-29.3	136	-43	94	-1	112.2	-27.1
324/162	140	130	-40	86	-6	110.1	-27.4	134	-42	87	-5	108.1	-25.7
	60	132	-34	88	-3	110.6	-24.1	132	-40	86	-3	108.8	-22.7
	0	134	-36	90	-1	111.1	-21.5	134	-39	88	-1	109.3	-20.3

* The low numbers in these columns are not very accurate, since they are not program generated; instead, they are all scaled from the scatter plots.

bridged taps for each loop. The average composition of each bridged tap is 59.3, 37.0, 3.7, and 0.0 percent of Nos. 26, 24, 22, and 19 AWG cables. The total number of loops in this kft band is 20, and 17 of these do have bridged taps. The average loop length is 776 ft.

Loops between 17 to 18 kft have the highest average number (2.87) of bridged taps per loop. The average loop length is 17,331.19 ft, and the average bridged tap is only 626.9 ft. The average composition of the bridged tap is 10, 74.0, 16.0, and 0.0 percent of Nos. 26, 24, 22, and

Table II—Bridged-tap distribution by loop lengths (0 to 18 kft)

Loop Length in Feet	No. of Bridged Taps	No. of Loops, No Bridged Taps	No. of Loops
0-1000	23	3	20
1000-2000	48	6	38
2000-3000	82	4	56
3000-4000	104	13	69
4000-5000	104	12	64
5000-6000	115	16	77
6000-7000	114	5	64
7000-8000	115	7	72
8000-9000	121	5	67
9000-10,000	97	3	53
10,000-11,000	96	8	55
11,000-12,000	87	8	52
12,000-13,000	59	3	38
13,000-14,000	50	5	31
14,000-15,000	45	1	26
15,000-16,000	32	3	21
16,000-17,000	27	0	12
17,000-18,000	46	2	16
Total no. of loops = 831	Loops: No bridged taps = 104	Loops with bridged taps = 727	

Table III—Average loop length and average bridged-tap length distribution

Loop Length in Feet	Average Loop Length	Average No. of Bridged Taps	Average Bridged-Tap Length
0-1000	776.00	1.15	1333.35
1000-2000	1559.74	1.26	995.58
2000-3000	2548.87	1.46	782.12
3000-4000	3544.38	1.51	1121.13
4000-5000	4539.55	1.62	939.42
5000-6000	5445.13	1.49	962.14
6000-7000	6481.23	1.78	740.68
7000-8000	7483.33	1.60	957.54
8000-9000	8541.78	1.81	904.93
9000-10,000	9446.68	1.83	848.39
10,000-11,000	10572.91	1.75	843.49
11,000-12,000	11466.83	1.67	1092.56
12,000-13,000	12435.87	1.55	938.66
13,000-14,000	13383.77	1.61	932.66
14,000-15,000	14412.73	1.73	917.27
15,000-16,000	15447.76	1.52	926.06
16,000-17,000	16490.17	2.25	1016.19
17,000-18,000	17331.19	2.87	626.91
Total no. of bridged taps = 1365	Average length of bridged taps = 922.42		

Table IV—Maximum, minimum, and average values of loop impedances at different frequencies (with bridged taps)

kb/kHz	Temperature °F	Central Office Side of Loops (Zin)						Subscriber Side of Loops (Zin)					
		Maximum		Minimum		Average		Maximum		Minimum		Average	
		Re	Im	Re	Im	Re	Im	Re	Im	Re	Im	Re	Im
2.4/1.2	140	704.8	-639.7	176.8	-513.2	560.0	-499.2	649.9	-640.	178.3	-120.6	497.47	-533.24
	60	652.3	-597.5	160.4	-478.3	520.8	-467.7	609.6	-597.5	161.5	-114.7	471.19	-497.8
	0	606.8	-562.1	147.8	-449.7	488.8	-440.9	575.8	-562.1	148.6	-109.5	448.5	-468.0
4.8/2.4	140	520.4	-453.0	123.4	-364.3	411.8	-343.1	476.3	-449.9	131.8	-78.8	340.5	-340.47
	60	486.0	-418.9	120.3	-337.3	383.6	-321.7	440.7	-419.5	123.9	-73.5	323.9	-346.9
	0	456.8	-393.5	117.3	-315.3	360.2	-303.4	412.1	-394.4	117.3	-69.5	309.6	-326.6
9.6/4.8	140	393.1	-324.8	91.5	-259.8	303.3	-230.7	351.6	-314.1	80.4	-57.2	234.5	-252.5
	60	371.5	-302.1	83.3	-239.0	284.2	-215.8	331.0	-292.6	78.6	-49.2	223.9	-236.5
	0	349.4	-281.4	77.6	-221.83	268.4	-203.2	313.2	-274.3	78.3	-44.5	214.9	-222.8
28/56	140	204.4	-129.7	48.8	-97.2	150.3	-100.7	198.8	-128.9	31.2	-9.5	106.6	-82.4
	60	198.7	-119.5	44.7	-87.3	145.2	-82.4	188.9	-117.6	30.5	-7.0	103.8	-76.0
	0	193.9	-112.4	41.8	-79.1	141.1	-67.1	178.0	-109.2	30.2	-5.4	101.6	-70.6
32/64	140	196.0	-120.1	47.1	-88.9	144.3	-99.1	193.2	-121.0	28.9	-4.3	102.3	-74.7
	60	194.7	-112.2	43.8	-79.6	139.9	-82.0	188.3	-112.2	29.1	-0.9	99.8	-68.7
	0	192.9	-105.5	40.3	-71.9	136.4	-67.0	181.3	-103.2	28.6	+2.6	98.0	-63.7
40/80	140	187.8	-108.9	44.7	-76.1	135.7	-95.2	177.9	-105.0	25.5	+3.1	96.1	-63.2
	60	189.8	-99.4	43.9	-67.7	132.3	-82.2	181.3	-100.5	24.9	+8.9	94.2	-57.8
	0	189.6	-94.8	41.8	-60.8	129.7	-70.2	183.1	-96.6	24.8	+15.3	92.9	-53.4
72/144	140	187.1	-101.7	40.3	-49.3	120.5	-67.5	157.6	-84.3	21.5	+27.8	85.2	-39.7
	60	190.5	-98.4	40.1	-43.2	119.4	-62.4	164.1	-84.5	21.3	+43.7	84.6	-35.9
	0	192.0	-93.0	40.1	-38.3	118.7	-57.6	175.3	-85.7	21.2	+54.6	84.2	-32.8
96/192	140	206.7	-79.7	38.6	-39.5	115.8	-49.6	180.3	-84.1	19.4	+49.7	82.6	-31.5
	60	233	-80.2	38.6	-34.5	115.4	-49.6	186.8	-83.5	20.3	+54.4	82.5	-28.1
	0	253.3	-81.1	38.7	-30.5	115.2	-50.6	200.7	-85.1	18.9	+56.8	82.4	-25.4
108/216	140	212.2	-105.5	37.9	-36.1	114.4	-38.0	180.1	-82.7	16.3	+59.4	81.8	-29.0
	60	198.8	-111.5	38.0	-31.5	114.2	-36.8	194.0	-81.4	16.5	+68.5	82.0	-25.9
	0	201.8	-114.2	38.1	-27.8	114.2	-37.5	203.1	-84.4	16.8	+74.9	82.1	-23.3
162/324	140	216	-119.7	35.1	-26.7	110.2	-34.6	184.8	-100.6	15.2	+74.5	78.5	-22.4
	60	233.4	-133.4	35.4	-23.4	110.7	-27.9	213.6	-105.3	14.0	+81.4	79.2	-20.3
	0	261.5	-145.5	35.6	-20.8	111.2	-19.8	242.0	-108.1	13.3	+88.0	79.8	-18.6

Table V—Maximum and average attenuation of loops

kb/kHz	Temperature (°F)	Attenuation in dB	
		Maximum	Average
2.4/1.2	140	11.7	4.93
	60	10.7	4.49
	0	9.9	4.13
4.8/2.4	140	15.6	6.92
	60	14.1	6.29
	0	13.3	5.78
9.6/4.8	140	21.5	9.63
	60	19.5	8.73
	0	18.0	8.01
28/56	140	45.5	19.93
	60	41.0	17.75
	0	37.4	16.02
32/64	140	47.6	20.82
	60	42.9	18.50
	0	39.1	16.66
40/80	140	50.6	22.27
	60	45.6	19.72
	0	41.7	17.72
72/144	140	60.0	26.30
	60	53.3	23.22
	0	47.9	20.84
96/192	140	66.2	28.46
	60	60.5	25.21
	0	56.4	22.73
108/216	140	69.1	29.44
	60	61.9	26.13
	0	56.4	23.62
162/324	140	76.0	33.15
	60	69.0	29.68
	0	63.5	27.08

19 AWG cables, respectively. Between these extremes (shortest loops with longest bridged taps and longest loops with shortest bridged taps) lies a population whose average bridged tap length is fairly consistent. Even though the population density is sparse, the in-extreme bands of length (0 to 1 kft and 17 to 18 kft), the population density in the intermediate bands (Table II) is relatively high and the statistical information derived is dependable. These statistics are tabulated in Tables II and III. The percentage of loops having bridged taps (≥ 0 , ≥ 1 , ≥ 2 , etc.) is shown in Fig. 6. Figure 7 (compare against Fig. 1a) displays the gauge distribution in the bridged tap. These distributions indicate similar patterns with a dominance of No. 26 AWG cable, which is gradually replaced by No. 24 AWG cable as the length of the loop

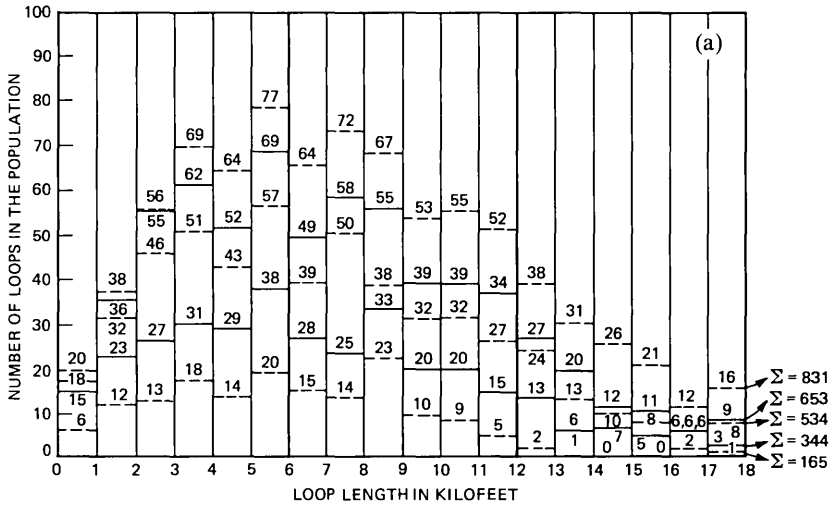


Fig. 1a—Histogram of loop population distribution by number of cable sections in each kft.

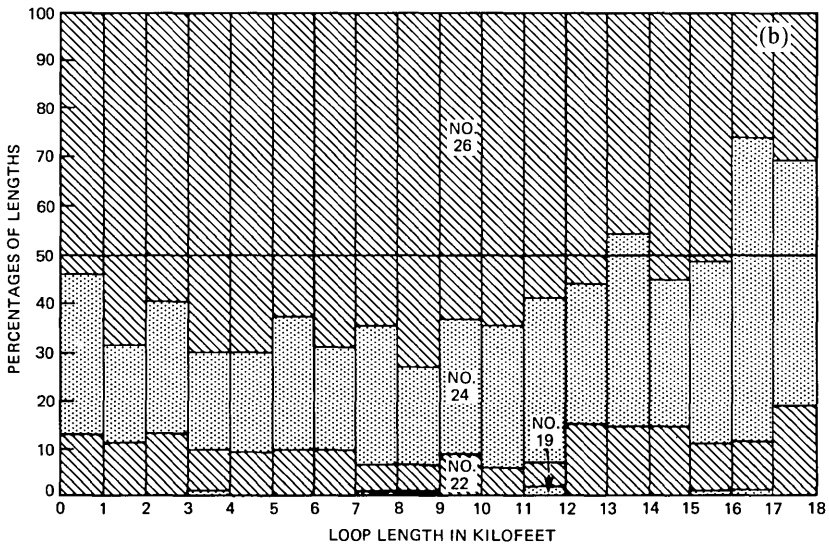


Fig. 1b—Distribution of gauge numbers with loop length.

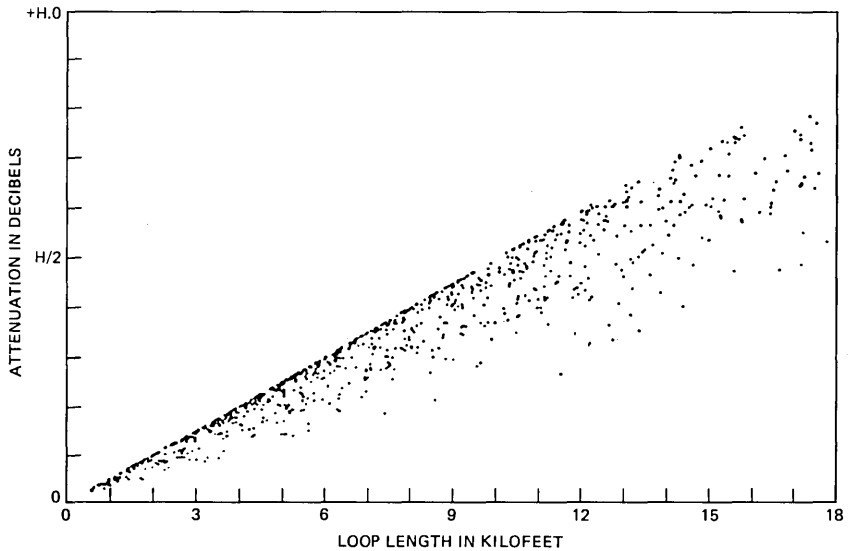


Fig. 2—Scatter plot of loop attenuations plotted against the loop length at 32 kHz and 60°F. The X-scale is 1 kft per division and Y-scale is 5.0 dB/division.

increases. Numbers 22 and 19 AWG cables do not dominate either the bridge tap or the loop lengths.

3.6 Summary of results (loops with bridged taps intact)

The loops in the survey have been simulated at three temperatures (140°F, 60°F, and 0°F). However, the discrete frequencies have been expanded to include (28, 40, and 96 kHz for 56, 80, and 192 kb/s rates). A summary of the image impedance at the ten discrete frequencies (1.2, 2.4, 4.8, 28, 32, 40, 72, 96, 108, and 162 kHz) is tabulated in Table IV. Table V gives a summary of loop attenuations.

3.7 Conclusions

The loop plant environment is far from the ideal situation where uniform gauge wires run from the co to the s. Any design of the bidirectional data transmission facility has to accommodate the wide disparity of cable compositions, bridged-tap configurations, and highly variable impedances looking from either direction of the loop. The range and statistics of these variations have been presented in this section as tables and scatter plots for use in the design of terminal equipment of digital subscriber lines.

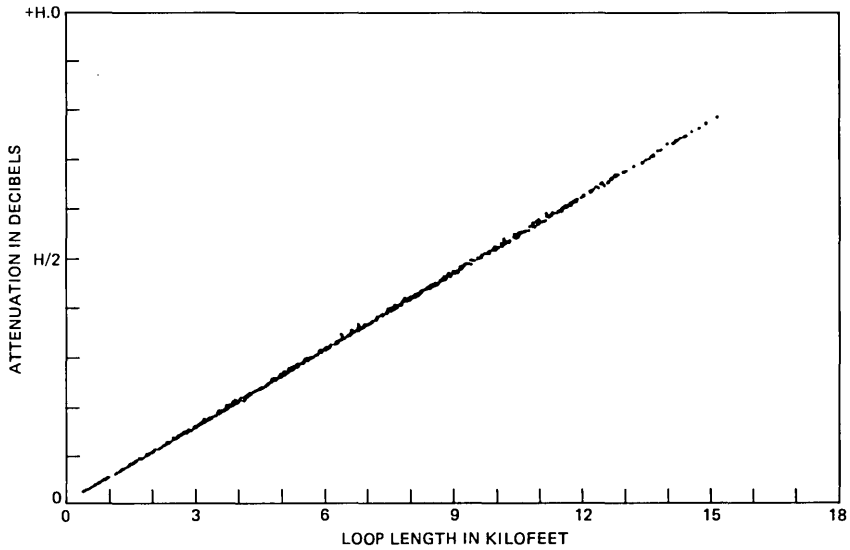


Fig. 3—Scatter plot of loop attenuations plotted against the equivalent loop length of No. 22 AWG cable. The frequency is 32 kHz and the temperature is 60°F. The X-scale is 2 kft/division and Y-scale is 5.0 dB/division.

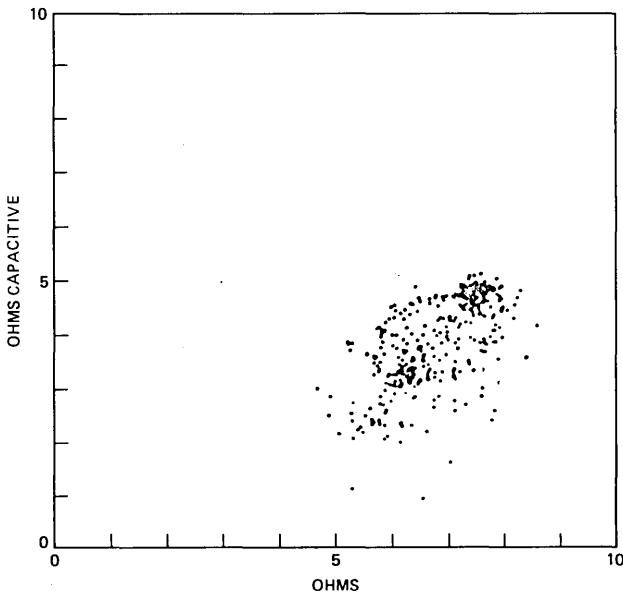


Fig. 4—Scatter plot of loop resistance plotted against its impedance (Central Office side). Temperature = 60°F, Frequency = 32 kHz, X- and Y-scales = 20 ohms/division.

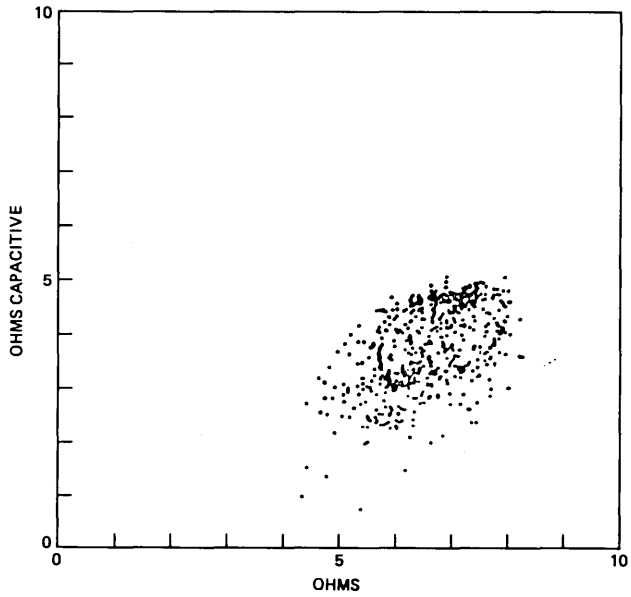


Fig. 5—Scatter plot of loop resistance plotted against its impedance (subscriber side). Temperature = 60°F, Frequency = 32 kHz, X- and Y-scale = 20 ohms/division.

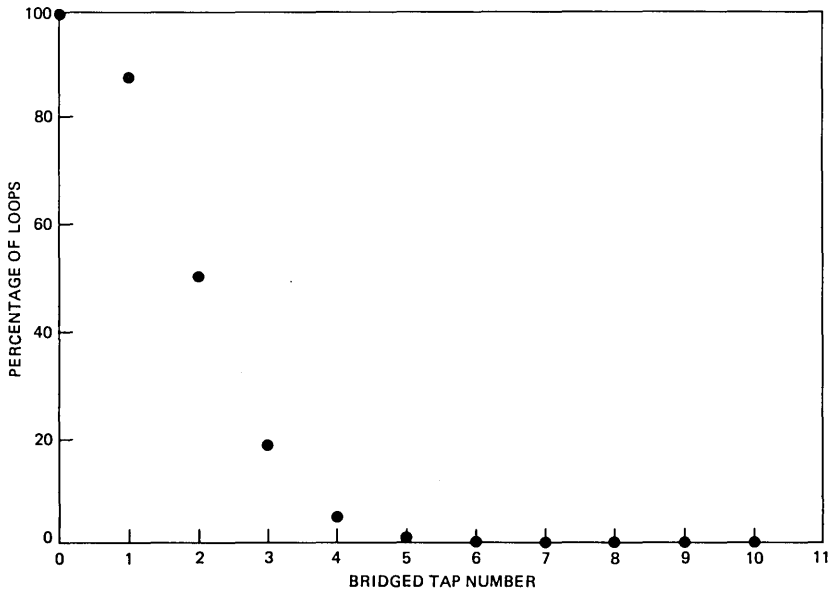


Fig. 6—Percentage of loops (Y-axis) having bridged taps equal to or greater than the bridged-tap number (X-axis) plotted.

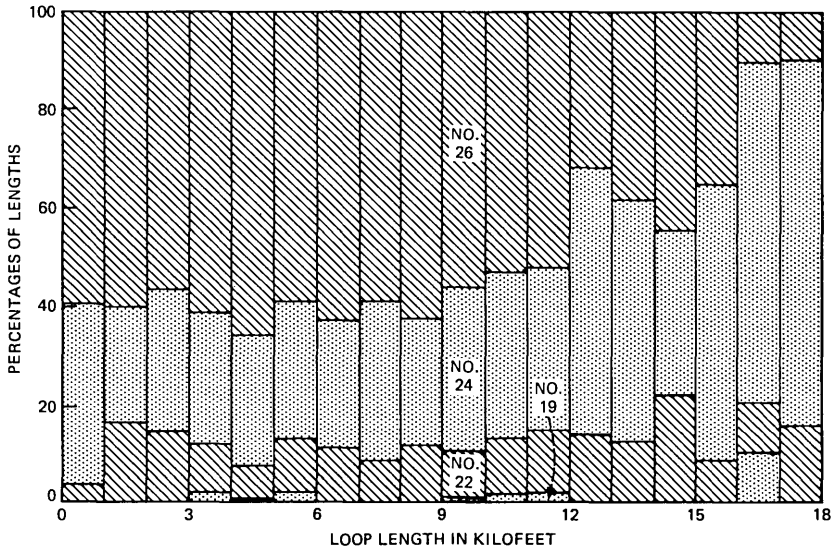


Fig. 7—Distribution of percentages of gauge sizes in the bridged taps.

IV. TIME-DOMAIN SIMULATIONS

4.1 Introduction

In this section, we present the time-domain results of typical hybrid data transmission systems, typical time-compression multiplexing systems with bipolar, ternary, partial response, and WAL-2 modes of coding. Single-pulse responses, pulse shapes, and eye diagrams are presented over a wide range of loop and terminating configurations.

The time-domain response of a transmission system is critically important in evaluating its capabilities to carry digital data. Such a response can be obtained from the spectral-domain response of the system by using conventional or fast Fourier transforms. However, FFTs were not used due to limited core capacity of the dedicated minicomputer on which the simulations were performed. The basis for obtaining the time-domain response of the entire system has been summarized in Section II.

4.2 Performance of the computational model

The flexibility of the software system to permit the simulation of any linear system configuration has been indicated (see Section II). Here, a hybrid duplex system with two electronic terminations having two four-section, sixth-order loss equalizers, (with equalization tailored for each loop) has been simulated.

When the cable length is made vanishingly small, typical component

(especially filter) performances and the validity of the model may be verified. Further, the delay through the filters may also be accurately determined. To establish these facts, two results are presented.

In Fig. 8a, a sequence of random pulses is used to excite the system from the co to the s side. Forty-eight pulse positions are plotted here. The first 16-pulse positions are shown in the top one-third of the figure (see the second horizontal line from the top). The second and third 16-pulse positions are plotted on the fourth and sixth lines of the figure. Also, the second (+1)-pulse position ($20.83 \mu\text{s}$)* after the start of the 48-pulse duration is the response of the first (+1) pulse at the transmitter end.

In Fig. 8b, the eye diagram corresponding to the pulse train in Fig. 8a is shown. There are seven lines constituting the eye diagram. The two outermost lines are formed by 0, 1, 0 and 0, -1, 0 transitions. The two intermediate inner lines are formed by -1, 1, -1 and 1, -1, 1 transitions, and finally the three innermost lines are formed by 1, 0, -1; -1, 0, 1; and 0, 0, 0 transitions of the pulses. A pulse diagram similar to that shown in Fig. 8b for the s-to-co direction of transmission is also obtained.

4.3 Single-pulse response over loops

Single-pulse response is essential to judge the capabilities of the overall system. Three crucial results emerge from the single-pulse response study: the deterioration of the received pulse, the extent of the long decaying tails left behind by the pulse, and the magnitude and the shape of reflections of the sent pulse at the sending end. Component values affecting these responses can then be suitably adjusted if the results prove unsatisfactory.

Single-pulse responses from single and multiple sections have been routinely computed, examined, and verified. Typical results from a three-section composite cable loop are presented in Figs. 9a through 9d. The loop consists of 3133 ft of No. 26 AWG cable, together with 8367 ft of No. 22 AWG cable, in series with 1365 ft of No. 19 AWG cable. The long tail of the pulse (Fig. 9a) received at the s side indicates that the following pulses would be offset from their zero position because of the influence of prior pulses. Next, consider the shape of the reflected pulse (Fig. 9b) on the s side. There are three peaks embedded in this pulse shape, and the central peak being almost as high as the received pulse would be a source of severe interference. Unless the reflections are substantially cancelled out by an echo canceler (see Section 4.4), the eye diagram would be considerably distorted.

* The bit rate for this particular simulation is 144 kb/s, and the delay can be computed by measuring the distance of the peak of this pulse (+1) from the instant $t = 0$ at the left-hand corner of the figure for the first 16 pulses.

Next, examine Figs. 9c and 9d. Here, the problem is exaggerated because of the relative magnitude of the received and reflected pulses, the ratio of these being 1:2.84. If it is desired to keep the pulse distortion down to 5 percent of the received-pulse height, the minimum amount of cancellation for the reflected signal should be 35 dB. Advancing one stage further, the single-pulse response can also predict that the nature of interference from a bipolar-pulse sequence 1, -1, 1, -1 is going to be different from the nature of interference caused by a pulse sequence 1, 0, 0, -1. In the former case, the positive half of the reflected pulse tends to become additive to the leading negative reflection of the next pulse, thus increasing the demands on the cancellation to about 41 dB. In the latter case, the reflections do not become additive because of the intermediate zeros in the pulse sequence. Similar considerations exist for the many different coding algorithms that can be used for transmission.

4.4 Random-data response

Random-data responses have been routinely generated to test the capability of the system over numerous loops. For the sake of consistency, results from the simulation of the loop in Section 4.3 are presented under this type of excitation. A random-pulse sequence of 48 bits is generated by selecting random bits of random numbers generated by the computer.

Further, we have been able to document excellent correspondence between computed eye diagrams and those from experimental results over a large number of loop configurations and bit rates. An example of this correspondence is evident between Figs. 10a and 10b. The experimentally generated eye (Fig. 10a) is obtained by transmitting 144-kb/s data over 18 kft of No. 22 AWG cable with 35 dB of echo cancellation (see Section 2.5). The eye opening is 74.7 percent. The computationally generated eye (Fig. 10b) is also obtained for the same conditions, and the eye opening is 74.8 percent. The eye opening is defined as the average of the top and bottom eye openings as a percentage to the average of the top and bottom eye heights.

4.4.1 Bipolar coding (hybrid transmission)

In the hybrid mode of transmission, the quality of the eye diagram depends on the extent of echo cancellation. To illustrate this point, Fig. 11a shows the eye diagram at the CO side of the loop, with no echo cancellation at 144-kb/s on a typical loop (3133 ft, No. 26 AWG; 8367 ft, No. 22 AWG; and 1365 ft, No. 19 AWG cables). Figure 11b shows the eye with perfect echo cancellation. Finally, Fig. 11c, shows an eye diagram with 30-dB echo cancellation.

4.4.2 Bipolar coding (time-compression multiplexing)

The transmission rate is increased to 324-kb/s for an effective bidirectional rate of 144 kb/s. The eye diagrams in this mode of operation are obtained by suppressing all reflections in the frequency domain, since only a unidirectional flow of data is present at any one instant. Figure 12 shows the eye diagram at the CO side of the loop.

4.4.3 Ternary coding

Simulations of ternary coding were limited because of the increasing degradation of the eye diagram. Most of the eyes were closed with composite cable loops and, hence, the results from a loop with 18 kft of No. 22 AWG cable, with 100 percent echo suppressions are given in Figs. 13a and 13b. Because of the symmetry of the loop, the corresponding figures for the other side of transmission are substantially the same as those in Figs. 13a and 13b; however, minor differences because of changes in clusters of bit patterns in the two 48-bit sequences (one from the CO side to S side and the other from the S side to CO side) are present. The ripple between bits $-1, -1, -1, \dots$ and $1, 1, 1, \dots$ was primarily responsible for the thickening of the eye in Fig. 13b. Further, long tails are also observed at the end of a sequence of data.

4.4.4 Class four partial response coding

Class four partial response coding¹⁶ yields wave shape and eye diagram (Figs. 14a and 14b) considerably different from those with bipolar coding. Two distinct degradations occur. In the Y direction, the eye opening relative to the peak tends to suffer more because of the relative displacement of the peak of the eye relative to the peak eye opening. In the X direction, the horizontal eye opening tends to become limited because of the limited response of the system—the major advantage being that the system bandwidth is about one-half the bandwidth for bipolar coding. The particular loop over which the data transmission was simulated does not have any bridge taps but is composed of three cable sections as discussed in Section 4.3.

4.4.5 The WAL-2 codes

The WAL-2 codes also limit the bandwidth necessary for transmission.¹⁷ The received data wave shape and eye diagram (Figs. 15a and 15b) also differ from those with the earlier types of codes. Here, the limited system response generates slowly varying pulse shapes (Fig. 15a). Generally, these codes are robust-to-line discontinuities but suffer in the presence of bridged taps. For the simulations given here, the loop was approximately 11 kft long, with nine cable sections and three bridged taps.

4.5 Time-compression multiplexing results with modified terminal configurations

The equalizer used for simulations in Section 4.4 has the capability to be tailored to the line loss by cascading up to three sections of sixth-order equalizers. Each of these sections provides for the loss of about 6000 ft of No. 22 AWG cable at 144 kHz. However, this particular approach has been abandoned in favor of an extended range equalizer (see Section 6.5). The circuitry for this equalizer has been adjusted such that there is a clear match between the attenuation of cables at different frequencies and the corresponding equalizer gain. Next, to simplify the termination impedance, the matching circuitry is substituted by a single resistance, which approximates the statistical average of the loop impedances at half the baud rate (see Table I, Section III). Further, it has been computationally determined (and experimentally verified) that the harmonics of the transmitted signal can be adequately controlled by adjusting the pulse width and, thus, saving the cost of an additional filter. Hence, the time-compression multiplexing simulations differ from the hybrid system to the extent that

- (i) the bit rate is 2.25 times the bidirectional hybrid transmission bit rate,
- (ii) the echo cancellation function is absent in the TCM mode,
- (iii) the initial filtering of transmitted pulse is eliminated,
- (iv) the pulse width has been computationally optimized at about 40 percent of the pulse period, and
- (v) the matching circuit for all the cables has been approximated as the statistical average of all the resistive components of the image impedance of the cables at a frequency equal to half the baud rate.

The advantages of the hybrid system inherent in maximizing the bandwidth utilization and the impulse noise immunity have to be weighed against the complexity of the echo canceler necessary to eliminate the reflections and also against the enhanced NEXT interference (over that in the TCM system) into other cable pairs. Conversely, the simplicity of the design and construction of the time-compression multiplex system has to be weighed against the higher loop losses and increased impulse noise susceptibility caused by increased bandwidth.

In Figs. 16a and 16b, the experimentally and computationally generated eye diagrams are compared for 14 kft of No. 24 AWG loop at 324 kb/s. The eye opening predicted by the simulation is 85 percent, and the experimentally determined eye opening is 83 percent at an instant t_1 , and is 76 and 75 percent, respectively at instant t_2 . Similar results are obtained for typically mixed cable composition in Figs. 17a and 17b for a loop consisting of four sections. The No. 19 AWG cables at the

end of the loop make the configuration close to the worst type of cable composition. The experimentally determined eye opening is approximately 54 percent and the computationally predicted eye opening is 57 percent.

4.6 Effects of bridged taps

Bridged taps play a critical role in judging the capability of existing loops to carry digital data. At a particular bit rate, the number, lengths, and location of taps influence the pulse shapes and, consequently, the eye diagrams. For the simulation presented in this section, a No. 22 AWG, single-cable 10.5-kft loop with perfect echo cancellation is used. The results of the simulation are presented in Figs. 18a through 18d for zero-, one-, two-, and three-bridged taps, respectively. In Fig. 18a, there are no bridged taps on a 10.5-kft, No. 22 AWG loop. The bit rate is 144 kb/s, with perfect echo cancellation for all the simulations. In Fig. 18b, one bridged tap (No. 22 AWG, 1.5 kft long) is added 2 kft away from the CO end of the loop. In Fig. 18c, a second bridged tap (No. 22 AWG, 1.5 kft long) is added 1.5 kft away from the first bridged tap. In Fig. 18d, a third bridged tap (No. 22 AWG, 1.5 kft long) is added 1.5 kft away from the second bridged tap. The CO-to-S side eye diagrams for the four cases* are shown.

The results for other gauge cables are similar, but the results for composite cables with bridged taps are dramatically inferior to those presented here because of mismatch (and hence, additional eye closure) between the loops and terminating impedances.

4.7 Effects of pulse widths

Harmonic content of the transmitted signal may be controlled by filtering delta function excitation pulses or by altering the pulse width of the transmitted signals. The TCM system is a special beneficiary of the latter method (thus reducing the cost of an additional filter) because of the absence of received data during transmission. This makes the system more robust against NEXT interference (if the transmission and reception of data is synchronized).

The effect of changing the pulse width was studied with a particular TCM system. The simulation was carried out on a 17,314-ft eight-section loop from the 1973 loop survey data base. The composition of the loop is 7789 ft of No. 26 AWG; 2998 ft of No. 24 AWG; 2564 ft of No. 26 AWG; 25 ft of No. 24 AWG; 957 ft of No. 26 AWG; 2120 ft of No. 24 AWG; 141 ft of No. 26 AWG; and 720 ft of No. 24 AWG cables. From our experience, this particular loop had the worst eye opening carrying

* Overall optimization in the system design yields significantly better eye openings (see Sections VI and VII) in spite of bridged taps. In this Section, eye degradations caused by bridged taps in one of the early systems is shown.

324-kb/s data at 60°F in the TCM system. The results of changing the pulse width are shown in Fig. 19, showing a broad insensitivity to pulse width in the 20- to 40-percent duty cycle range for the particular equalizer simulated. This test has prompted the use of 40-percent duty cycle in the subsequent TCM simulations.

4.8 Conclusion

Simulations of the two general configurations for the bidirectional digital line have been accomplished. The system of time-domain programs is capable of simulating most of the physical conditions that exist on loops. Effects of temperature, code variations, component tolerances, and loop configurations on the eye diagrams have been routinely analyzed. Proposed systems are entirely simulated, and the effectiveness of each component on the eye opening is individually or combinatorially determined. The presence of bridged taps and their

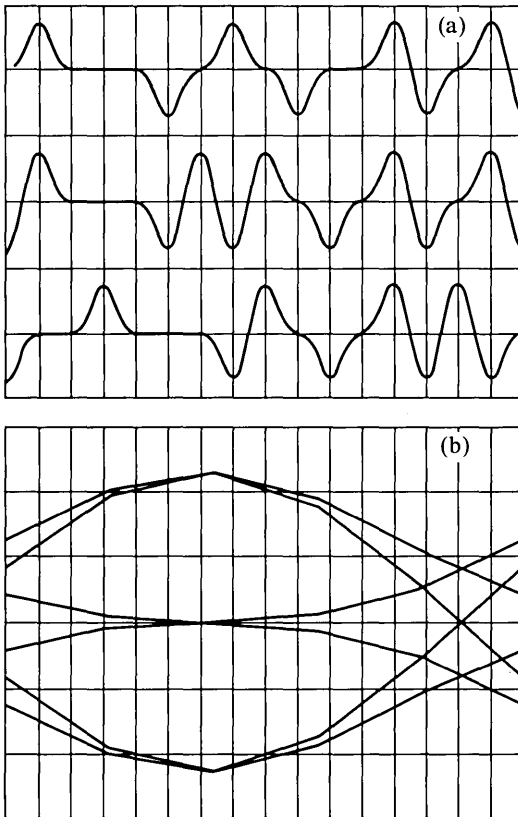


Fig. 8—System characteristics with zero loop length. (a) Pulse pattern and shape at the receiver. (b) Eye diagram at the receiver.

critical location in the loops is analyzed by a series of simulations. Crosstalk and impulse noise effects are not included in the simulation reported here.

The execution time of the programs has been about 20 minutes on a Data General Nova 2 minicomputer and about 50 seconds on a Data General Eclipse S-250 computer. It also translates to about 10 seconds on the IBM 370.

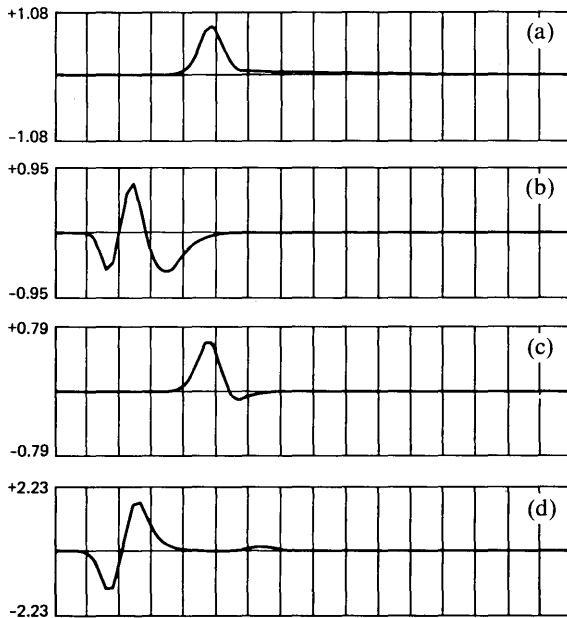


Fig. 9—Transmission and reflection of a single pulse on a typical loop consisting of three cable sections. Pulse rate is 144 kb/s, and each box width corresponds to 1-pulse duration. (a) Received pulse at s end of loop. (b) Reflected pulse at s end of loop. (c) Received pulse at co end of loop. (d) Reflected pulse at co end of loop.

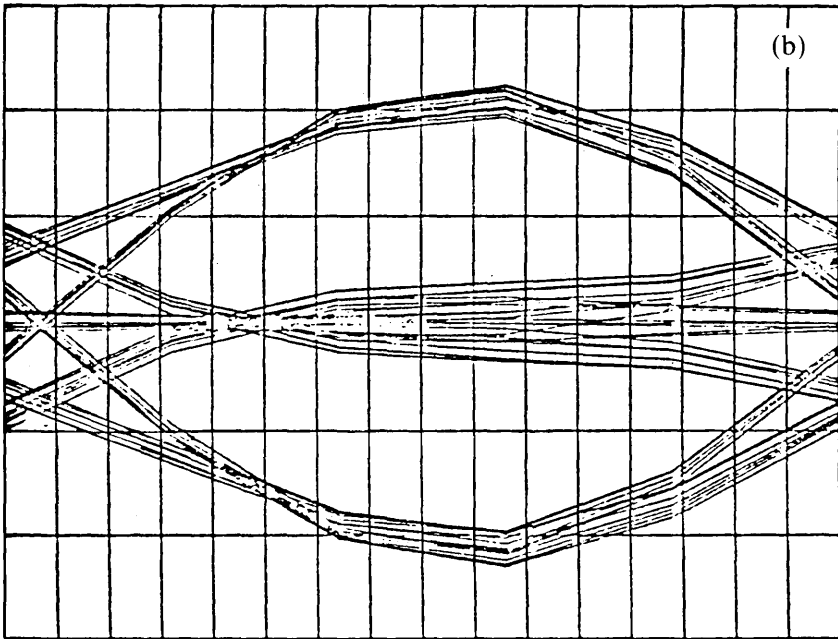
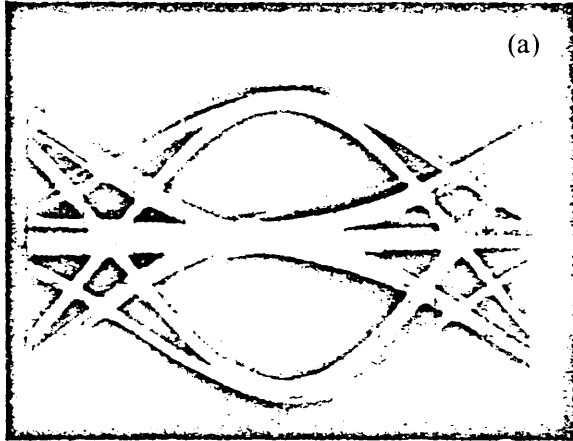


Fig. 10—Experimentally (a) and computationally (b) generated eye diagrams by transmitting bidirectional data over 18 kft of No. 22 AWG cable. The echo cancellation is 35 dB.

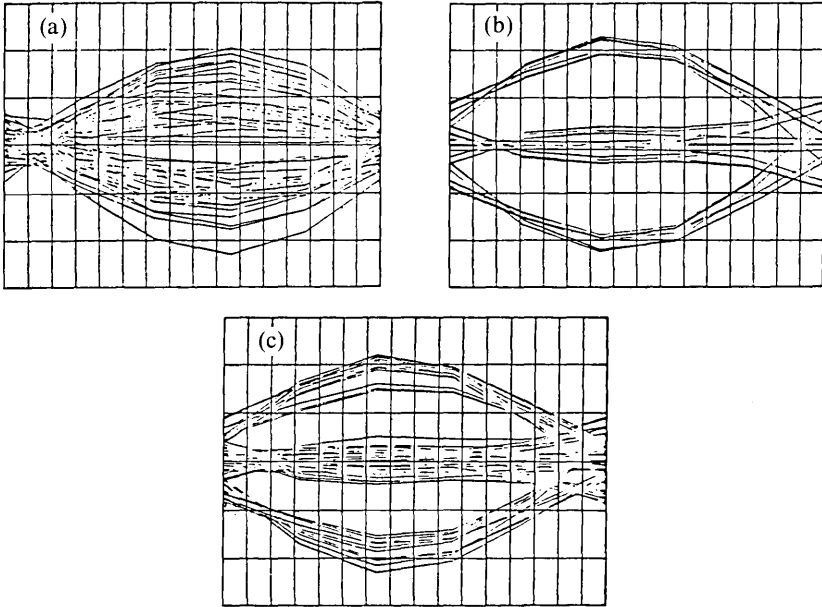


Fig. 11—Eye diagrams obtained by transmission of 144 kb/s bidirectional data over a typical loop. In (a) there is no echo cancellation, in (b) there is perfect echo-cancellation, and in (c) there is 30-dB echo cancellation.

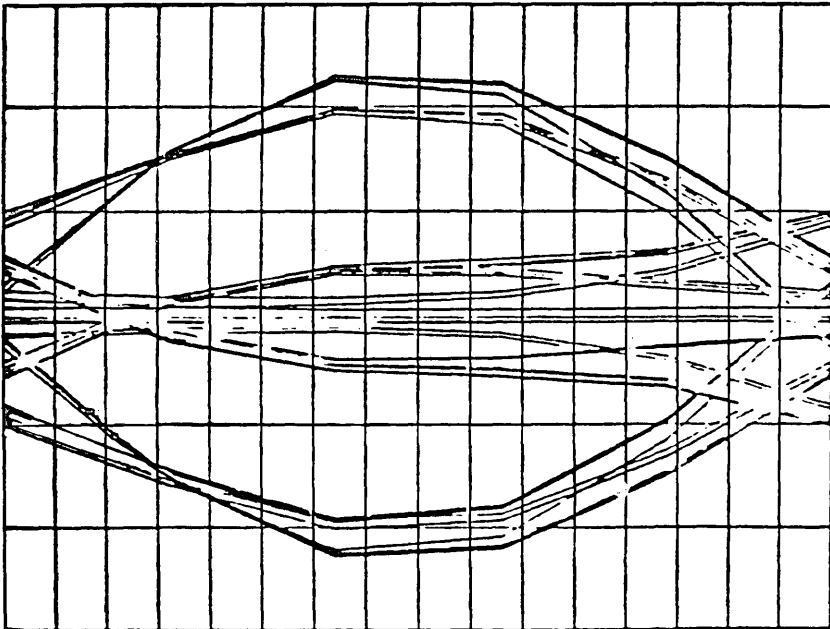


Fig. 12—Eye diagram obtained by transmission of data at 324 kb/s (for an effective bidirectional rate of 144 kb/s) in the TCM mode. The loop configuration is the same as that for the simulations in Fig. 11.

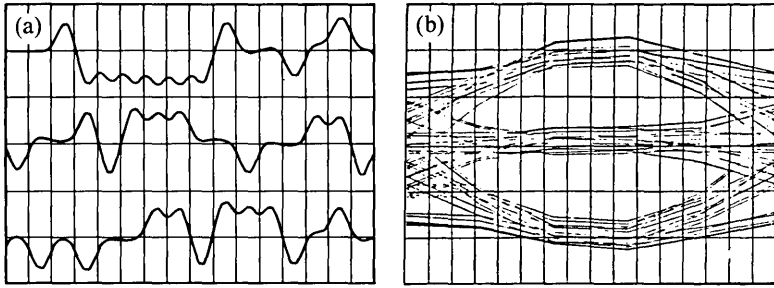


Fig. 13—Pulse pattern and eye diagram obtained by ternary code at 144 kb/s. The loop is 18 kft of No. 22 AWG cable. (a) Subscriber-side pulse pattern. (b) Subscriber-side eye diagram.

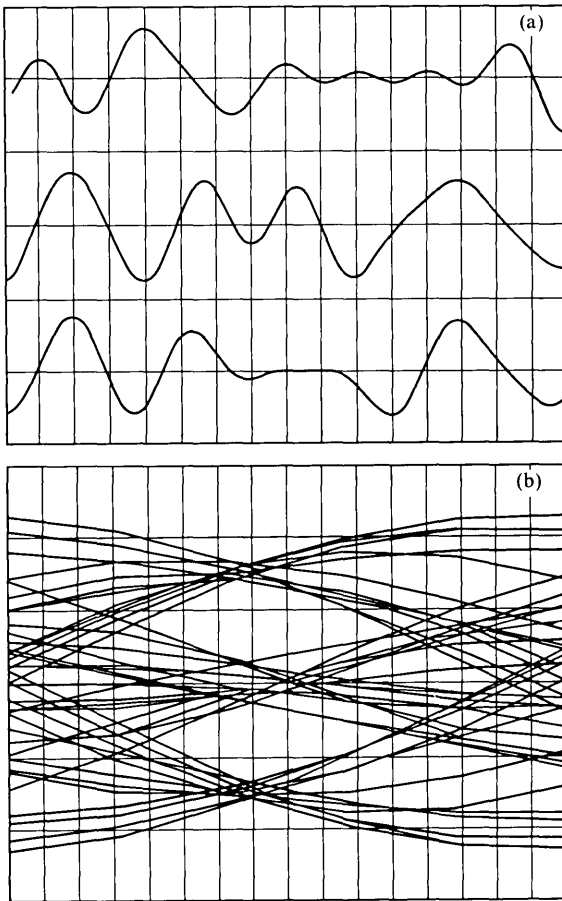


Fig. 14—Pulse pattern and eye diagram obtained by class four partial-response coding. The loop is a typical three-section loop, and the bit rate is 144 kb/s. (a) Subscriber-side received data. (b) Subscriber-side eye diagram.

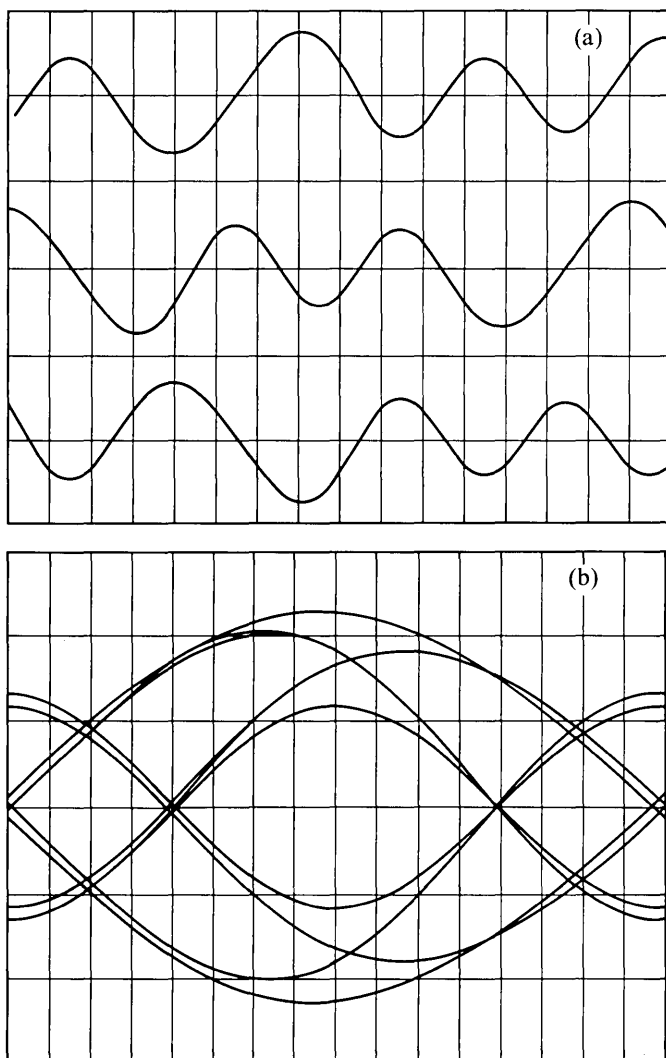


Fig. 15—Pulse pattern and eye diagram obtained by WAL-2 code. The loop configuration has nine cable sections and three bridged taps, and the bit rate is 144 kb/s. (a) Subscriber-side received data. (b) Subscriber-side eye diagram.

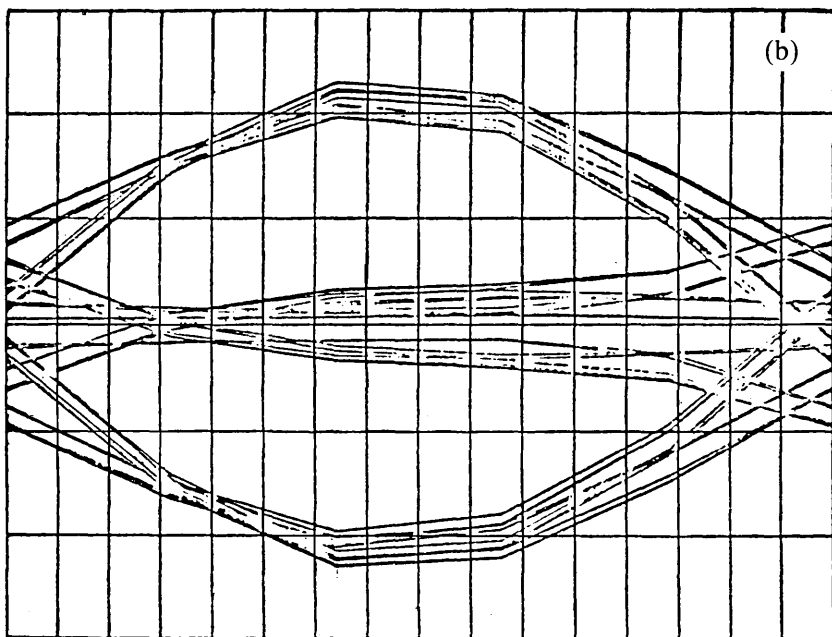
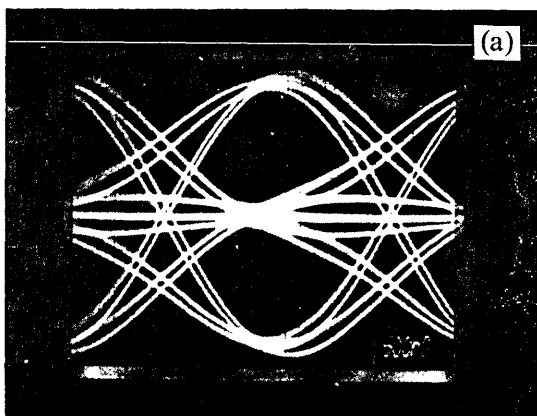


Fig. 16—Experimentally (a) and computationally (b) generated eye diagrams over 14 kft of No. 24 AWG cable. The bit rate is 324 kb/s, and the half-bit rate loop attenuation is approximately 39 dB.

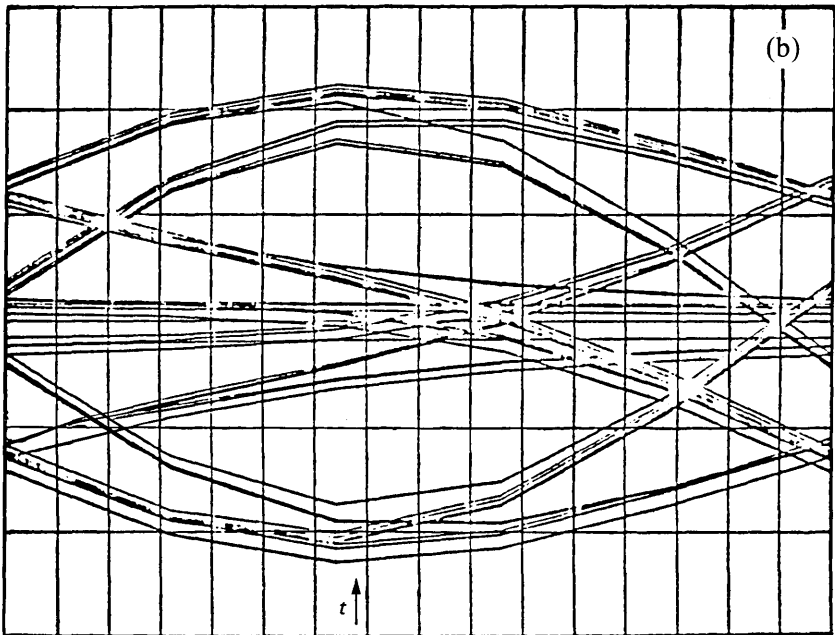
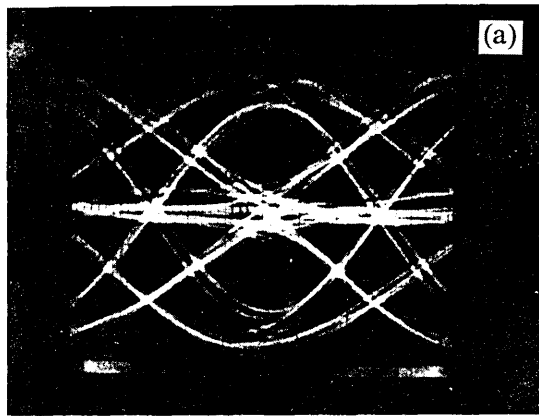


Fig. 17—Experimentally (a) and computationally (b) generated eye diagrams over a four-section (3.46 kft, 19 AWG; 8.7 kft, 24 AWG; 9.8 kft, 22 AWG; 3.46 kft, 19 AWG) loop at 324 kb/s in the rcm mode. The loop attenuation at half-bit rate is approximately 48 dB.

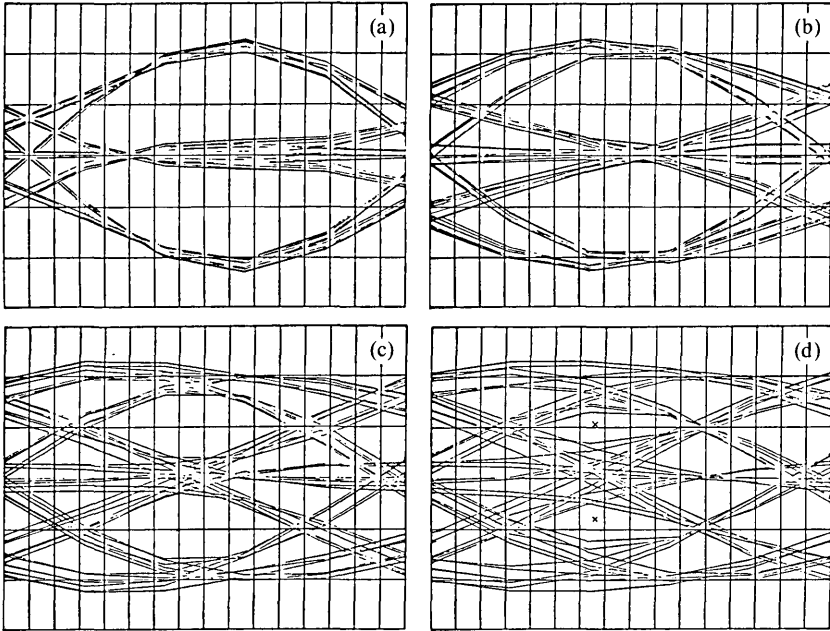


Fig. 18—Degradation of the eye diagram with an increasing number of bridged taps. (a) Subscriber-side eye diagram, no bridged taps. (b) Subscriber-side eye diagram, two bridged taps. (c) Subscriber-side eye diagram, two bridged taps. (d) Subscriber-side eye diagram, three bridged taps.

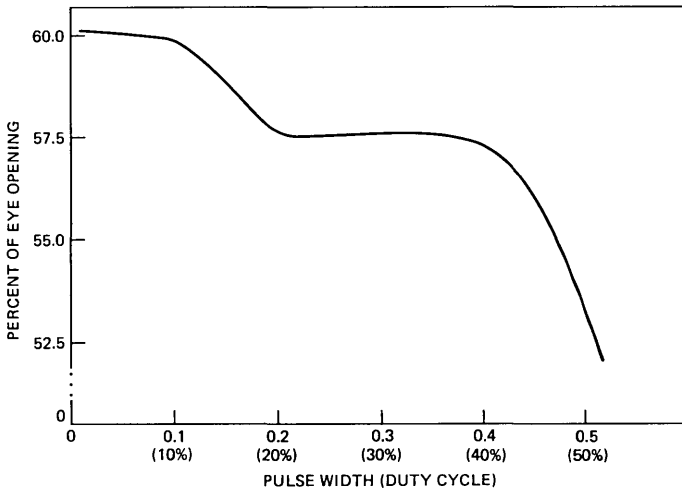


Fig. 19—Effect of varying the pulse width on the eye opening of 17,314-ft loop composed of eight discrete cable sections with a typical equalizer (see Section 5.5).

V. SUMMARY OF 1973 LOOP SURVEY SIMULATIONS UNDER VARIOUS TERMINAL CONFIGURATIONS

5.1 Introduction

The time-domain simulations yield pulse shapes and eye diagrams. The loop plant, however, consists of a widely diverse collection of loops (see Section III). Thus, we have been able to establish a computational link between the simulation programs and the loop survey data base such that the program systematically simulates the data transmission with any prescribed terminal configuration loop by loop on a statistically significant population of the Bell System loops.

5.2 From eye diagrams to eye statistics

Two hundred and forty equally spaced instants of time span the 48-pulse period over which the 48 random binary pulse data are transmitted. Hence, the pulses are approximated as a sequence of five straight lines (in the time domain). Out of the 240 instants of time for scanning 48 ones, zeros, or minus ones, 144 instants are selected for the scanning of the 48 data bits. The first set of 48 instants contains the instant at which the absolute maximum value of the incoming magnitude is located. The second set of 48 instants precedes the first 48 instants by one-fifth the pulse duration, and the third set follows the first 48 instants by one-fifth the pulse duration.

Next, for each of the three sets of 48 instants at which the scanning can be done, the data are arranged in diminishing order of magnitude. Three clusters of data are generated: (i) at the upper level, corresponding to the plus ones received in the data; (ii) at the intermediate level, corresponding to the zeros received; and (iii) at the lower (minus) level, corresponding to the minus ones received. From these three clusters seven eye statistics can be generated. In Fig. 20, the three scanning instants t_1 , t_2 , and t_3 , and the five data clusters, representing the distances $a_i b_i$, $b_i c_i$, $c_i d_i$, $d_i e_i$, and $e_i f_i$ ($i = 1, 2, \text{ or } 3$), are indicated. Next, $a_i b_i$ expressed as a proportion of the average eye height constitutes the top eye thickness, $b_i c_i$, $c_i d_i$, $d_i e_i$, and $e_i f_i$, also expressed as proportions of the average eye height, constitute the top eye opening, the central thickness, the lower eye opening, and the bottom eye thickness, respectively. Finally, the positive average eye height and negative average eye height constitute the sixth and seventh pertinent eye statistics from the eye diagram at each of three scanning instants t_i ($i = 1, 2, \text{ or } 3$). However, the scanning instant t_i is selected to have the maximum average top and bottom eye opening leading to a unique scanning instant and a unique set of seven statistics stored away for each eye. Two such seven-parameter, eye-statistical sets for each of the two eyes generated by data from CO to S and from S to CO are thus stored for each loop.

5.3 From eye statistics to scatter plots

The eye statistics of loops in the data base are generated and stored under a predefined set of terminal conditions. These eye statistics can now be displayed as a collection of scatter plots, each dot denoting a particular eye statistic of a particular loop. The top and bottom eye-opening statistics are assembled in one scatter plot. Along the X-axis, the physical length of the loop or the equivalent length of No. 22 AWG cable (or, equivalently, the loop attenuation) may be plotted. The top central and bottom eye thickness may also be plotted on one scatter plot. With two independent directions of transmission, a set of eight scatter plots are obtained for each transmission scheme. The next set of plots is obtained by separating out the loops by the number of sections. Here, the X scale is plotted by the length of the loop but compressed by two-thirds to accommodate loops in the (1, 2, 3), (4, 5, 6), or (≥ 7) sections and up to 18,000 ft on each plot. A typical example of the entire set consists of 24 scatter plots. Here, we present six such plots (Figs. 21a through 21f) obtained by transmitting data at 80 kb/s in the TCM mode at line rate of 180 (2.25×80) kb/s. In Fig. 21a, the loop length is shown on the X-axis. The eye thickness (see Section 5.2) data are plotted in the Y direction. In Fig. 21b, the eye thickness is plotted against the equivalent length of the loop in kft of No. 22 AWG cable at 55°F. At half the bit-rate frequency of 90 kHz, each division indicates about a 3.3-dB loop loss. In Figs. 21c through 21e, the eye thickness data from three sets of loops with 1-, 2-, or 3-cable sections, 4-, 5-, or 6-cable sections, and finally 7-, 8-, or ≥ 9 -cable sections are plotted.

To study the effect of the accuracy of equalization, we have generated the next family of scatter plots which indicates the eye height (also as a scatter plot), together with the eye opening and eye thickness data. In Fig. 21f, the effect of the eye height (which is allowed to change by approximately 20 percent by adjusting the equalization) on the eye thicknesses is plotted as scatter plots in the top half of the plots. In the lower half, the eye height data are plotted.

5.4 Worst loop tabulations

The scatter plots are a collection of points with each trio (Fig. 21f) or quad (Figs. 21a, etc.) representing a loop. However, it becomes necessary to identify the loops that do indeed cause failure or unexpected eye closures. For this reason, a set of programs has been developed which identifies and tabulates the loops whose eye openings lie between any two predefined percentages for any terminal configuration. For example, the composition of loops that have a ≥ 25 percent eye closure is shown in Table VI.

Table VI—Data of loop that exhibit more than 25 percent eye closure

WORST LOOP SEARCH-LOOP DETAILS— EYE CLOSURE = 25 PERCENT							
130, 5,	26, 2,						
4671, 24,	5348, 22,	671, 26,	759, 19,	4122, 22,			
199, 6,	30, 2,						
2512, 22,	2333, 24,	4238, 22,	573, 24,	7292, 22,	190, 24,		
456, 2,	29, 2,						
13643, 22,	724, 26,						
699, 3,	28, 2,						
13308, 26,	1412, 24,	990, 26,					
740, 2,	25, 2,						
11523, 22,	6224, 24,						
741, 8,	27, 2,						
7789, 26,	2998, 24,	2564, 26,	25, 24,	957, 26,	2120, 24,	141, 26,	
720, 24,							
765, 5,	29, 2,						
10694, 22,	1530, 19,	1638, 24,	303, 26,	2477, 24,			
R							

Note: The first number (130) indicates the loop number, the second number (5) indicates the number of cable sections. The third and fourth numbers indicate the percentage eye closure (26) and the direction of transmission (2 for s to co and 1 for co to s). The number pairs on the next line denote the cable length and the gauge number. Five such numbers are printed because there are five cable sections. The same data format repeats for the next six loops.

5.5 Percentage failure analysis

An alternate way to investigate the success or failure of any terminal configuration is to identify the percentage of loops in each kilofoot band that has eye closure in excess of the prechosen eye openings. Typically, eight eye-closure (2.5, 5, 7.5, 10, 12.5, 15, 20, and 30 percent) limits are defined, and there are eighteen 1-kft bands in the loop data base. Results for the 80-kb/s TCM mode transmission is shown in Table

Table VII—Percentage of loops in each kilofoot band capable of carrying data with less than the specified eye closure (CO-to-S-data)

	Percentage (Eye Closure)							
	2.5	5	7.5	10	12.5	15	20	30
0-1	0.00	0.00	0.00	0.00	0.00	100.00	100.00	100.00
1-2	0.00	0.00	0.00	0.00	7.89	100.00	100.00	100.00
2-3	0.00	0.00	0.00	0.00	89.29	100.00	100.00	100.00
3-4	0.00	0.00	0.00	46.38	98.55	100.00	100.00	100.00
4-5	0.00	0.00	1.56	96.87	100.00	100.00	100.00	100.00
5-6	0.00	0.00	54.55	96.10	100.00	100.00	100.00	100.00
6-7	0.00	0.00	59.37	92.19	98.44	100.00	100.00	100.00
7-8	0.00	1.39	52.78	95.83	100.00	100.00	100.00	100.00
8-9	0.00	0.00	10.45	89.55	94.03	98.51	100.00	100.00
9-10	0.00	0.00	7.55	73.58	86.79	100.00	100.00	100.00
10-11	0.00	5.45	40.00	56.36	70.91	89.09	100.00	100.00
11-12	0.00	28.85	40.38	55.77	61.54	73.08	100.00	100.00
12-13	0.00	34.21	52.63	63.16	68.42	76.32	89.47	100.00
13-14	0.00	9.68	32.26	54.84	67.74	70.97	80.65	100.00
14-15	0.00	15.38	26.92	50.00	57.69	73.08	92.31	100.00
15-16	0.00	9.52	23.81	42.86	47.62	57.14	66.67	100.00
16-17	0.00	0.00	50.00	83.33	83.33	83.33	83.33	100.00
17-18	0.00	6.25	25.00	37.50	43.75	50.00	62.50	100.00

VII for the co-to-s eye data. A totally perfect system would have a 100-percent result for each of the elements of the table, and a totally unacceptable system will have zeros for all the elements. Thus, the higher numbers toward the center of the table would tend to reflect the compromise in the designing terminal equipment and its cost. If the criterion is for 90 percent of the loop population to have 80 percent or better opening, the average of the number in the eighth column should be greater than or equal to 90, etc.

5.6 Simulation data for typical 64- and 144-kb/s TCM and hybrid system with and without bridged taps

Each simulation generates a large number of scatter plots and associated tables. This section gives the highlights of eight such simulations (Figs. 22 through 29). In Figs. 22a and 22b, the eye-opening and eye-thickness data for a 64-kb/s hybrid system are plotted with 30-dB echo cancellation. Figure 22 pertains to co-to-s data transmission and similar results (Figs. 23 through 29) are given under the other conditions.

Table VIII—Loop percentage failure and shortest length for failure

Rate	Mode	No Bridged Taps	With Bridged Taps
64 kb	Hybrid TCM	9.0%, 12 kft	31.2%, 5.7 kft
		0.0%, 18 kft	2.0%, 2.7 kft
144 kb	Hybrid TCM	8.4%, 9 kft	46.5%, 2.5 kft
		0.0%, 18 kft	26.1%, 0.5 kft

5.7 Discussion of the simulation results

An example of the effect of bridged taps under a hybrid mode of transmission can be identified by comparing Figs. 22 and 23 at the 64-kb/s rate or Figs. 24 and 25 at the 144-kb/s rate. Similarly, the effect of bridged taps in the TCM mode of transmission is identifiable by comparing Fig. 26 with 27, or 28 with 29 at the two data rates. Conversely, a hybrid and a TCM system can be compared at the two rates by comparing Fig. 22 against 26, or Fig. 23 against 27 for the 64-kb/s rate, and by comparing Fig. 24 against 28, or Fig. 25 against 29 for the 144-kb/s rate.

5.7.1 An example of a comparison of a TCM system with a hybrid system

The entire population of loops in the loop survey can carry bidirectional data at 64 or 144 kb/s up to 18 kft with the TCM system when the bridged taps are stripped. The eye closure in all the cases has been computed to be <42 percent. In the hybrid mode with 30-dB echo

cancellation and with similar equalization, the failure rate (criterion: eye closure >40 percent) is expected to be 9 percent at 64 kb/s, when all the bridged taps are stripped, and climb up to 31.2 percent with the bridged taps intact.

At 144 kb/s with the TCM system, all the loops (no bridged taps) carry the bidirectional data with 40 percent or less eye closure, except one single loop which exhibits a 42-percent closure. Under similar conditions, the hybrid system with 30-dB echo cancellation yields a loop failure rate of about 8.4 percent. Bridged taps deteriorate the performance of both the TCM and the hybrid systems. However, the TCM system suffers a 26.1-percent loop failure against 46.5 percent for the hybrid system with 30-dB echo cancellation.

The next significant observation is that in the hybrid system at 64 kb/s with all the bridged taps stripped, the data can be transmitted successfully on all loops up to 12 kft, and the failure rate is 8, 35, 61, 76, 66, and 81 percent in each of the 1-kft bands up to 18 kft. At 144 kb/s-data transmission on the loops with all the bridged taps stripped is successful up to about 11 kft. The failure rates for 12- to 18-kft bands have been computed as 15.4, 26.3, 25.8, 7.7, 52.4, 66.7, and 100 percent, respectively.

Further, the effect of the bridged taps forces the limitations of the loop length to 5.7 kft at 64 kb/s in the hybrid mode and to about 2.1 kft at 144 kb/s. At 64 kb/s the failure rates in each of the 1-kft bands between 5 to 18 kft are 1.3, 1.6, 8.33, 61.2, 71.7, 72.73, 69.3, 63.2, 51.6, 73.1, 76.1, 66.6, and 81.25 percent, respectively. At 144-kb/s, only the 1- and 2-kft band qualify with a 100-percent success for data transmission, and loop failure with other sixteen 1-kft bands are 3.57, 1.45, 6.25, 23.38, 35.96, 26.39, 82.09, 88.68, 70.9, 73.1, 79.47, 100, 92.31, 95.24, 100, and 100 percent, respectively. On the other hand, the TCM mode of transmission is not particularly sensitive to loop length but, instead, to the particular bridged-tap length. The hybrid system suffers twice because of (i) reflection of the transmitted signals caused by impedance mismatches, and (ii) reflections from the bridged taps in the direct transmission path. The situation becomes complicated because of the length, number, and the distribution of the bridged taps along the loop length.

5.7.2 Comparison of results for loops without and with bridged taps

Loop failure is particularly susceptible to the presence of bridged taps. In the hybrid system at 64 kb/s, the penalty is that approximately 22 percent (from 9.0 to 31.2 percent) more loops become incapable of carrying the data. In the TCM system, about 2 percent (from 0.0 to 2 percent) loops are excluded. In the hybrid system at 144-kb/s, the penalty is about 38 percent (from 8.4 to 46.5 percent) of the loops

because of the presence of the bridged taps, whereas the TCM system suffers a 26 percent (from 0.0 to 26.1 percent) increased loop failure. These results are summarized in Table VIII. The next observation is that the loop-failure percentage has very little to do with the shortest loop that fails. Stated alternatively, the failure is likely to be independent of the loop length. However, from further analysis the characteristics of the failed loops indicate that even one single-bridged tap of critical length and appropriate gauge located anywhere along its length can destroy the eye. It has been determined that the length of this bridged tap is such as to cause a delay of one (or an integer number of) pulse period (periods, to lesser extent), thus, resulting in a systematic obliteration of the eye from either direction.

The former observation is further confirmed by the fact that the shortest loop length (Table VIII) for a 144-kb/s TCM system is only 0.5 kft, whereas the loop percentage failure is about 26 percent. Similar results for the hybrid system indicate that the shortest loop length is about 2.5 kft, and the percentage failure rate is about 46 percent.

5.8 Summary of results and conclusions

We have been able to obtain the overall performance of many systems under different terminal conditions. The results presented in this paper are based on an equalizer (Section VI). In the hybrid mode of data transmission, there is reason to conclude that deterioration

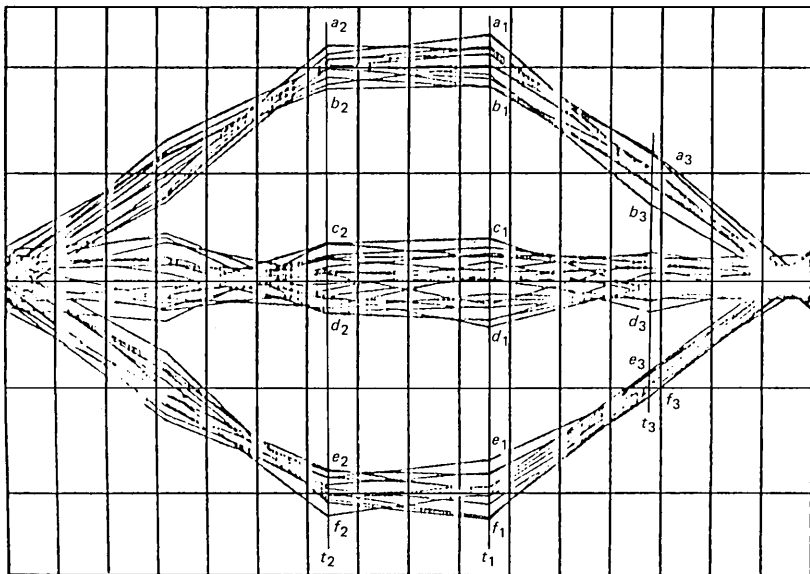


Fig. 20—Extraction of eye statistics from the eye diagram.

starts to become worse after the shortest loop length for failure is reached, whereas a similar conclusion is not evident in the TCM mode. In the former case, the eye deterioration is basically caused by (i) reflections, and (ii) delayed transmissions. While the signal strength starts to fall because of longer loop lengths, the reflected signal retains

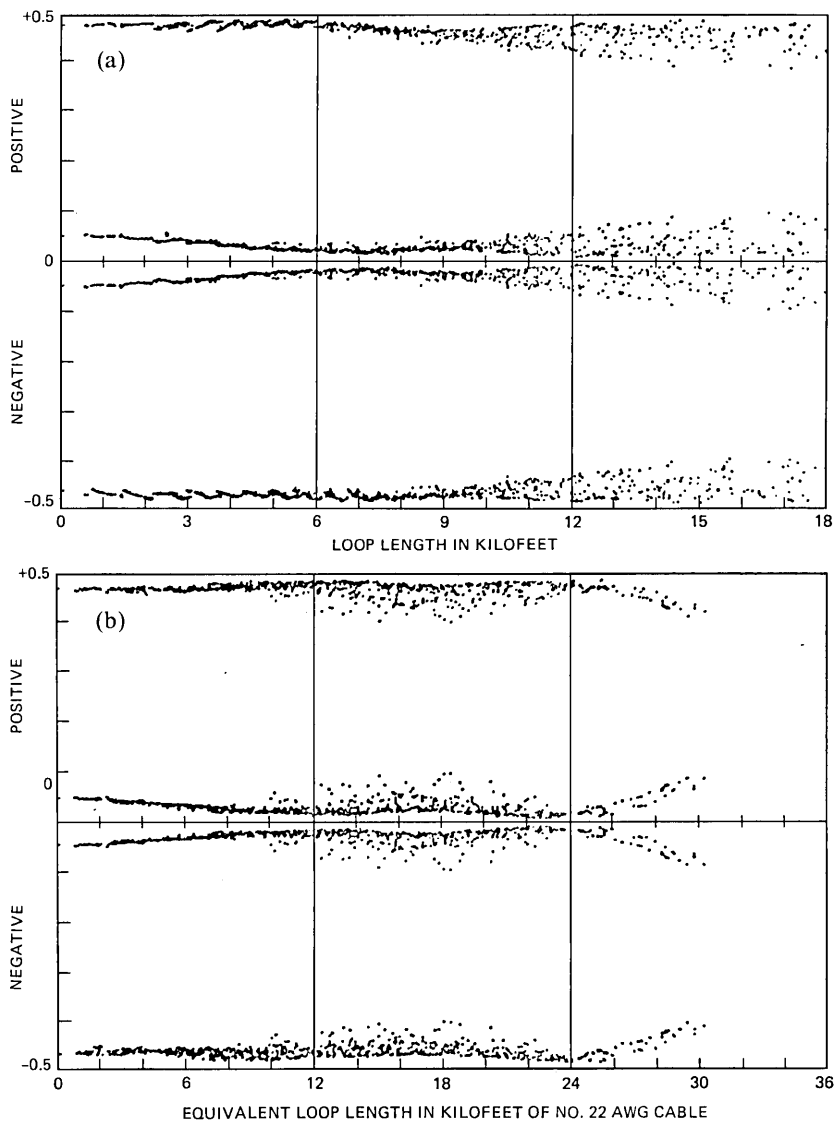


Fig. 21—Eye thickness scatter plots for 80-kb/s data transmission in the TCM mode. In the set of six figures (a through f) the data at the s end of the loops are given. (a) Eye thickness (Y-axis) versus loop length in kft (X-axis). (b) Eye thickness versus equivalent loop length (expressed in kft of No. 22 AWG cable).

its strength. The delayed transmission, which is of concern to both the hybrid and the TCM mode, can interfere with the pulse in the next time slot. In the TCM mode, the delayed transmission alone is the cause of loop performance degradation.

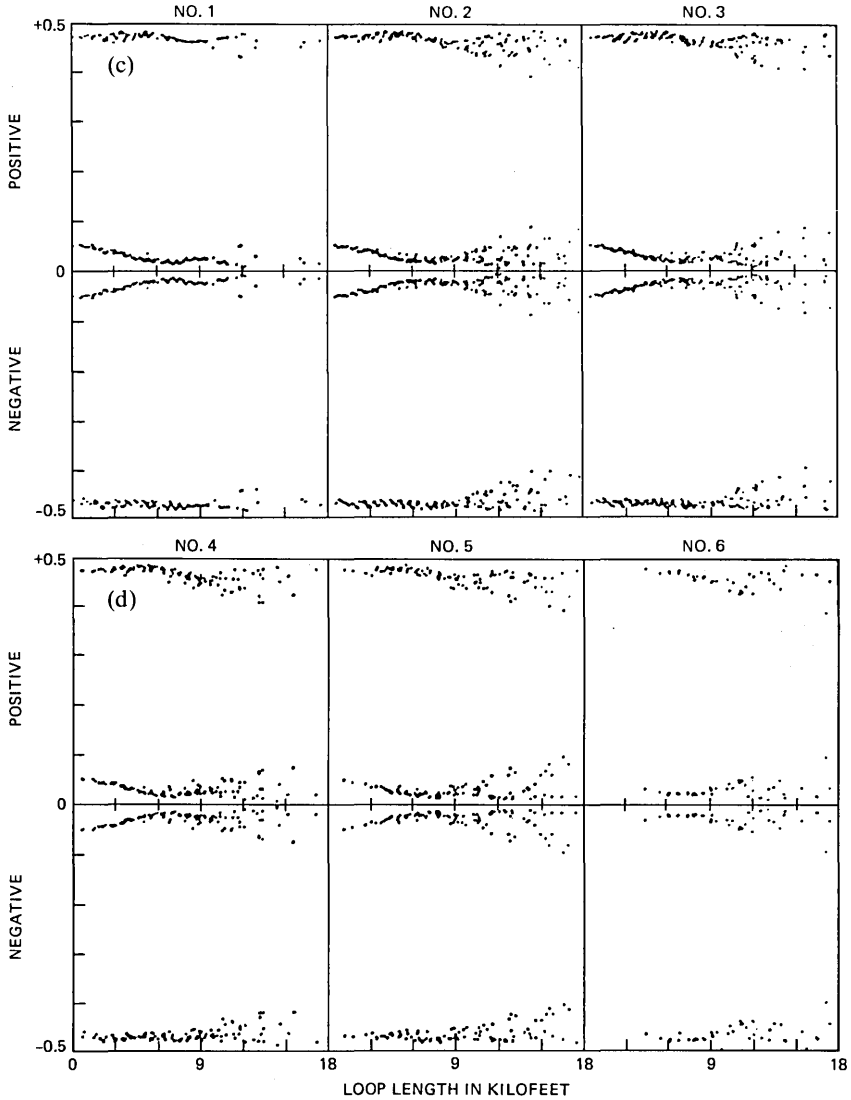


Fig. 21—(c) Eye thickness for loops with 1-, 2-, or 3-cable sections versus loop length in kft (numbers indicate number of sections). (d) Eye thickness for loops with 4-, 5-, or 6-cable sections versus loop length in kft (numbers indicate number of sections).

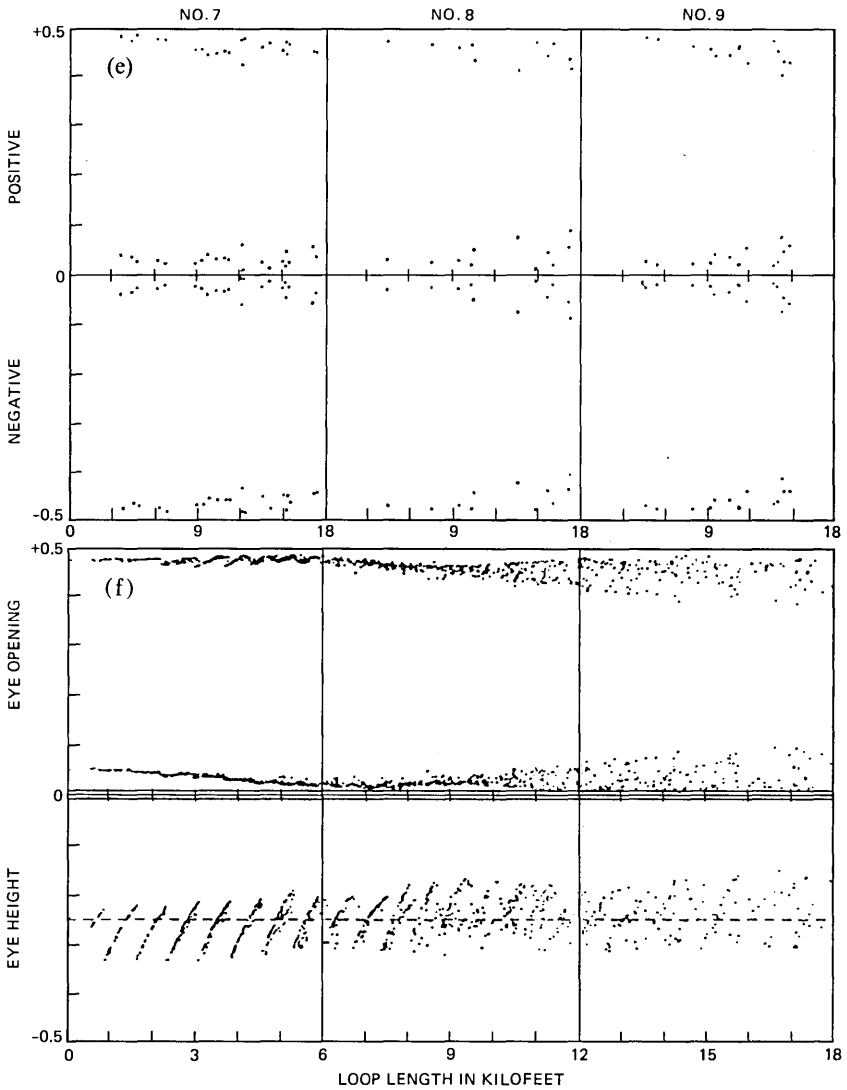


Fig. 21—(e) Eye thickness for loops with 7-, 8-, or ≥ 9 -cable sections versus loop length in kft (numbers indicate number of sections). (f) Eye thickness and eye height for all loops versus loop length in kft.

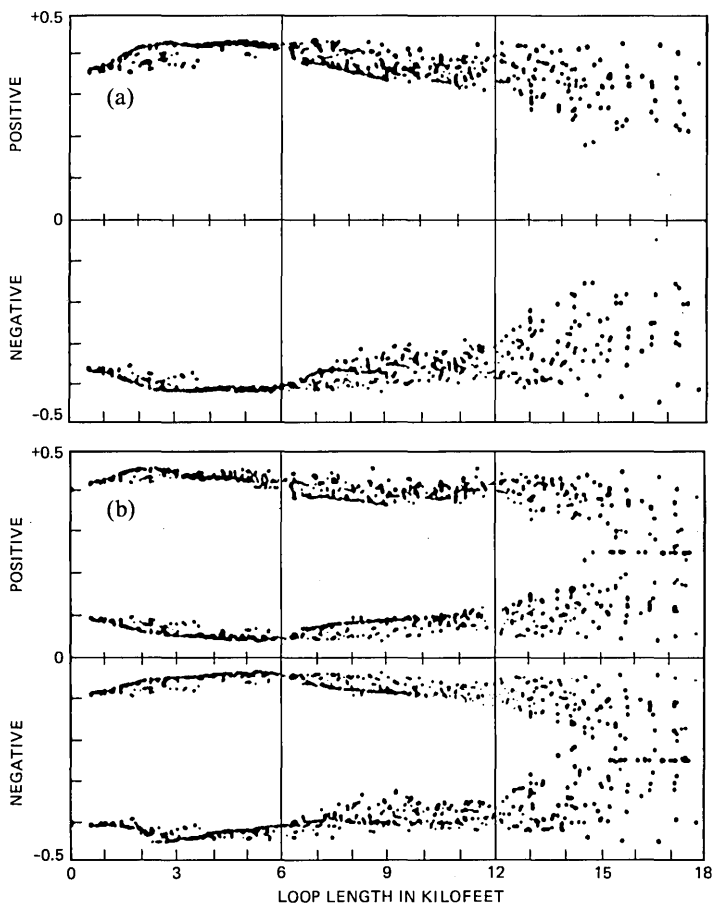


Fig. 22—Eye data scatter plots for 64-kb/s hybrid transmission with 30-dB echo cancellation. Bridged taps are stripped from the loops. Subscriber side data are given. (a) Eye opening. (b) Eye thickness.

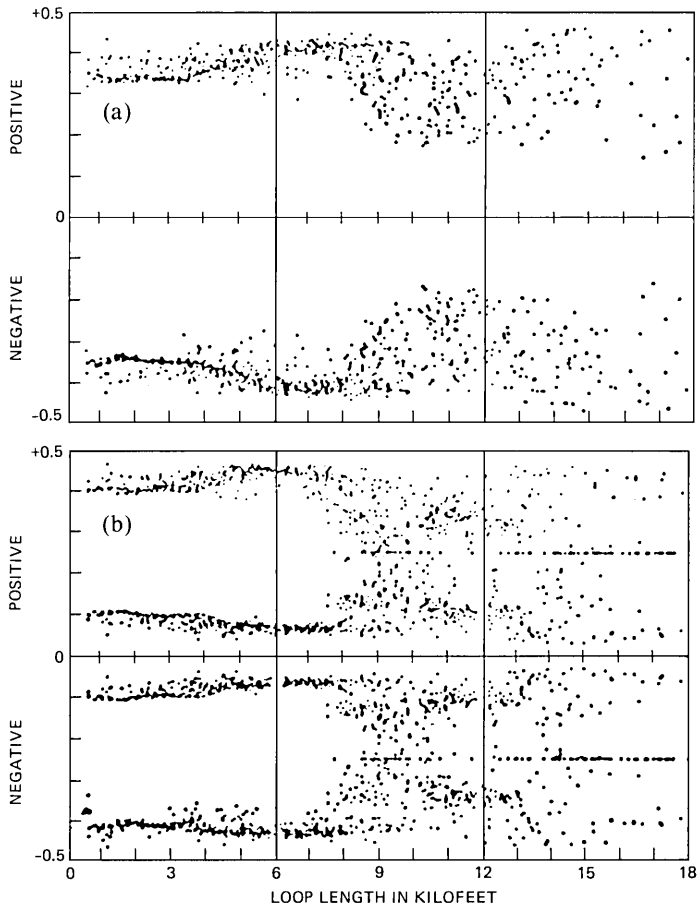


Fig. 23—Eye data scatter plots for 64-kb/s hybrid transmission with 30-dB echo cancellation. Bridged taps are left intact. Subscriber side data are given. (a) Eye opening. (b) Eye thickness.

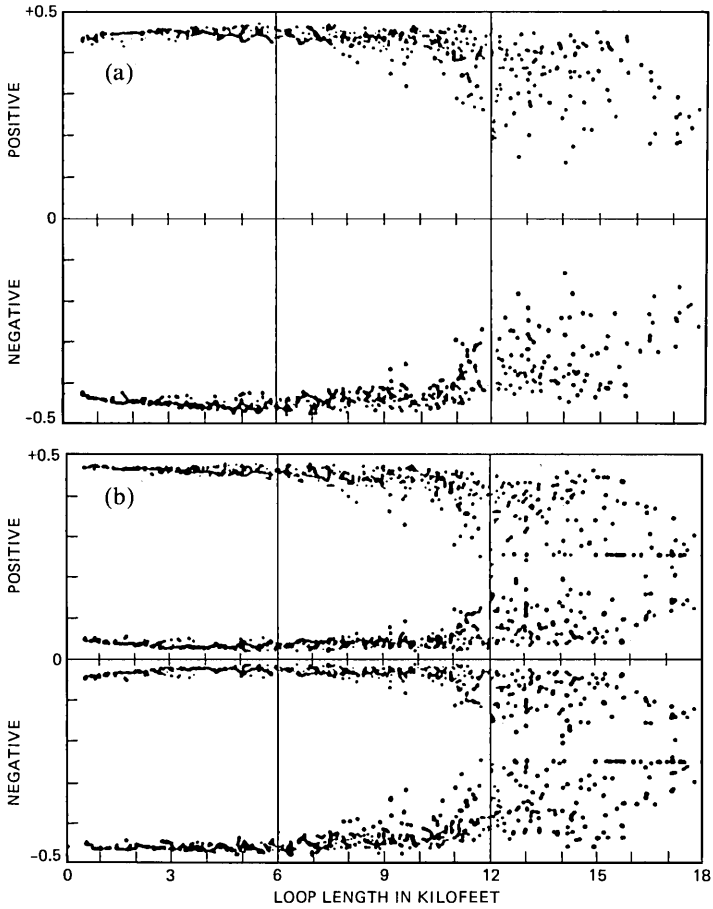


Fig. 24—Eye data scatter plots for 144-kb/s hybrid transmission with 30-dB echo cancellation. Bridged taps are stripped from the loops. Subscriber side data are given. (a) Eye opening. (b) Eye thickness.

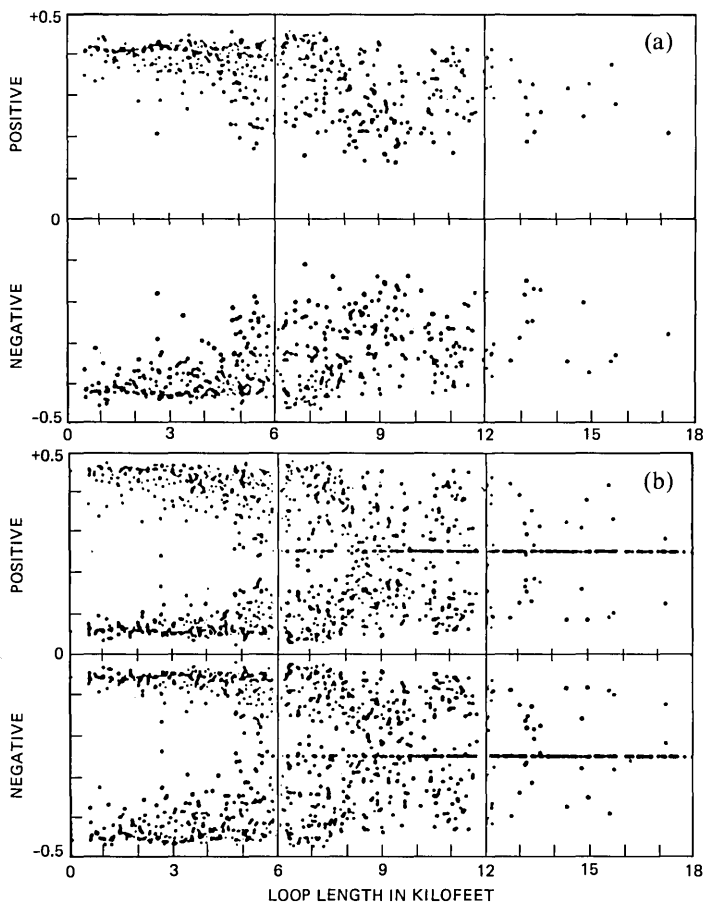


Fig. 25—Eye data scatter plots for 144-kb/s hybrid transmission with 30-dB echo cancellation. Bridged taps are left intact. Subscriber side data are depicted. (a) Eye opening. (b) Eye thickness.

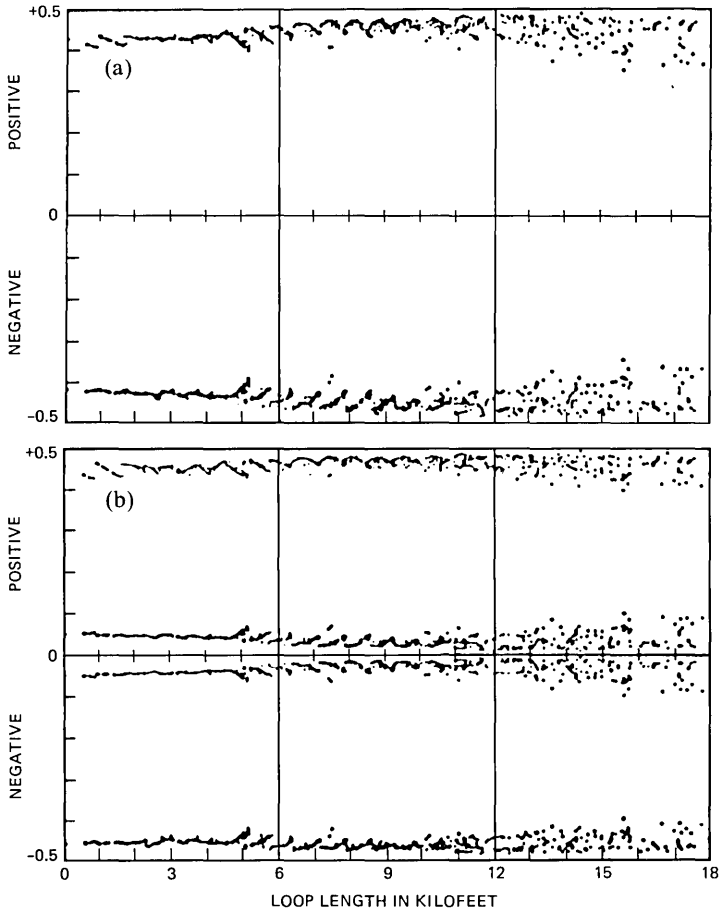


Fig. 26—Eye data scatter plots for 64-kb/s TCM-mode transmission (actual line rate is 144 kb/s). Bridged taps are stripped from the loops. Subscriber side data are given. (a) Eye opening. (b) Eye thickness.

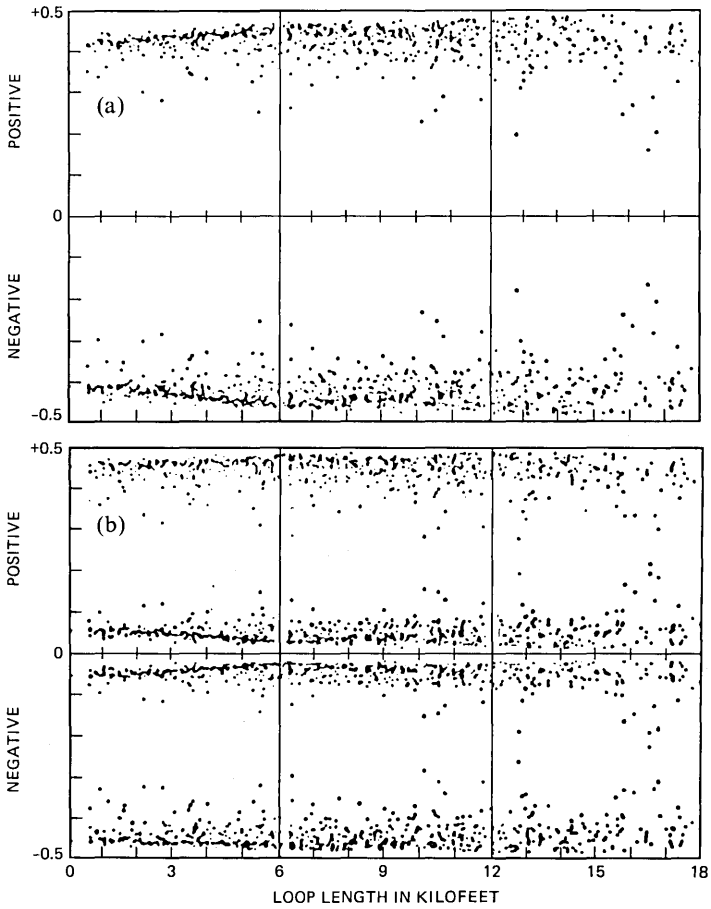


Fig. 27—Eye data scatter plots for 64-kb/s TCM-mode transmission (actual line rate is 144 kb/s). Bridged taps are left intact. Subscriber side data are given. (a) Eye opening. (b) Eye thickness.

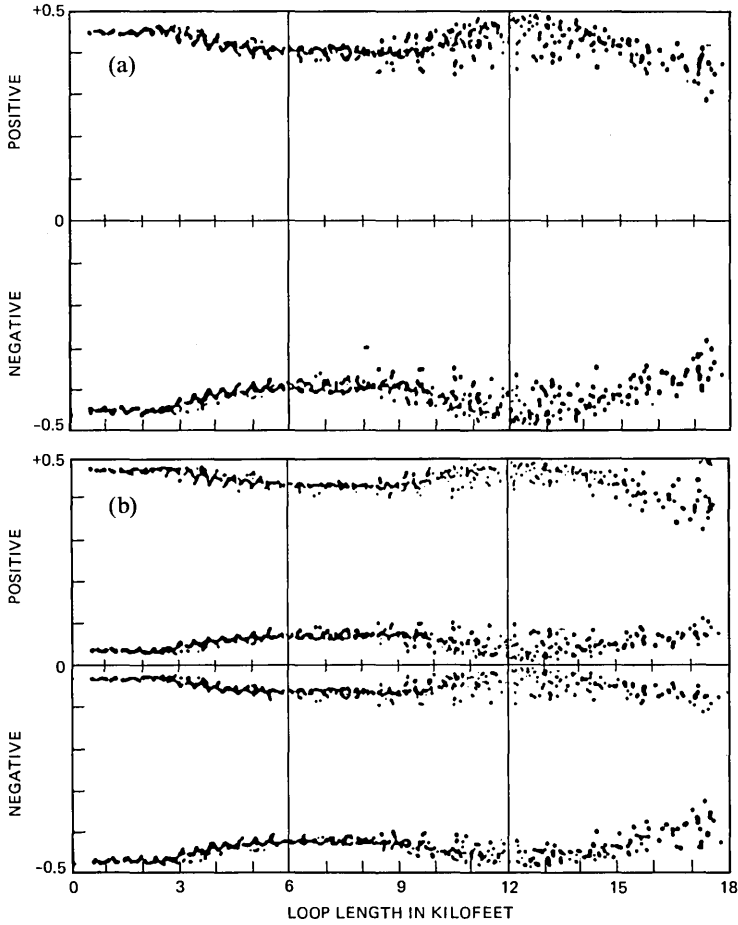


Fig. 28—Eye data scatter plots for 144-kb/s TCM-mode transmission (actual line rate is 324 kb/s). Bridged taps are stripped from the loops. Subscriber side data are given. (a) Eye opening. (b) Eye thickness.

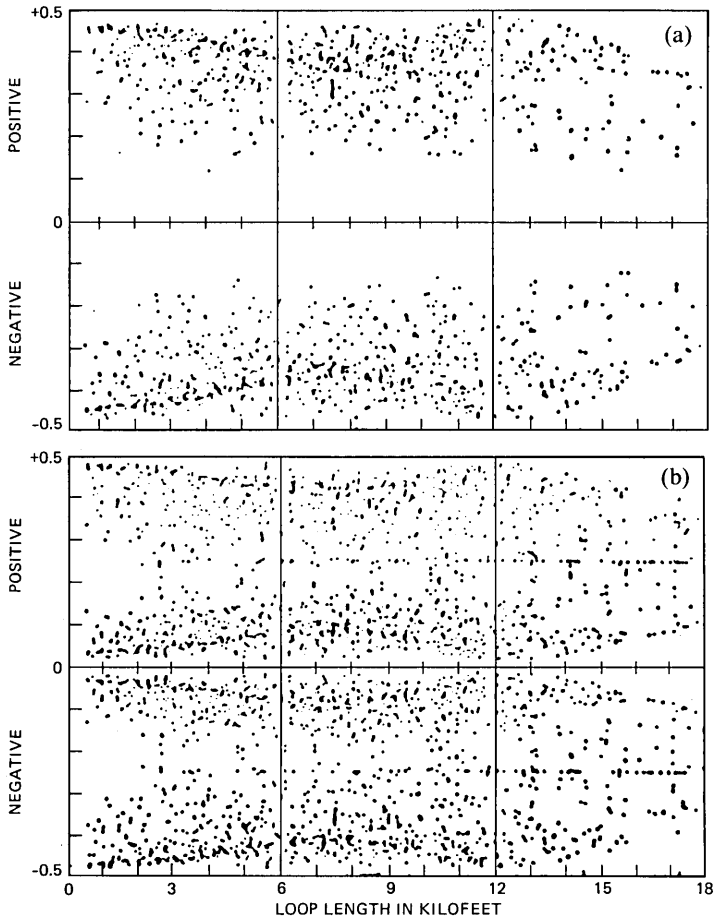


Fig. 29—Eye data scatter plots for 144-kb/s TCM-mode transmission (actual line rate is 324 kb/s). Bridged taps are left intact. Subscriber side data are given. (a) Eye opening. (b) Eye thickness.

VI. ANALYSIS, DESIGN OPTIMIZATION, AND EVALUATION OF EQUALIZERS

6.1 Introduction

Four equalizer designs are analyzed and evaluated for their application to data transmission in the range of 56 to 144 kb/s. The first design is for 144-kb/s transmission. The second design is specifically for a line rate* of 324 kb/s. The remaining two designs are intended for a range of TCM applications in the region of 126 (2.25×56) kb/s to 324 (2.25×144) kb/s. Realizations of the designs are discussed and

* The information rate is 144 kb/s, but the line rate for this design is enhanced to 324 kb/s because of the TCM operation.

their actual performances are computed by a series of simulation programs discussed in Sections II, III, and IV. To prevent cable mismatch effects (which are indeed present in a hybrid system) from overshadowing the influence of equalization, we present simulation results utilizing continuous unidirectional transmission, thus, focusing on the performance of the equalizer. The equalizers then can be utilized in either a hybrid or a TCM-mode system. The eye-opening scatter plots obtained by analyzing the system performance on actual loops taken from the loop survey are used as the ultimate criteria to judge the equalizer quality.

A digital-system equalizer attempts to undo the effect of cable attenuation and restore the pulse shape at the receiver; however, pulse shape results from a composite of the amplitudes of many frequency components, their phase relationships, and their harmonic relationships. Hence, a perfect pulse restoration at all bit rates entails perfect responses at all frequencies. In essence, an inverse loop circuit constitutes a perfect equalizer circuit. However, loops, bit rates, and coding algorithms are each numerous and uncorrelated, thus, causing additional elements of complexity in the design of equalizers. Even though the results presented here are for the bipolar code, it should be noted that for other codes, the region of spectral emphasis for matching cable loss and equalizer gain will be dictated by the bandwidth requirement of the particular code.

6.2 Three-section, 18,000-ft equalizer

6.2.1 Circuit configuration and representation

Each of the three sections has a five-pole, five-zero circuit. The location of these poles and zeros are obtained by the solution of five simultaneous equations that are formulated to yield exact equalizations of 6,000 ft of No. 22 AWG cable at five discrete frequencies (1, 2, 10, 50, and 100 kHz). Further, the transfer function of the RC circuit is controlled by the gain of an operational amplifier, and this gain is adjusted by yield equalization of loops or loop sections under 6000 ft of cable. Thus, loops of any length under 18,000 ft can be equalized by cascading one, two, or three sections of this equalizer and appropriately adjusting the gains on the three sections of the equalizer. Variation in temperatures is converted to a variation in effective loop length, and the eye height is maintained by the gains of the three sections of the equalizer.

6.2.2 Equalizer performance with composite cables

The performance evaluation of this equalizer with composite cables is limited to a study of eye openings as the composition of the cables is changed gradually for an overall loop length of 18 kft. Two major

simulations are performed. In the first simulation, a loop comprising Nos. 22 and 24 AWG cables with an overall length of 18 kft is chosen. At one extreme, the loop is totally composed of No. 22 AWG cable; conversely, at the other extreme, the loop consists of No. 24 AWG cable. These two cases are presented at the left and right sides of the X-axis in Fig. 30. As the distance along the X-axis is increased, the No. 22 AWG cable is shortened and the length of No. 24 AWG cable is increased. The eye openings are plotted on the Y-axis. The two eyes generated for alternate bipolar coding yield two data points for each loop composition.

Similar results for Nos. 19 and 26 AWG cable compositions are shown in Fig. 31. The simulations are carried out at 144 kb/s. The performance of the equalizer and the quality of the filter are both reflected by the eye opening. The first filter at the transmitting end has the 3-dB point located at half the bit rate. The second identical filter is located at the receiver end. This pair of filters essentially yields a pulse shape, with the amplitude rising from zero and steadily reaching a peak and diminishing to zero, one pulse period after its peak.

In Figs. 30 and 31, a pair of points along each vertical line represents an independent simulation for the appropriate composition of cables. Eye diagrams are internally generated and the seven eye statistics (Section 5.2) are extracted. For each loop, two dots representing the positive and negative eye opening are plotted. From Figs. 30 and 31, it can be expected that the equalizer compensates 18 kft of Nos. 19, 22, 24, and 26 AWG cables with 70, 80, 70, and 0 percent eye openings, respectively. With only No. 26 AWG loops, independent simulations indicate that this equalizer provides an eye opening of about 40 percent with 12 kft loops. It is also interesting to note that the eye openings in either direction of transmission are roughly the same because the effects of reflections (as they occur in a hybrid system) are eliminated, thus, emphasizing only equalizer and filter performances. Proper filter performance is assured by a 100-percent eye opening at zero cable length. The equalizer performance with the loops in the data base may be examined by studying the scatter plots of Figs. 32a and 32b. The eye openings (Fig. 32a) and the eye thickness (Fig. 32b) are generated by the transmission of random data with bipolar codes.

6.3 Four-section, 20,000-ft equalizer

6.3.1 Circuit design

The range and spectrum of equalization are both enhanced for this design. As opposed to the former design, a "staged turn-on" algorithm has been used for more effective equalization. In this mode, the four sections are turned on, one by one, as the range of each section is exhausted by the loop attenuation. Further, the equalization is also

forced out to a frequency of 250 kHz, thus, increasing the total maximum gain from 60 dB for the former design, to about 72 dB. Each section of this six-pole, six-zero equalizer has exact equalization at 1, 2, 10, 50, 100, and 250 kHz for 5000 ft of No. 22 AWG loop.

6.3.2 Equalization data for loop attenuations

The performance of this equalizer is studied at three frequencies. The attenuation of the 831, 1973 survey loops (Section III), in the truncated data base are computed at frequencies of 56, 144, and 324 kHz. Next, the equalization gain for each of the loops at the three corresponding frequencies is also computed. As a next step, the equivalent length of the composite loops, in terms of No. 22 AWG cable, is calculated and the loop attenuations are now plotted in Figs. 33a, 34a, and 35a for these three frequencies at 56, 144, and 324 kHz, respectively. These scatter plots represent approximate straight lines since the gauge-length conversions (see Section 3.4) bring the individual loop attenuation points parallel to the *X*-axis to roughly fall along the No. 22 AWG cable attenuation line. Finally, the equalizer gains for all the loops are also plotted in Figs. 33b, 34b, and 35b. For perfect equalization, the lines in Figs. 33a and 33b, 34a and 34b, and 35a and 35b should be collinear. The imperfection of equalization is indicated by the noncollinearity of these lines or, for that matter, the nonconcurrency of these individual points.

6.3.3 The 1973 loop survey eye diagram performance

Simulations at 324 kb/s (the TCM mode rate corresponding to 144-kb/s bidirectional hybrid rate) and at 126 kb/s (the TCM mode rate corresponding to 56-kb/s bidirectional hybrid rate) are presented to evaluate the performance of this equalizer. In Fig. 36, the eye openings are shown as a scatter plot of the 1973 survey loops when transmitting data at 324 kb/s in the TCM mode. These results correspond to co-to-s data transmission. Similar results generated for s-to-co transmission are not presented. Figure 37 shows the eye-opening data when the system is excited with 126-kb/s TCM mode.

6.4 Limited-range, single-pole equalizer

In the previous two designs the equalizer gain exactly compensates the cable loss at specific frequencies (five for the first, six for the second design) and at specific cable lengths (6 kft of No. 22 AWG and 5 kft of No. 22 AWG cables). Variations because of length are accomplished by changing the gain control on the operational amplifiers. Equalizers reported in Sections 6.4 and 6.5 are designed by broadly matching the shape of the cable loss with frequency against the gain of the equalizer in the frequency domain. Overall gain changed to

accommodate different cable lengths are adjusted by changing diode resistances. This, in turn, adjusts the gain of the operational amplifier without drastically changing the frequency characteristics. A single pole and an adjustable zero-type of transfer function is used to generate a suitable equalization range over a 6- to 36-dB cable loss. When these poles and zero's are redistributed, a corresponding range of equalization may be obtained for these lower frequency applications. The application considered here is for a 324-kb/s TCM-mode data transmission. Cable attenuations and equalizer gains at the half-baud rate (162 kHz) are both plotted in Fig. 38. The dotted lines indicate the cable attenuations of the Nos. 19, 22, 24, and 26 AWG cables. The full lines indicate the corresponding equalizer gain. The chief limiting factor is the range of equalization. The equalizer saturating at about 36 dB cannot compensate for cable losses greater than about 10.7 kft of No. 26 AWG at 162 kHz. Our study of the loop plant indicates that a considerable fraction of loops extends beyond this distance. Hence, the design of this particular type of equalizer has been abandoned for the 324-kb/s TCM mode of bidirectional data transmission. A limited study of eye opening data has indicated that only 30 to 40% of the loops would carry bidirectional data with a 60-percent or better eye opening at 324-kb/s TCM-mode data transmission.

6.5 Enhanced-range, wider-frequency, optimized equalizer

The design philosophy for this equalizer is the same as that for the former equalizer; However, two cascaded, shaped gain amplifiers are used in this case. The first has a low-frequency zero and two higher-frequency poles, while the second has a low-frequency zero, another right-half-plane zero, and a pair of complex poles. However, optimization by the incremental displacement of poles and zeros is essential to follow the loop attenuation at frequencies of interest.

6.5.1 Optimization strategy

An optimization approach in both the frequency and distance domains is simultaneously attempted to match the equalizer gain against the cable loss. First, half-baud rate frequency cable attenuation lines are generated for Nos. 19, 22, 24, and 26 AWG cables. Then the gauge conversion factors (see Section 3.4) at this frequency are used as a basis of all the gauge conversions. The maximum equivalent loop length (as extracted from the loop survey) is then determined to correspond to about 16.7 kft of No. 26 AWG cable. Next, No. 26 AWG cable losses at 5, 10, 50, 100, 150, 200, and 250 kHz are generated by the primary characteristics of the No. 26 AWG cable (see dashed lines in Figs. 39a and 39b). The poles and zeros of the equalizer are given incremental changes such that the equalizer gain and the cable losses

are almost collinear at about the half-baud rate frequency over the span of one-half to two-thirds of maximum cable length (see Figs. 39a and 39b). The first step of optimization is more or less easily achieved; however, in the second step of shifting the R's and C's of the equalizer circuit such that the noncollinearity of the equalizer gain and the cable loss at the low-frequency end of the spectrum has to be weighed against the noncollinearity of the two at the higher end of the spectrum. The optimization becomes complicated by the fact that both the low- and high-frequency noncollinearities themselves display crossovers in the distance domain. Further, the crossover at the low-frequency end has an intersection going from a lower gain to a higher gain as the length of the cable is increased. On the other hand, the crossover at the higher frequency follows an opposite type of characteristic changing from higher gain to lower gain as the distance increases. Thus, a large number of trials are necessary to achieve a satisfactory compromise.

The effect of this optimization implies one distinct effect on the single-pulse response. At lower cable lengths, there is a distinct overshoot because of the higher frequency over equalization and the lower frequency under equalization. Conversely, at longer cable lengths there is a tail left behind in the single-pulse response because of lower frequency over equalization and higher frequency under equalization. But there is a certain range of lengths at which the single-pulse response approaches perfection. We have trapped and exploited this perfection to be about two-thirds the maximum cable length. Thus, the scatter plot generated by this type of equalizer shows nearly 100 percent eye openings (to be discussed next) in the central one-third span of the loops. This type of equalizer behavior is a distinct contrast to those discussed in Sections 6.2 and 6.3. Further, it is consistently good over a range of 126 to 324 kb/s.

6.5.2 Selected loop performance

At 55 ft of No. 24 AWG cable, the eye diagram is imperfect. The cable distortion component can be ruled out at this minimal length. However, in our effort to reduce the circuit complexity, we have eliminated the transmit filter and optimized the pulse width at about 40 percent of the pulse period.* The harmonics of this pulse shape are affected by the receiver filter and by the very slight effect of the equalizer. This has been understood to be the reason for the slight imperfection of the eye diagram shown in Fig. 40 at 324-kb/s operation.

* The pulse width for the best eye opening was found to exhibit broad insensitivity in the range of 35 to 42 percent of the pulse period. Hence, for all the simulations, we have held the transmit pulse width at 40 percent and retained a half-baud rate 3 dB down four-section Bessel filter at the receiver end of the loop.

A typical loop response around 6 kft is presented in Fig. 41 at 324 kb/s. In Fig. 41, a seven-section loop with an overall length of 6093 ft is chosen at 60°F. The eye diagram* is relatively the same from both directions of transmission.

Two loops around 12 kft show the response of the equalizer. In Fig. 42, the eye closure is about 18.7 percent at 324 kb/s. This loop is also composed of seven sections and is the worst loop in that region of overall loop lengths. The best system performance also takes place around this length, with a single-section loop with an 11,998-ft No. 26 AWG cable as shown in Fig. 43. The eye closure is only 3 percent, and the response is consistent with the design of the equalizer as discussed in Section 6.5.1.

In Fig. 44, the worst loop (17,314 ft loop) response is shown. The eye closures are about 43 and 42.3 percent for the two sides of transmission, and one can visualize the presence of long tails left behind single pulses in these two eye diagrams.

6.5.3 The 1973 loop survey eye diagram performance

The loops in the truncated loop survey data base have been simulated at four different TCM frequencies (126, 162, 216, and 324 kb/s to correspond to full-duplex bidirectional rates of 56, 72, 96, and 144 kb/s). The scatter plots of eye openings are plotted in Figs. 45, 46, 47, and 48. All these scatter plots exhibit a pattern yielding the best eye openings in the area of the 8 to 13 kft length rather than at about zero length. This particular performance is because of the equalizer optimization strategy.

6.6 Conclusions

The design of the equalizer has a profound effect on the capability of the loops to transmit the digital data. Here, we have compared the various design strategies and studied their effects. An equalizer design using the presently available configurations was optimized for a center frequency of 81 kHz to correspond to 162-kb/s TCM mode. However, a reoptimization of this design at 126 and 324 kb/s was deemed unnecessary because of its satisfactory performance. The optimization procedure described here should prove valuable for the design and implementation of any equalizer configuration, provided its maximum range is adequate for the attenuation expected from the longest of the loops. Effects of cable-bridged taps, impulse noise, and crosstalk on the error rate of the data transmission are not included in this study. If these effects limit the maximum range of equalization, then any of the

* The eye closure is 21.1 percent for the co-to-s eye diagram and 21.4 percent for the s-to-co eye diagram.

proposed designs may be effectively used by employing the optimization strategy presented in this paper.

All the simulation results presented here are for the bipolar code. However, it can be visualized that the design philosophy and the optimization techniques are universal to the extent that the region of spectral emphasis (Figs. 39a and 39b) will be dictated by the bandwidth requirements of the particular code.

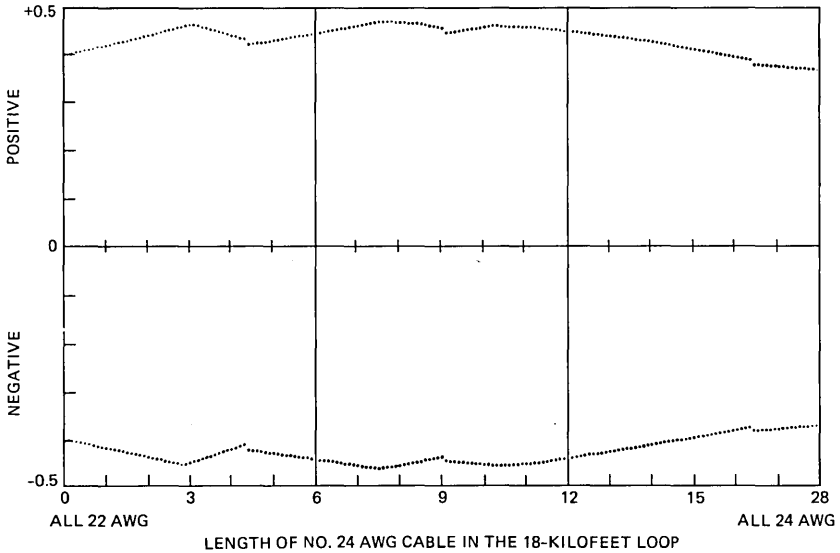


Fig. 30—Eye openings with Nos. 22 and 24 AWG composite cable loops having a total length of 18 kft (144 kb/s).

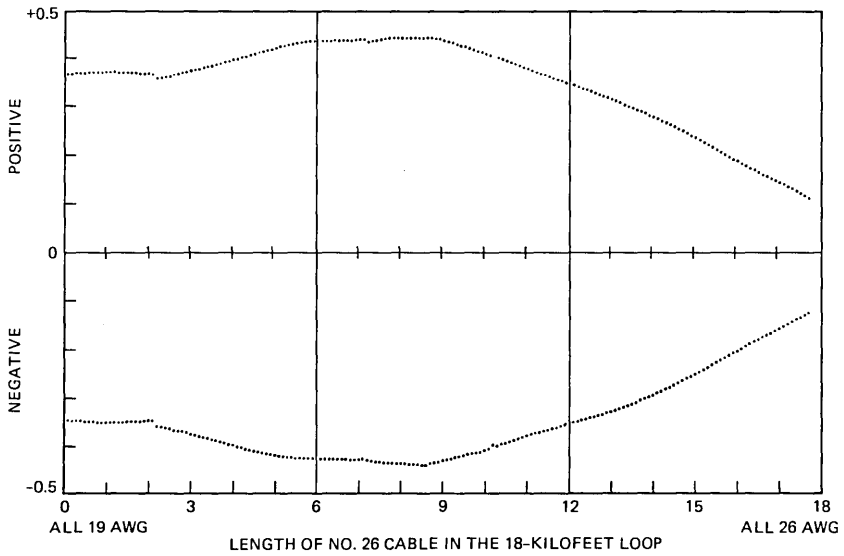


Fig. 31—Eye openings with Nos. 19 and 26 AWG composite cable loops having a total length of 18 kft (144 kb/s).

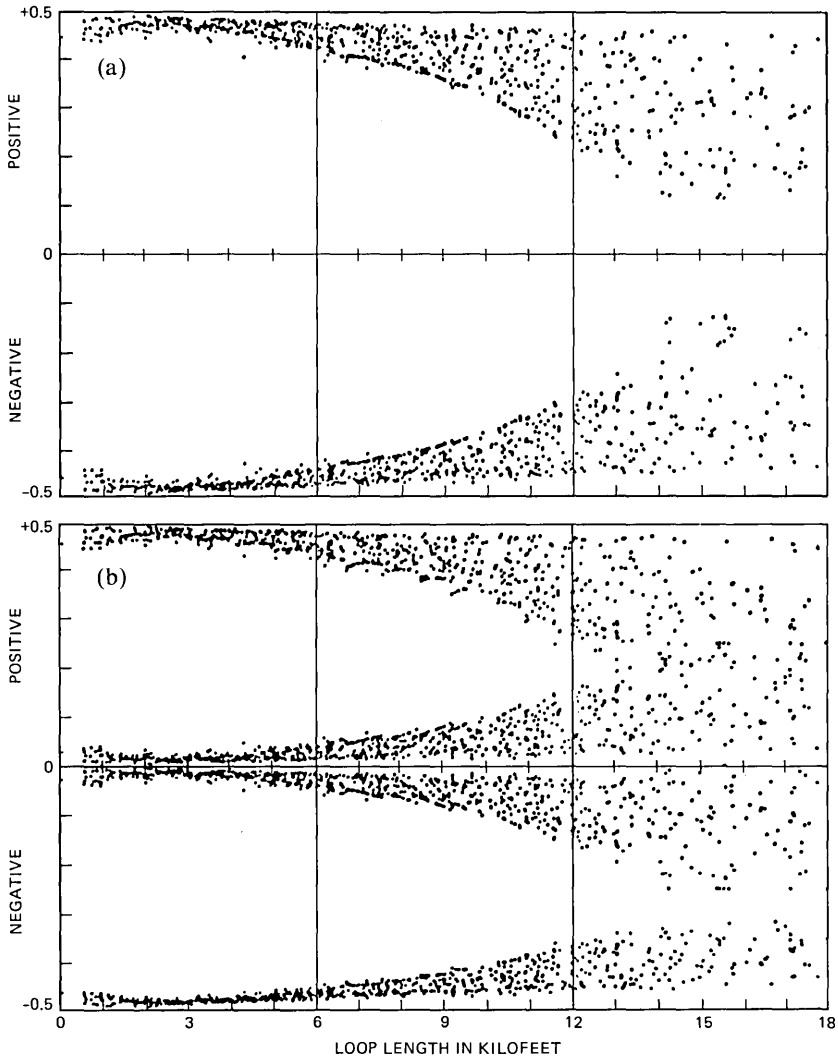


Fig. 32—Eye data scatter plot obtained by the simulation of 1973 survey loops with the three-section, 18,000-ft equalizer at 144 kb/s. (a) Eye opening. (b) Eye thickness.

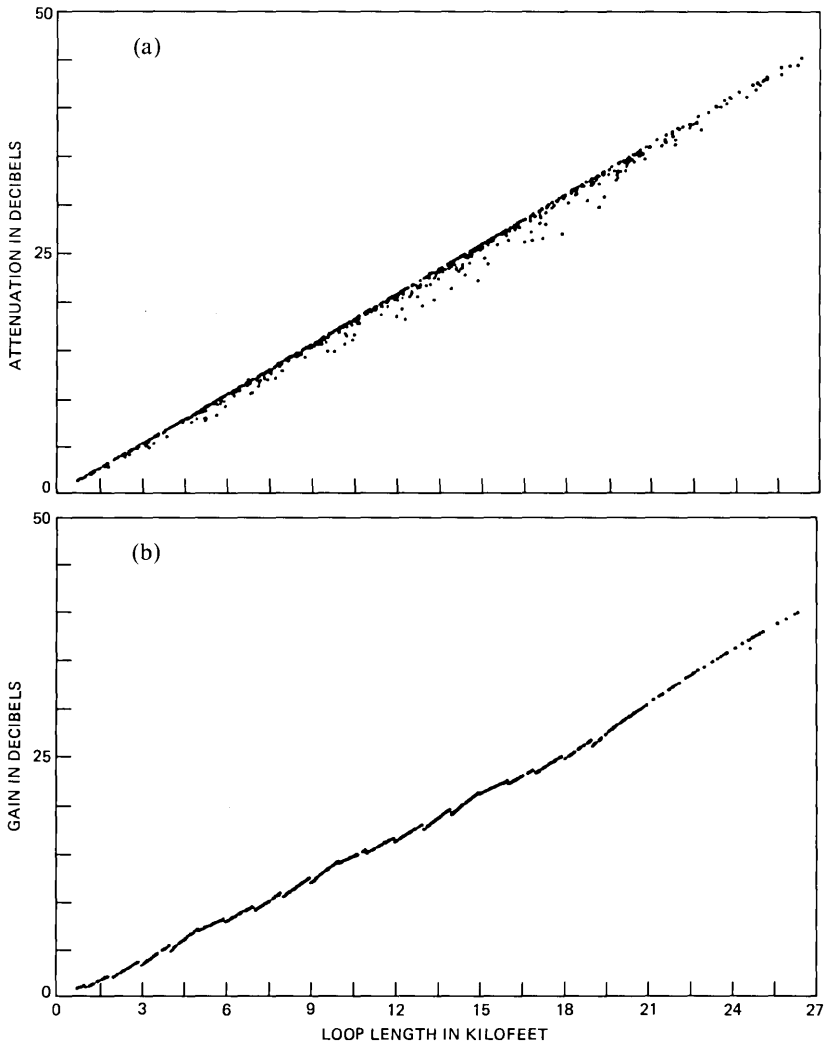


Fig. 33—Comparison of loop attenuations and equalizer gains for 1973 loop survey at 56 kHz plotted against the loop length expressed in equivalent kft of No. 22 AWG cable. Scale on the Y-axis is 5 dB/division, and on the X-axis it is 1.5 kft/division. (a) Loop attenuation. (b) Equalizer gain.

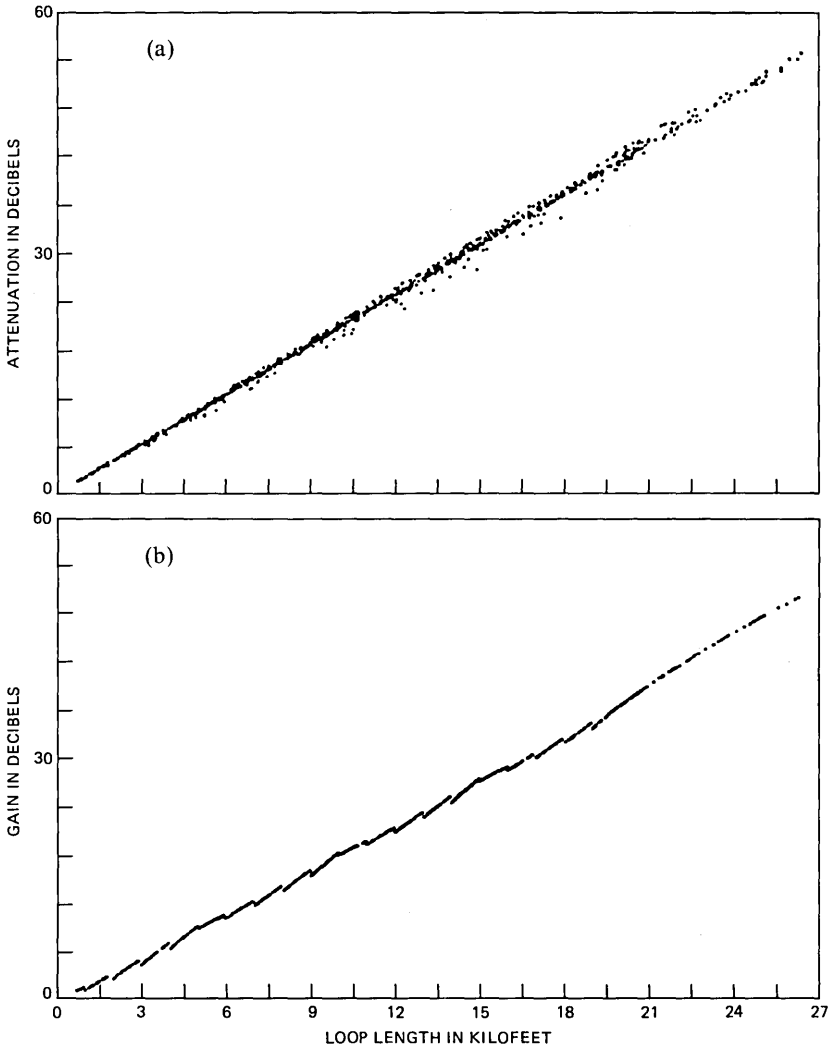


Fig. 34—Comparison of loop attenuations and equalizer gains for various loops at 144 kHz. The Y-axis scale is 6 dB/division. (a) Loop attenuation. (b) Equalizer gain.

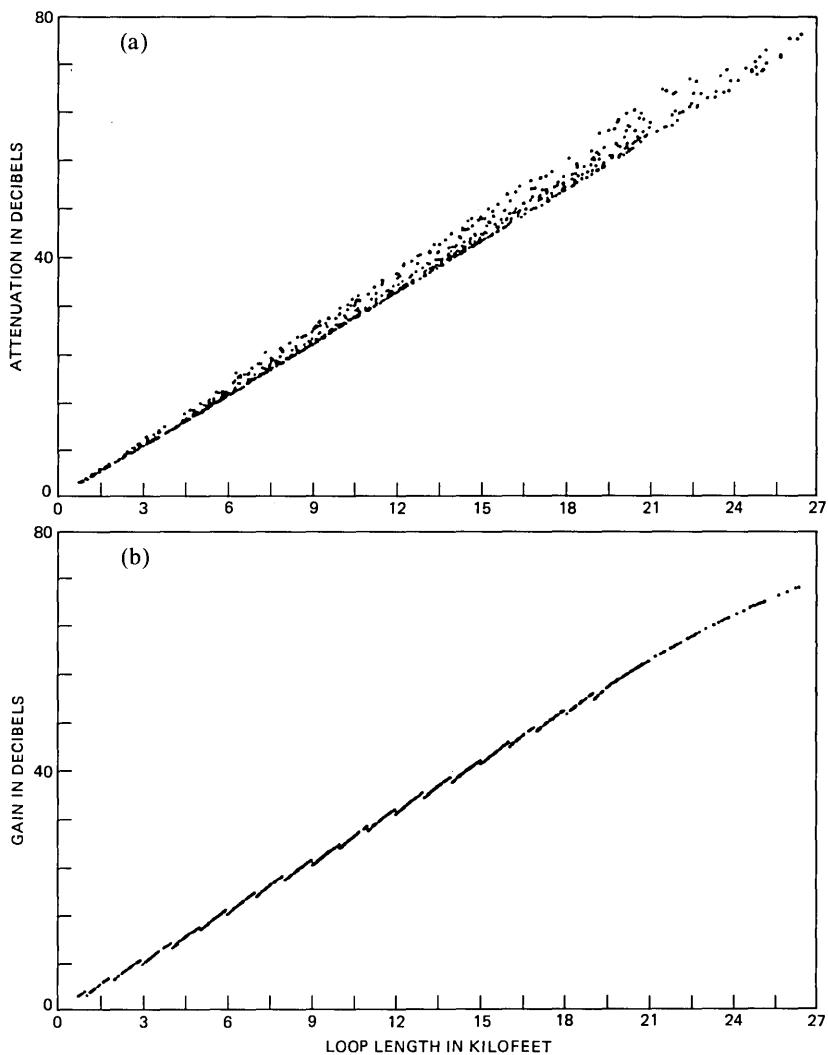


Fig. 35—Comparison of loop attenuations and equalizer gains for various loops at 324 kHz. The Y-axis scale is 8 dB/division. (a) Loop attenuation. (b) Equalizer gain.

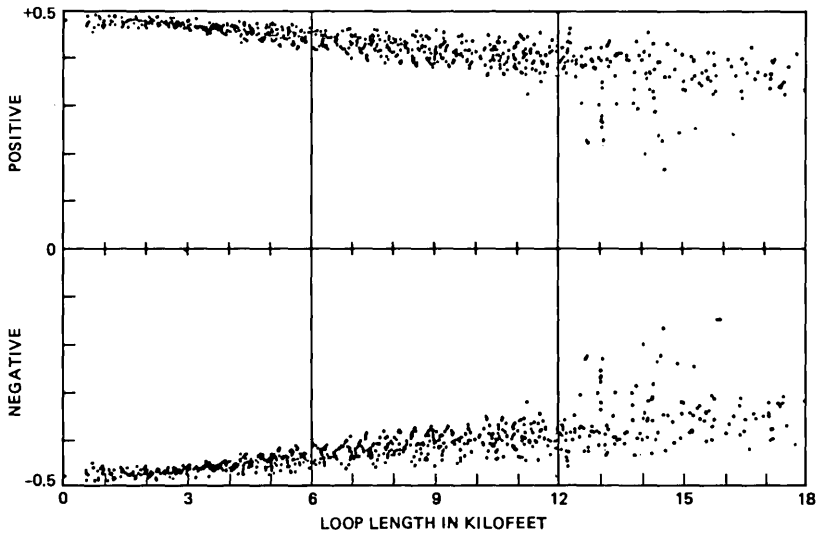


Fig. 36—Eye opening scatter plot at 324 kb/s with 20,000-ft, four-section equalizer in the TCM mode of transmission. Subscriber side data are given.

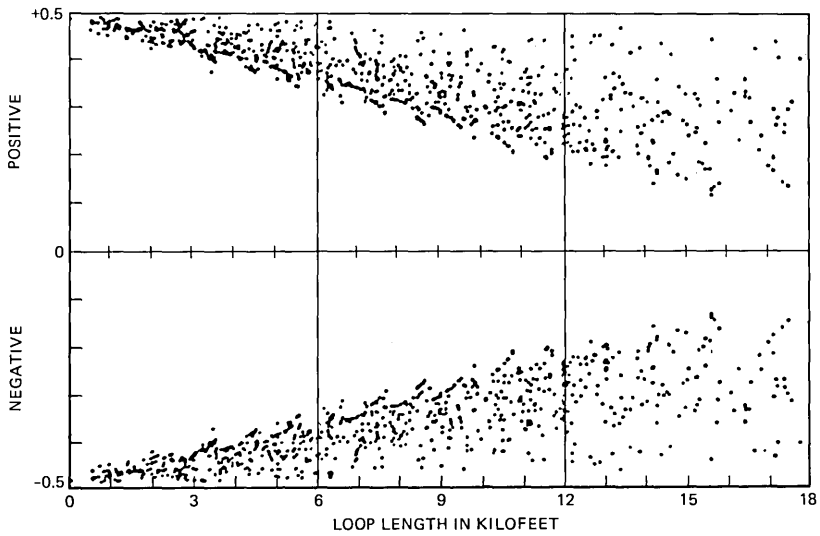


Fig. 37—Eye opening scatter plot at 126 kb/s with 20,000-ft, four-section equalizer in the TCM mode of transmission. Subscriber side data are given.

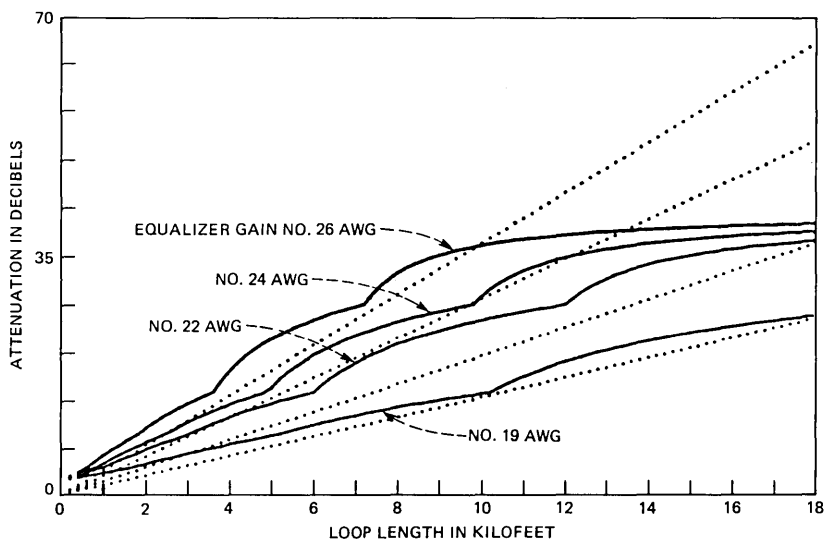


Fig. 38—Cable losses (dotted lines) and equalizer gains of a limited range, single-pole equalizer plotted for a 324-kb/s TCM design. Loop length (1 kft/division) is plotted on the X-axis and loop loss (7 dB/division) is plotted on the Y-axis.

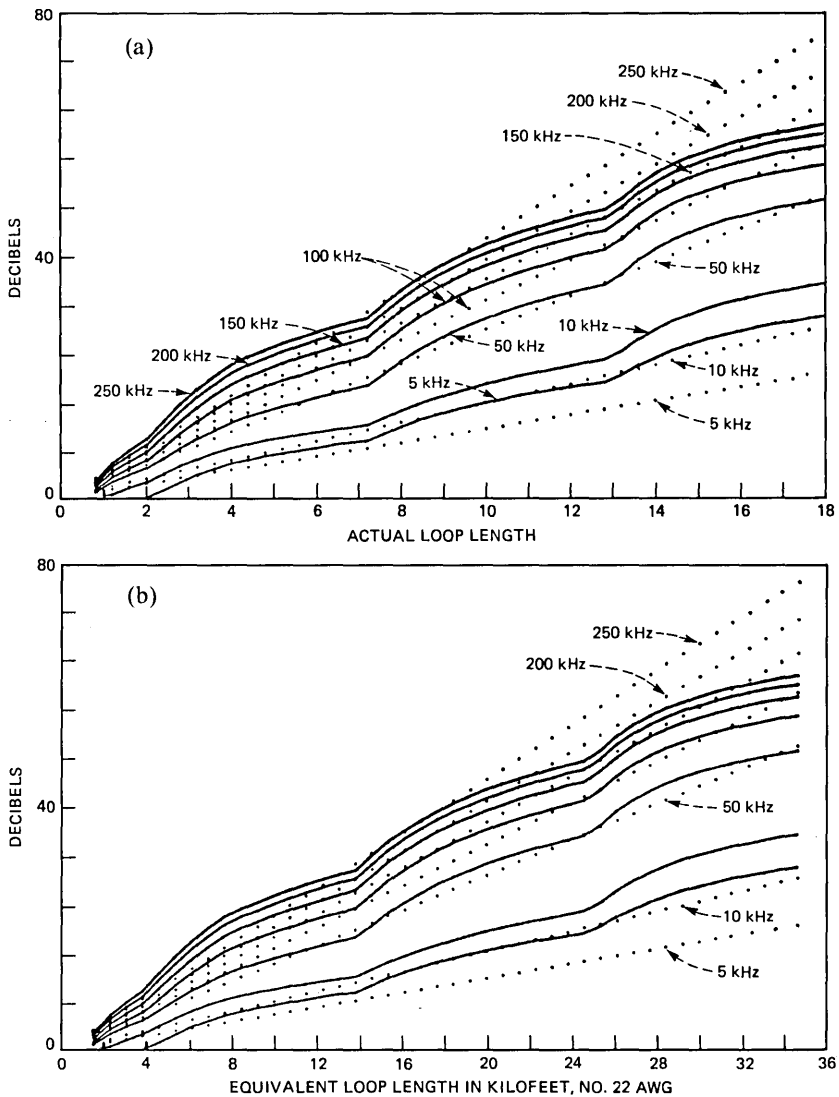


Fig. 39—Comparison of cable loss (dashed lines) and equalizer gains of the enhanced range, wider frequency, optimized equalizer at different frequencies for the No. 26 AWG cable. The Y-axis is 8 dB/division. (a) Plot against the actual loop length (the X-axis scale is 1 kft/division). (b) Plot against the equivalent loop length in terms of No. 22 AWG cable (the X-axis scale is 2 kft/division).

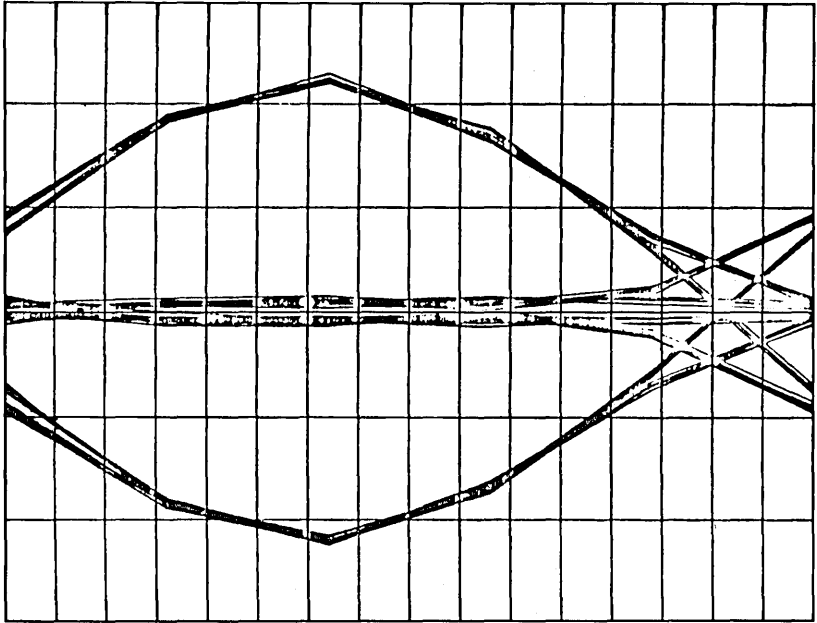


Fig. 40—Eye diagram showing the effect of finite-pulse width with 55 ft of No. 24 AWG cable at 324 kb/s.

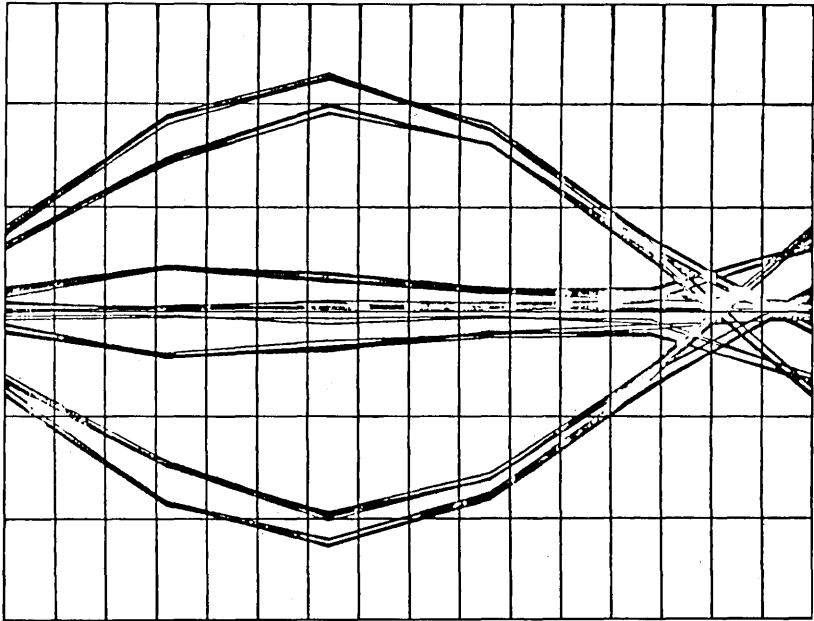


Fig. 41—Seven-section loop (88 ft, No. 19 AWG; 3571 ft, No. 22 AWG; 17 ft, No. 26 AWG; 310 ft, No. 22 AWG; 19 ft, No. 24 AWG, 1299 ft, No. 26 AWG; and 789 ft, No. 24 AWG) response at 324-kb/s TCM excitation.

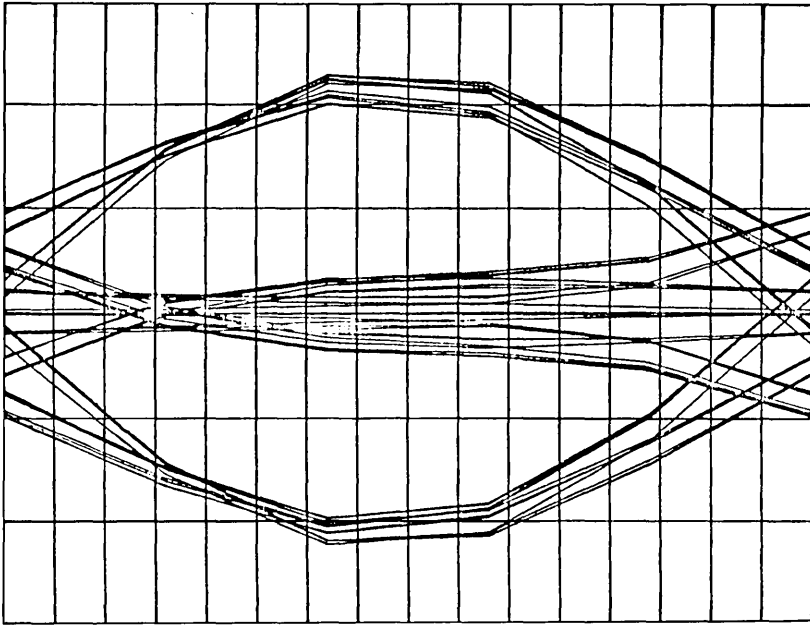


Fig. 42—Seven-section (3450 ft, No. 26 AWG; 261 ft, No. 24 AWG; 50 ft, No. 26 AWG; 313 ft, No. 22 AWG; 2477 ft, No. 24 AWG; 5329 ft, No. 22 AWG; and 200 ft, No. 24 AWG) loop response at 324-kb/s TCM excitation.

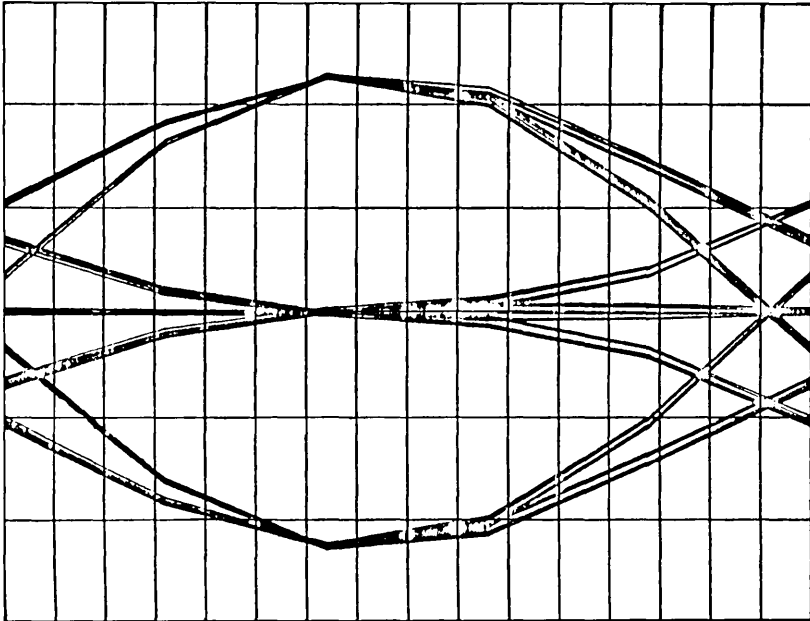


Fig. 43—Eye diagram for a single-section loop consisting of 11,998 ft of No. 26 AWG cable at 324 kb/s.

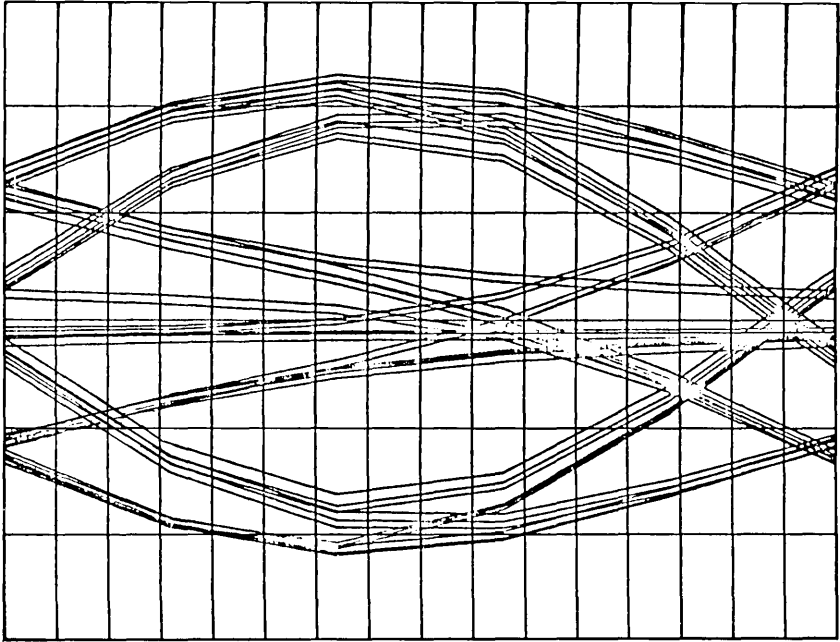


Fig. 44—Worst eye opening for an eight-section (7789 ft, No. 26 AWG; 2998 ft, No. 24 AWG; 2564 ft, No. 26 AWG; 25 ft, No. 24 AWG; 957 ft, No. 26 AWG; 2120 ft, No. 24 AWG; 141 ft, No. 26 AWG; and 720 ft, No. 24 AWG), 17,314 ft loop at 324 kb/s.

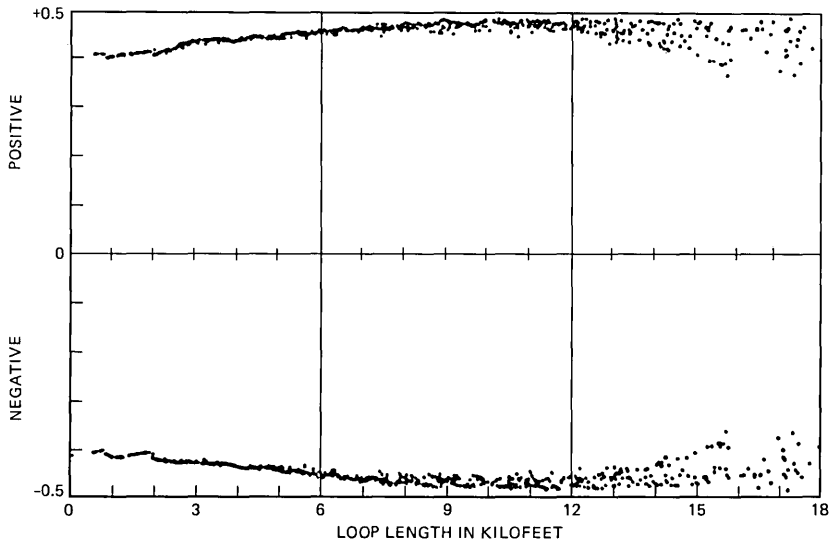


Fig. 45—Eye opening scatter plot for the 1973 survey loops at 126 kb/s TCM mode. (Effective rate is 56 kb/s.)

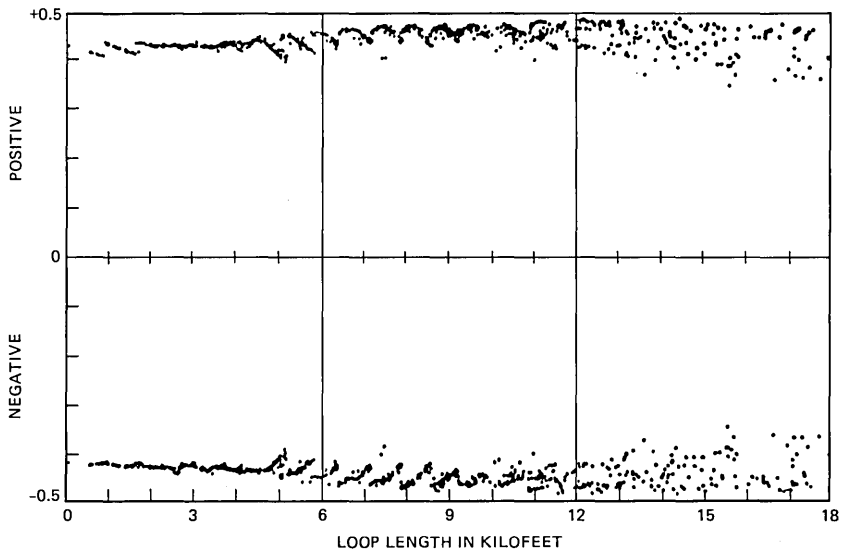


Fig. 46—Eye opening scatter plot for the 1973 survey loops at 162 kb/s TCM mode. (Effective rate is 72 kb/s.)

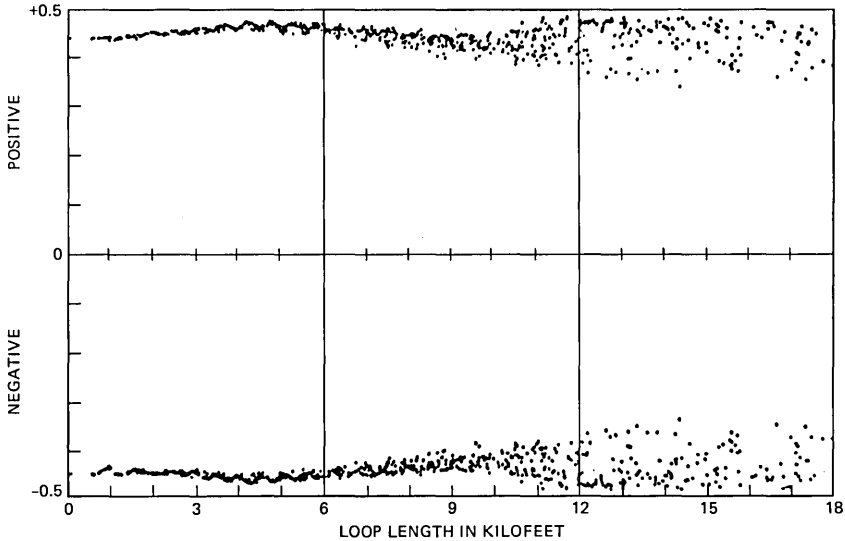


Fig. 47—Eye opening scatter plot for the 1973 survey loops at 216 kb/s TCM mode. (Effective rate is 96 kb/s.)

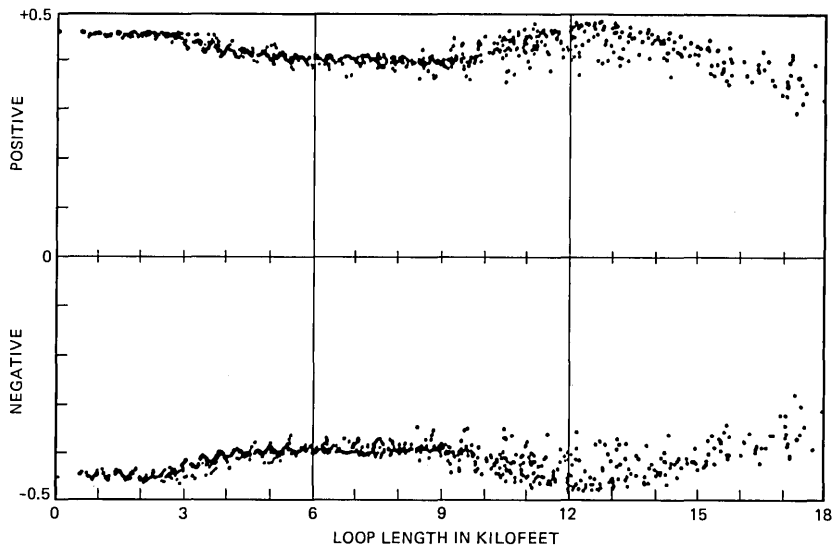


Fig. 48—Eye opening scatter plot for the 1973 survey loops at 324 kb/s. (Effective rate is 144 kb/s.)

VII. CONCLUDING REMARKS

The limit-cycle approach used in the paper and discussed in the Appendixes provides a broad spectrum of results important for the overall design of the digital transmission system. The statistical analysis of the loop plant provides a basis for the design of terminal circuitry, especially for the value of the terminating impedances for a range of transmission rates, and it also indicates the extent of mismatch. For the hybrid system design, this mismatch is the initial basis to choose the quality and extent of echo cancellation. The time-domain response in Section IV is the final basis to study the system performance. The better systems yield a satisfactory eye opening even with the worst configuration of loop studied in Section III. Next, the time-domain simulations over the entire statistically significant population of the loops (Section III) has been cross-compared for the two competing systems (the hybrid and the TCM) at various transmission rates. The summary of these results under two conditions (with bridged taps and without bridged taps) are presented in Section 5.7. Finally, the influence of the equalizer design is clearly indicated in Section VI. It is here that we propose the approach for a systematic design of the equalizer for data transmission. The computer-aided design technique is outlined and the influence of the design strategy is clearly delineated. These designs can be modified and matched with the typical loop environment for the other national telephone networks. Within the

Bell System, the designs have been tailored to the loop environment at data rates between 56 to 324 kb/s.

System design rules vary drastically with the loop environment. Hybrid systems are ideally suited where loop discontinuities are absent. In this case, a low-quality echo canceler can be complimented by an excellent matching circuit. The time-compression mode is suitable for a widely varying loop environment, especially if the extent of the echo cancellation is limited to 30 to 35 dB. Further in the TCM, the extent and persistence of echos at the end of a burst also influences the guard-time duration. Such simulations (even though not reported here) have been conducted¹⁸ and some loops (not essentially those with high-loop losses) have longer time constants for these echos. Acceptable loop configurations in the presence of bridged taps are also critically influenced by the design of the equalizer and filters. For example, the nature of balance that the designer imposes between high-frequency and low-frequency gains (depending on the distribution of the poles and zeros in the equalizer and filters) has a wide ranging influence on the allowable bridged tap(s). Hence, to permit a wide variety of loop acceptance, it is desirable to adjust the equalizer such that the fixed design of the equalizer totally undoes the effect of an average loop with an average configuration of bridged taps. Deviations (because of loop variations) from this perfect compensation causes an error which distributes the eye closure around about a near open eye diagram. It is here that the designer can obtain an acceptable eye opening (about 60 percent) even with the worst loops in the data base by choosing the optimal circuit components. Such designs have also been successfully obtained yielding very low loop failure rates in the TCM mode of transmission.

Further, it is also possible to computationally superpose two independent limit-cycle conditions (one for impulse noise and one for data transmission) to study the effects¹⁸ of impulse noise events on data transmission. The simulations graphically show the influence on the wave shape of the received data and the eye diagram it generates. To study the effects of a typical event on a cross section of the loops in the loop survey data base, we have generated scatter plots of s/n 's because of the imperfection of the transmission system with and without the events. High-loss loops suffer more. The nature and harmonic content of the event both influence the error rate. Typically recorded events do not display drastic influence on loops at 64 kb/s (in the TCM mode of transmission) until they reach about a 30-dB loss at 72 kHz. The influence starts to become significant with loops of 40-dB loss—the s/n reduces from 7 to about 3 dB and loops over 40 dB tend to become very unpredictable.

APPENDIX A

Formulations and Component Representation

A.1 Excitation functions

A.1.1 Delta function pulse shape

The m th harmonic of a single-delta function repeating indefinitely, trapped in a limit cycle every T seconds, may be represented as

$$A(p) = a_1 + a_1 e^{-pT} + a_1 e^{-2pT} + a_1 e^{-3pT} + \dots, \quad (1)$$

where $p = 2\pi im/T$ and $a_1 = 1$ denotes a positive delta function, $a_1 = 0$ denotes the absence and $a_1 = -1$ denotes the negative-delta function. Further

$$A(p) = \frac{a_1}{1 - e^{-pT}}. \quad (2)$$

The m th harmonic of K such delta-function pulses displaced from the first pulses by $\tau, 2\tau, 3\tau, \dots, k\tau, \dots, (K-1)\tau$ seconds can be generalized as

$$B(p) = \sum_{k=1}^{K} \frac{a_k e^{-(k-1)p\tau}}{(1 - e^{-pT})}. \quad (3)$$

A.1.2 Finite pulse-width square-wave pulse shape

When a single pulse of width δ repeats infinitely, trapped in a limit cycle repeating every T seconds, then it may be represented as a summation of one positive unit function (repeating infinitely every T seconds) and one negative unit function (also repeating infinitely every T seconds) but displaced by δ seconds. Hence, the algebraic representation of this pulse becomes

$$\begin{aligned} A(p) &= \frac{a_1}{p} [(1 + e^{-pT} + e^{-2pT} + e^{-3pT} \dots) \\ &\quad - e^{-p\delta}(1 + e^{-pT} + e^{-2pT} + e^{-3pT} \dots)] \\ &= \frac{a_1(1 - e^{-p\delta})}{p(1 - e^{-pT})}, \end{aligned} \quad (4)$$

where $p = 2\pi im/T$ and a_1 (as in Appendix A, section A.1.1) denotes presence or absence of the pulse. For alternate bipolar pulses, the value of a becomes $+1, 0$ or -1 , and for multilevel pulse simulations, a can become $q, (q-1) \dots 1, 0, -1, \dots (q-1), -q$, and this would generate a $(2q+1)$ level eye diagram.

The effect of K such pulses $a_1 \dots a_k$ displaced from the first pulse

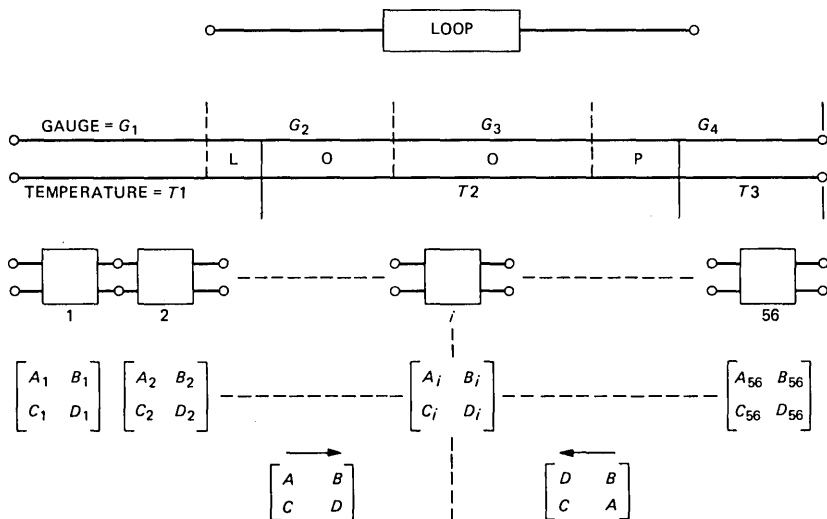


Fig. 49—Loop without bridged taps.

by $\tau, 2\tau, \dots, k\tau, \dots, (K-1)\tau$ can be written as

$$B(p) = \sum_{k=1}^{k=K} \frac{\alpha_k (1 - e^{-p\delta}) e^{-(k-1)p\tau}}{p(1 - e^{-pT})} \quad (5)$$

APPENDIX B

Loop Calculations

B.1 Loops without bridged taps

In Fig. 49, a loop with four gauges and three temperatures is shown. Fifty-six individual sections are created, each having its own gauge and its own temperature. For these sections, the individual $ABCD$ parameters are generated. Composite loop parameters are obtained by matrix multiplication* at each harmonic frequency of the excitation function [See eqs. (3) and (5).]

B.2 Loops with bridged taps

In Fig. 50, a loop with a sections and b bridged taps is shown. Each bridged tap has c sections. This would be the most general representation of any loop without load coils. Only one single temperature is permitted for the entire loop and its bridged taps, to keep the com-

* Each term is complex and should be treated as such.

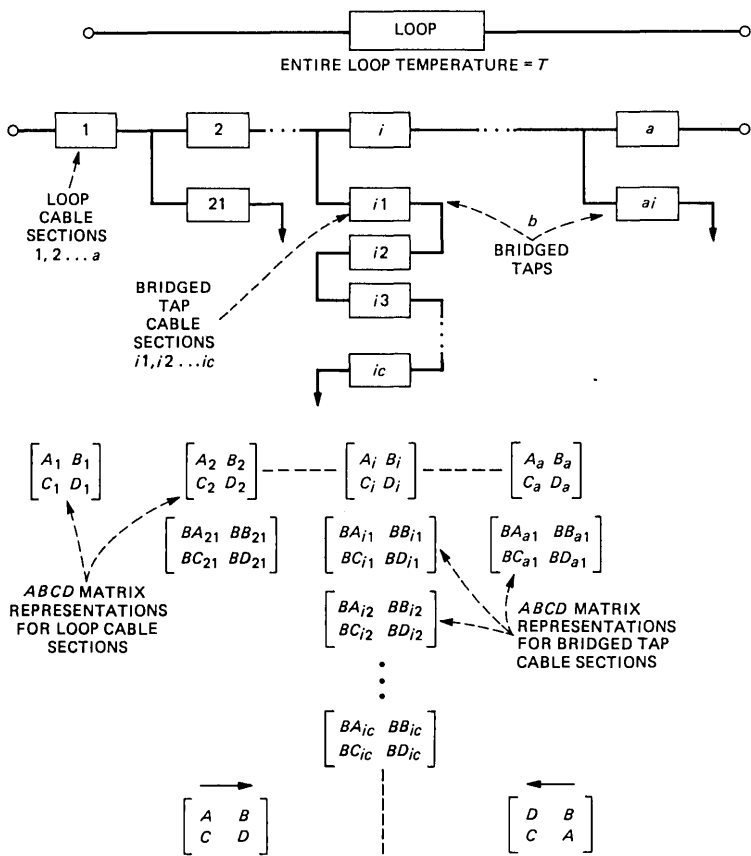


Fig. 50—Loop with bridged taps.

plexity of the representation and to conserve the core space requirements for the computer. Individual *ABCD* parameters for the individual loop section is first generated and stored. When a bridged tap is encountered, its own *ABCD* parameters are obtained by normal *ABCD* matrix multiplication for all the sections in that particular bridged tap. The loop at this point sees the bridged tap as a parallel connection, and the bridged tap *ABCD* is obtained by making *A* and *D* unity, *B* zero, and *C* as $(Y_0 \tanh \Gamma)$, where Y_0 is the admittance (i.e., the square root of *CD* divided by *AB*) prior to conversion, and Γ is propagation constant for the entire bridged tap (i.e., the complex log of half the sum of *A*, *D*, B/Z_0 , and Z_0C , where $Z_0 = 1/Y_0$) prior to conversion.

Thus, the matrix reduction is continued in the presence of the bridged taps, and the net *ABCD* parameters for the entire loop are obtained.

APPENDIX C

Conversion to Time Domain

The system's spectral-domain response can be written as

$$F(p) = B(p) \times \zeta(p), \quad (6)$$

where $\zeta(p)$ represents the system's transfer function for the m th harmonic and p is defined $2\pi im/T$. The inverse Fourier transform of $F(p)$ is

$$\begin{aligned} f(t) &= \frac{1}{2\pi i} \int_{-i\infty}^{+i\infty} B(p) e^{pt} \zeta(p) dp \\ &= \frac{1}{2\pi i} \int_{-i\infty}^{+i\infty} \sum_{k=1}^{k=K} \frac{a_k e^{-(k-1)p\tau} \zeta(p) e^{pt}}{1 - e^{-pT}} dp \\ &= \sum_{k=1}^{k=K} \left[\text{sum of residues at } p = \frac{\pm 2\pi im}{T} \right]. \end{aligned} \quad (7)$$

For delta functions, we have $B(p)$ defined by eq. (3), and each residue at the m th harmonic can now be evaluated as

$$[a_{-1}]_{m=m} = \lim_{p \rightarrow \frac{2\pi im}{T}} \left(p - \frac{2\pi im}{T} \right) \sum_{k=1}^{k=K} \frac{a_k e^{-(k-1)p\tau} \zeta(p) e^{pt}}{1 - e^{-pT}}. \quad (8)$$

By differentiating the numerator and denominator separately and by L'Hôpital's rule, we have

$$[a_{-1}]_{m=m} = \sum_{k=1}^{k=K} \frac{a_k e^{-(k-1)p\tau} \zeta(p) e^{pt}}{T}, \quad (9)$$

since $e^{-pT} \rightarrow 1$ as $p \rightarrow 2\pi im/T$. The summation of residues leads to the time-domain response

$$f(t) = \sum_{m=-M}^{m=+M} \sum_{k=1}^{k=K} \frac{a_k e^{-\frac{(k-1)2\pi im}{K} t} \zeta\left(\frac{2\pi im}{T}\right) e^{\frac{2\pi imt}{T}}}{T}. \quad (10)$$

In the earlier computations, M is limited to 64, K is 48. In the more recent computations, M and K have ranged between 64-1200, and 48-480, respectively.

REFERENCES

1. K. Tazaki, K. Okimi, and Y. Hidaka, "COSMOS-1 System—Multiplanning and Local Transmission," Paper presented at Nat. Telecommun. Conf., 1978.
2. N. Inoue, R. Komiya, and Y. Inoue, "Time Shared Two-Wire Digital Transmission for Subscriber Loops," ICC 1979 Conf. Record Paper 2.4, pp. 2.4.1-5.
3. W. Neu, "Long Range Prospects of Digital Subscriber Lines and Sets," Proc. 1978

- Int. Zurich Seminar on Digital Commun., IEEE Catalog No. 78 CH-1325-0 ASST, pp. C1.1-5.
4. T. Svenssen, "Methods for Two-Wire Duplex Digital Transmission at 80 kBit/s on Subscriber Lines," Proc. 1978 Int. Zurich Seminar on Digital Commun., IEEE Catalog No. 78 CH-1325-0 ASST, pp. C5.1-4.
 5. P. T. Nielson and M. W. Gram, "A Digital Hybrid for Two-Wire Digital Subscriber Loops," Nat. Telecommun. Conf. 1978, IEEE Catalog 1354-0/78/0000-0098, pp. 21.2.1-7.
 6. A. H. Ithell and W. G. T. Jones, "A Proposal for the Introduction of Digital Techniques into Local Distribution," Proc. 1978 Int. Zurich Seminar on Digital Commun., IEEE Catalog No. 78 CH-1325-0 ASST, pp. F5.1-5.
 7. British Post Office, "Consideration of a Customer's Digital Signaling System," CCITT Study Group XI Delayed Contribution, January 1979.
 8. W. A. Kaiser, "Strategies for the Introduction of New Services in Existing Local Networks," Proc. 1978 Int. Zurich Seminar on Digital Commun., IEEE Catalog No. 78 CH-1325-0 ASST, pp. F1.1-10.
 9. G. Robin and S. R. Treves, "Progressive Introduction of Digital Switching and Transmission," Proc. 1978 Int. Zurich Seminar on Digital Commun., IEEE Catalog No. 78 CH-1325-0 ASST, pp. F4.1-6.
 10. R. K. Even, R. A. McDonald, and H. Seidel, "Digital Transmission Capability of the Loop Plant, ICC 1979 Conf. Record, Paper 2.1, pp. 2.1.1-7.
 11. W. E. Danielson and W. B. Macurdy, "Local Digital Switching Trends and Design Objectives in the Bell System Network," Conf. Record Int. Switching Symp., May 1979.
 12. S. V. Ahamed et al., "The Provision of High Speed Digital Data Services Over Existing Loop Plant," Proc. Nat. Elect. Conf. (November 1979), 33, pp. 265-70.
 13. L. M. Manhire, "Physical and Transmission Characteristics of Customer Loop Plant," B.S.T.J. 57, No. 1 (January 1978), pp. 35-59.
 14. S. V. Ahamed, "The Nature and Use of Limit Cycles in Determining the Behavior of Certain Semideterminate Systems," B.S.T.J. 58, No. 8 (October 1979), pp. 1869-84.
 15. Private communication.
 16. E. R. Kretzmer, "Generalization of a Technique for Binary Data Communication," IEEE, Trans. Commun. Tech., 1 CM-14, No. 1 (February 1966), pp. 67-8.
 17. D. J. Clothier and P. Bylanski, "Digital Transmission System for Multiterminal Applications," GEC Telecommun. J., 41 (1980), pp. 10-5.
 18. S. V. Ahamed, P. P. Bohn, and N. L. Gottfried, "A Tutorial on Two-Wire Digital Transmission in the Loop Plant," IEEE Special Issue on Communications, COM 29, No. 11 (November 1981), pp. 1554-64.

CONTRIBUTORS TO THIS ISSUE

Syed V. Ahamed, B.E., 1957, University of Mysore; M.E., 1958, Indian Institute of Science; Ph.D., 1962, University of Manchester, U.K.; Post-Doctoral Research Fellow, 1963, University of Delaware; Assistant Professor, 1964, University of Colorado; M.B.A. (Economics), 1978, New York University; Bell Laboratories, 1966–1981. At Bell Laboratories, Mr. Ahamed has worked in computer-aided engineering analysis and design of electromagnetic components, designed and implemented minicomputer software and hardware interfacing, applied algebraic analysis to the design of domain circuits, and investigated computer aids to the design of bubble circuits. He has investigated new varacter designs for microwave power in the C-band and developed hardware and software interfacing for audio frequency CODECS. Beginning in 1975, he optimized CODEC designs, encoding techniques, and speech-encoded data storage and manipulation by minicomputers. Since 1977, he has been simulating the overall performance of the loop plant, while carrying bidirectional digital data in the range of 56 to 324 kilobaud. He is currently a visiting professor in the Electrical Engineering Department at the University of Hawaii at Monoa, Hawaii, and he is on a leave of absence from Bell Laboratories.

Arthur F. Bergh, currently enrolled at Swarthmore College; Bell Laboratories, 1980—. Mr. Bergh has been engaged in speech recognition research in the Acoustics Research Department.

Ernest E. Bergmann, A.B. (Physics), 1964, Columbia University; M.A. (Physics), 1966, Ph.D. (Physics), 1969, Princeton University; Lehigh University, 1969—. Mr. Bergmann is a Professor of Physics at Lehigh University; from 1977 to 1978, he was on sabbatical at Los Alamos Scientific Laboratory. He is presently a consultant to Bell Laboratories, Allentown. His current research activity is in optics and laser physics; he is also active in software design. Member, AAUP, APS, OSA, Sigma Xi.

Edward G. Bowen, A.S. (Electrical Engineering), 1963, Vermont Technical College; B.S. (Electrical Engineering), 1971, Newark College of Engineering; Bell Laboratories, 1963—. At Bell Laboratories, Mr. Bowen is an Associate Member of the Technical Staff. His principal interests are coding of video signals.

Clyde L. Monma, B.S. (Computer Science), 1974, Washington State University, M.S. and Ph.D. (Operations Research), 1978, Cornell University; Bell Laboratories, 1979—. Mr. Monma has worked on developing Operations Research methods via research in the areas of sequencing and scheduling problems, network optimization methods, production and inventory control, and algorithmic design. As a consultant, he has worked on projects involving scheduling and network planning. He is currently working on network design tools for data transport networks. He is also the Book Review Editor for *Networks* and a member of ORSA.

Arun N. Netravali, B. Tech. (Honors), 1967, Indian Institute of Technology; M.S., 1969, Ph.D., 1970, (Electrical Engineering), Rice University; Bell Laboratories, 1972—. From 1970 to 1972, Mr. Netravali worked on problems related to filtering, guidance, and control for the space shuttle. Early in his career at Bell Laboratories, he began working on various aspects of signal processing. Presently, he is Head, Visual Communication Research Department. He was a visiting professor in the Electrical Engineering Department at Rutgers University, New Brunswick, New Jersey. He serves on the editorial board of the Proceedings of the IEEE, and is the editor of Signal Processing and Communication Electronics for the IEEE Transactions on Communications. Member, Tau Beta Pi, Sigma Xi. Senior Member, IEEE.

Lawrence R. Rabiner, S.B. and S.M., 1964, Ph.D. (Electrical Engineering), The Massachusetts Institute of Technology; Bell Laboratories, 1962—. From 1962 through 1964, Mr. Rabiner participated in the cooperative plan in electrical engineering at Bell Laboratories. He worked on digital circuitry, military communications problems, and problems in binaural hearing. Presently, he is engaged in research on speech communications and digital signal processing techniques. He is coauthor of *Theory and Application of Digital Signal Processing* (Prentice-Hall, 1975) and *Digital Processing of Speech Signals* (Prentice-Hall, 1978). Former President, IEEE, ASSP Society; former Associate Editor, ASSP Transactions; former member, Technical Committee on Speech Communication of the Acoustical Society, ASSP Technical Committee on Speech Communication; Member, IEEE Proceedings Editorial Board, Eta Kappa Nu, Sigma Xi, Tau Beta Pi. Fellow, Acoustical Society of America, IEEE.

Moshe Segal, B.Sc. and Ingénieur (Mechanical Engineering), 1956, Technion-Israel Institute of Technology, Dr. of Engineering (Opera-

tions Research), 1961, The Johns Hopkins University; Bell Laboratories, 1961—. Mr. Segal has worked on the development and application of Operations Research methods including queueing models, traffic engineering methods, network flow techniques, and scheduling algorithms. He is currently supervisor of the Operations Research and Network Methods Group. During the academic year 1976–1977, he was a Visiting Scientist and a Lady Davis Fellow at the Technion-Israel Institute of Technology. Mr. Segal is an Adjunct Professor at Columbia University, he serves on the editorial board of *Discrete Applied Mathematics*, and he is an Associate Editor of *Operations Research Letters*.

Jay G. Wilpon, B.S. (Mathematics), A.B. (Economics), Lafayette College; Bell Laboratories 1977—. Since joining Bell Laboratories, he has been with the Acoustics Research Department. He has been engaged in speech communications research and is presently concentrating on problems of speech recognition.

PAPERS BY BELL LABORATORIES AUTHORS

COMPUTING/MATHEMATICS

- Brillhart J., Filaseta M., Odlyzko A., **On an Irreducibility Theorem of A. Cohn.** *Can J Math* 33(5):1055-1059, 1981.
- Chung F. R. K., Garey M. R., Johnson D. S., **On Packing 2-Dimensional Bins.** *SIAM J Alg* 3(1):66-76, 1982.
- Dixon P., **Plans and Written Directions for Complex Tasks.** *J Verb Lear* 21(1):70-84, 1982.
- Fishburn P. C., Brams S. J., **Efficacy, Power, and Equity Under Approval Voting.** *Publ Choice* 37(3):425-434, 1981.
- Fullerton L. W., Hills J. G., **Computer Simulations of Close Encounters Between Binary and Single Stars—The Effect of the Impact Velocity and the Stellar Masses.** *Astronom J* 87(1):175-183, 1982.
- Futia C. A., **Invariant Distributions and the Limiting Behavior of Markovian Economic Models.** *Econometric* 50(2):377-408, 1982.
- Gansner E. R., **The Enumeration of Plane Partitions Via the Burge Correspondence.** *Ill J Math* 25(4):533-554, 1981.
- Graedel T. E., McGill R., **Graphical Presentation of Results From Scientific Computer Models.** *Science* 215(4537):1191-1198, 1982.
- Kernighan B. W., **PIC—A Language for Typesetting Graphics.** *Software* 12(1):1-21, 1982.
- Kernighan B. W., Morgan S. P., **The UNIX Operating System—A Model for Software-Design.** *Science* 215(4534):779-783, 1982.
- Kurshan R. P., Odlyzko A. M., **Values of Cyclotomic Polynomials at Roots of Unity.** *Math Scand* 49(1):15-35, 1981.
- Lengauer T., **Upper and Lower Bounds on the Complexity of the Min-Cut Linear Arrangement Problem on Trees.** *SIAM J Alg* 3(1):99-113, 1982.
- MacDonald N. H., Frase L. T., Gingrich P. S., Keenan S. A., **The Writers Workbench—Computer Aids for Text Analysis.** *IEEE Commun* 30(1):105-110, 1982.
- Mirman L. J., Ranaan J., Tauman Y., **A Sufficient Condition on f for f^μ to be in $pNAD$.** *J Math Econ* 9(3):251-257, 1982.
- McIlroy M. D., **Development of a Spelling List.** *IEEE Commun* 30(1):91-99, 1982.
- Rothkopf E. Z. et al., **Effects of Spatial Context During Acquisition on the Recall of Attributive Information.** *J Exp Psy H* 8(2):126-138, 1982.
- Serfozo R., **Functional Limit Theorems for Extreme Values of Arrays of Independent Random Variables.** *Ann Probab* 10(1):172-177, 1982.
- Sharma D. K., Gruchacz A. M., **The Display Text Editor TED—A Case Study in the Design and Implementation of Display-Oriented Interactive Human Interfaces.** *IEEE Commun* 30(1):111-119, 1982.
- Takane Y., Carroll J. D., **Nonmetric Maximum-Likelihood Multidimensional Scaling From Directional Rankings of Similarities.** *Psychometri* 46(4):389-405, 1981.
- Tully J. C., **Computer-Stimulation of the Dynamics of Chemical Processes.** *Comput Chem* 5(4):159-165, 1981.
- Whitted T., **Some Recent Advances Computer-Graphics.** *Science* 215(4534):767-774, 1982.
- Whitten W. B., Leonard J. M., **Directed Search Through Autobiographical Memory.** *Mem Cognit* 9(6):566-579, 1981.

ENGINEERING

- Acampora A. S., **Bit Error Rate Bounds for Viterbi Decoding With Modem Implementation Errors.** *IEEE Commun* 30(1):129-134, 1982.
- Agrawal V. D., Seth S. C., Agrawal P., **Fault Coverage Requirement in Production Testing of LSI Circuits.** *IEEE J Soli* 17(1):57-60, 1982.

- Antler M. et al., **Fretting Corrosion of Gold-Plated Connector Contacts**. *Wear* 74(1):27-50, 1981.
- Arnold H. W., Cox D. C., Hoffman H. H., **Antenna Beamwidth Independence of Measured Rain Attenuation on a 28-GHz Earth-Space Path**. *IEEE Antenn* 30(2):165-167, 1982.
- Arthurs E., Stuck B. W., **Bounding Mean Throughput Rate and Mean Delay in Office Systems**. *IEEE Commun* 30(1):12-18, 1982.
- Bean J. C., Sadowski E. A., **Silicon MBE Apparatus for Uniform High-Rate Deposition on Standard Format Wafers**. *J Vac Sci T* 20(2):137-142, 1982.
- Birrer I. J. et al., **Sigma Degrees Signature of the Amazon Rain Forest Obtained From the Seasat Scatterometer**. *IEEE Geosci* 20(1):11-17, 1982.
- Blasie J. K. et al., **The Location of Redox Centers in Biological Membranes Determined by Resonance X-ray Diffraction. 2. Analysis of the Resonance Diffraction Data**. *Bioc Biop A* 679(2):188-197, 1982.
- Bodtmann W. F., Arnold H. W., **Fade-Duration Statistics of a Rayleigh-Distributed Wave**. *IEEE Commun* 30(3):549-553, 1982.
- Bonyhard P. I., Nelson T. J., **Ion-Implanted Bubble Memory Device Chip Organization**. *IEEE Magnet* 18(2):740-744, 1982.
- Bonyhard P. I., Hagedorn F. B., Ekholm D. T., Muehlner D. J., Nelson T. J., Roman B. J., **Large Capacity Ion-Implanted Bubble Devices**. *IEEE Magnet* 18(2):737-740, 1982.
- Brainard R. C., Netravali A. N., Pearson D. E., **Predictive Coding of Composite NTSC Color Television Signals**. *SMPTE J* 91(3):245-252, 1982.
- Brown W. L. et al., **Ion-Beam Lithography**. *Nucl Instru* 191(1-3):157-168, 1981.
- Browning J. D., Tanimoto S. L., **Segmentation of Pictures Into Regions With a Tile-by-Tile Method**. *Patt Recog* 15(1):1-10, 1982.
- Buschvishniac I. J., **Drive Point Impedance of an Infinite Orthotropic Plate Under Tension**. *J Acoust So* 71(2):368-371, 1982.
- Campbell J. C., Ogawa K., **Heterojunction Phototransistors for Long-Wavelength Optical Receivers**. *J Appl Phys* 53(2):1203-1208, 1982.
- Cohen L. G., Mammel W. L., Lumish S., **Dispersion and Bandwidth Spectra in Single-Mode Fibers**. *IEEE J Q El* 18(1):49-53, 1982.
- Cox D. C., **Cochannel Interference Considerations in Frequency Reuse Small-Coverage-Area Radio Systems**. *IEEE Commun* 30(1):135-142, 1982.
- Dutta N. K., Nelson R. J., **Gain Measurements in 1.3-Micron InGaAsP-InP Double Heterostructure Lasers**. *IEEE J Q El* 18(1):44-49, 1982.
- Fichtner W., Levin R. M., Taylor G. W., **Experimental Results on Submicron—Size P Channel MOSFETS**. *Elec Dev L* 3(2):34-37, 1982.
- Flanagan J. L., Johnston J. D., Upton J. W., **Digital Voice Storage in a Microprocessor**. *IEEE Commun* 30(2):336-345, 1982.
- Fratamico J. J., Gans M. J., Owens G. J., **A Wide Scan Quasi-Optical Frequency Diplexer**. *IEEE Micr T* 30(1):20-27, 1982.
- Frye R. C., Leamy H. J., **Direct Observation of the Gate Oxide Electric-Field Distribution in Silicon MOSFETS**. *Elec Dev L* 3(1):1-3, 1982.
- Fukui H. et al., **Reliability of Power GaAs Field-Effect Transistors**. *IEEE Device* 29(3):395-401, 1982.
- Goodman D. J., Timor U., **Spread-Spectrum Mobile Radio With Variable-Bit-Rate Speech Transmission**. *IEEE Commun* 30(3):531-538, 1982.
- Harvey F. K., **Mementos of Early Photographic Sound Recording**. *SMPTE J* 91(3):237-244, 1982.
- Henry C. H., **Theory of the Linewidth of Semiconductor Lasers**. *IEEE J Q El* 18(2):259-264, 1982.
- Iga K., Miller B. I., **Chemically Etched Mirror GaInAsP/InP Lasers—Review**. *IEEE J Q El* 18(1):22-29, 1982.
- Kaufman J. S., **Congestion Formulas for a Heterogeneous Server Loss System With Random Selection Discipline**. *Operat Res* 29(6):1167-1180, 1981.
- Lambert A. M., Luss H., **Production Planning With Time-Dependent Capacity Bounds**. *Eur J Oper* 9(3):275-280, 1982.

- Lee T. P., **LEDS and Photodetectors for Wavelength Division-Multiplexed Light-Wave Systems.** *Opt Laser T* 14(1):15-20, 1982.
- Liebesman B. S., **Criteria for Continued Inspection During the Discontinue Phase of MIL-STD-105D.** *J Qual Tech* 14(1):34-39, 1982.
- Limb J. O., **Communications in the Automated Office.** *IEEE Commun* 30(1):1-5, 1982.
- Lin C. L., Reed W. A., Pearson A. D., Shang H. T., Glodis P. F., **Designing Single-Mode Fibers for Near-IR(1.1-1.7 μm) Frequency Generation by Phase-Matched 4-Photon Mixing in the Minimum Chromatic Dispersion Region.** *Electr Lett* 18(2):87-89, 1982.
- Mammel W. L., Cohen L. G., **Numerical Prediction of Fiber Transmission Characteristics From Arbitrary Refractive-Index Profiles.** *Appl Optics* 21(4):699-703, 1982.
- Marcuse D., Nash F. R., **Computer Model of an Injection Laser With Asymmetrical Gain Distribution.** *IEEE J Q El* 18(1):30-43, 1982.
- Menendez R. C., Lee S. W., **Analysis of Rectangular Horn Antennas Via Uniform Asymptotic Theory.** *IEEE Antenn* 30(2):241-250, 1982.
- Migus A., Shank C. V., Ippen E. P., Fork R. L., **Amplification of Subpicosecond Optical Pulses—Theory and Experiment.** *IEEE J Q El* 18(1):101-109, 1982.
- Mueller K. H., Werner J. J., **A Hardware Efficient Passband Equalizer Structure for Data Transmission.** *IEEE Commun* 30(3):538-541, 1982.
- Nutt G. J., Bayer D. L., **Performance of CSMA CD Networks Under Combined Voice and Data Loads.** *IEEE Commun* 30(1):6-11, 1982.
- Paek U. C. et al., **Parametric Effects on the Bandwidth of a Single-Mode Fiber With Experimental Verification.** *Appl Optics* 21(4):704-709, 1982.
- Prabhu K. A., Bose N. K., **Impulse-Response Arrays of Discrete-Space Systems Over a Finite Field.** *IEEE Acoust* 30(1):10-18, 1982.
- Rummler W. D., **A Simplified Method for the Laboratory Determination of Multipath Outage of Digital Radios in the Presence of Thermal Noise.** *IEEE Commun* 30(3):487-494, 1982.
- Shashaty A. J., **Twist Moments and Deformations in Submarine Cable Installation.** *J Eng Ind* 104(1):104-107, 1982.
- Stamatoff F. et al., **The Location of Redox Centers in Biological Membranes Determined by Resonance X-Ray Diffraction. 1. Observation of the Resonance Effect.** *Bioc Biop A* 679(2):177-187, 1982
- Stone J., Earl H. E., Derosier R. M., **Measurement Set for Optical Fiber Loss Spectra.** *Rev Sci Ins* 53(2):197-201, 1982.
- Stone J., Lemaire P. J., **Reduction of Loss Due to OH in Optical Fibers by a 2-Step OH-*OD Exchange Process.** *Electr Lett* 18(2):78-80, 1982.
- Tsang W. T. et al., **Stripe-Geometry Laser With In situ Ohmic Contact and Self-Aligned Native Surface Oxide Mask for Current Isolation Prepared by Molecular-Beam Epitaxy.** *Electr Lett* 18(3):123-124, 1982.
- Weissmann G. F., **Damping and Metals Characterization.** *J Test Eval* 10(1):21-24, 1982.
- Wright P. D., Nelson R. J., Wilson R. B., **Monolithic Integration of InGaAsP Heterostructure Lasers and Electrooptical Devices.** *IEEE J Q El* 18(2):249-258, 1982.
- Yeh Y. S., Reudink D. O., **Efficient Spectrum Utilization for Mobile Radio Systems Using Space Diversity.** *IEEE Commun* 30(3):447-455, 1982.

MANAGEMENT/ECONOMICS

- Chang J. M., Chang S. K., **Database Altering Techniques for Office Activities Management.** *IEEE Commun* 30(1):74-81, 1982.
- Cherry L., **Writing Tools.** *IEEE Commun* 30(1):100-105, 1982.
- Gehani N. H., **The Potential of Forms in Office Automation.** *IEEE Commun* 30(1):120-125, 1982.

- Hausman J. A., Taylor W. E., **A Generalized Specification Test.** *Econ Lett* 8(3):239-245, 1981.
- Jackson K. A., Gilmer G. H., Matula R. A., **Inventivity Issue Joined—Small Firm Concept Challenged.** *Ind Res Dev* 24(2):210-216, 1982.
- Tole J. R., Stephens A. T., Harris R. L., Ephrath A., **Visual Scanning Behavior and Mental Workload in Aircraft Pilots.** *Aviat Sp En* 53(1):54-61, 1982.

PHYSICAL SCIENCES

- Abrahams E., Anderson P. W., Lee P. A., Ramakrishnan T. V., **Quasiparticle Lifetime in Disordered 2-Dimensional Metals.** *Phys Rev B* 24(12):6783-6789, 1981.
- Allen S. J., Tsui D. C., Derosa F., Thornber K. K., Wilson B. A., **Direct Measurement of Velocity Overshoot by Hot-Electron, Submillimeter Wave Conductivity in Si Inversion Layers.** *J Physique* 42(NC7):369-374, 1981
- Allen S. J., Wilson B. A., Tsui D. C., Gold A., Gotze W., **Experimental Measurement of the Frequency-Dependent Memory Function for the 2D Electron Gas in Si Inversion Layers.** *Surf Sci* 113(1-3):211-217, 1982.
- Auborn J. J. et al., **Sodium-Sulfur-Aluminum Chloride Cells.** *J Energ* 6(2):86-90, 1982.
- Bair H. E., Warren P. C., **Morphology of Lightly Plasticized PVC.** *J Macr S Ph* B20(3):381-402, 1981.
- Baker W. O., **Polymers in the World of Tomorrow.** *ACS Symp S* 1981(175):165-202, 1981.
- Banavar J. R., Cieplak M., **Nature of Ordering in Spin Glasses.** *Phys Rev L* 48(12):832-835, 1982.
- Blythe P. A., Daniels P. G., Simpkins P. G., **Thermally Driven Cavity Flows in Porous Media. 1. The Vertical Boundary-Layer Structure Near the Corners.** *P Roy Soc A* 380(1778):119-136, 1982.
- Bosch M. A., Lemons R. A., **Crystallization of Amorphous Silicon on Silica by CW-Laser Irradiation.** *Appl Phys L* 40(2):166-168, 1982.
- Bozio R. et al., **Infrared Study on the Formation of Charge-Density Waves in (TMTSF)₂X (X = REO₄- and PF₆- at Atmospheric Pressure.** *Sol St Comm* 41(12):905-910, 1982.
- Brandle C. D., **Flow Transitions in Czochralski Oxide Melts.** *J Cryst Gr* 57(1):65-70, 1982.
- Brown T. R., **Is Creatine-Phosphokinase in Equilibrium in Skeletal Muscle?** *Fed Proc* 41(2):174-175, 1982.
- Cava R. J., Roth R. S., Negas T., Parker H. S., Minor D. B., **Crystal Chemistry, Modulated Structure, and Electrical Conductivity in the Oxygen Excess Scheelite-Based Compounds La_{1-x}Th_xNbO_{4+x/2} and LaNb_{1-x}W_xO_{4+x/2}.** *J Sol St Ch* 40(3):318-329, 1981.
- Chen C. Y. et al., **Characteristics of an In_{0.53}Ga_{0.47}As Very Shallow Junction Gate Structure Grown by Molecular-Beam Epitaxy.** *Elec Dev L* 3(1):15-17, 1982.
- Cheng K. Y., Cho A. Y., Drummond T. J., Morkoc H., **Electron Mobilities in Modulation Doped Ga_{0.47}In_{0.53}As/Al_{0.48}In_{0.52}As Heterojunctions Grown by Molecular-Beam Epitaxy.** *Appl Phys L* 40(2):147-149, 1982.
- Chin A. K., **Evaluation of Defects in CDTE Using a Simple Cathodoluminescence Technique.** *J Elchem So* 129(2):369-374, 1982.
- Chin A. K., Bonner W. A., **Investigation of Impurity Variations by Cathodoluminescence Imaging—Application to GaSb-TE.** *Appl Phys L* 40(3):248-251, 1982.
- Ching Y. et al., **Resonance Raman Spectra of Heme-C and Heme-D1 in Pseudomonas Cytochrome Oxidase.** *FEBS Letter* 138(2):239-244, 1982.
- Chu S., Wong S., **Linear Pulse Propagation in an Absorbing Medium.** *Phys Rev L* 48(11):738-741, 1982.
- Chu S. N. G., Jodlauk C. M., Ballman A. A., **New Dislocation Etchant for InP.** *J Elchem So* 129(2):352-354, 1982.
- Chu S., Gibbs H. M., Passner A., **Single-Ion-Pair Fluorescence Ratios in Ruby and Anderson Localization.** *Phys Rev B* 24(12):7162-7173, 1981.

- Citrin P. H., Eisenberg P., Rowe J. E., **Adsorbate Structure on Reconstructed Semiconductors—Te and I on Si (111)7X7 and Ge(111)2X8.** *Phys Rev L* 48(12):802-805, 1982.
- Cohen J. D., Lang D. V., Harbison J. P., Sergent A. M., **Study of Light-Induced Changes in A-Si-H by Detailed Computer Modeling of Admittance and DLTS.** *J Physique* 42(NC4):371-374, 1981.
- Colvard C., Merlin R., Klein M. V., Gussard A. C., **Light-Scattering from Phonons in GaAs-AlAs Super-Lattices.** *J Physique* 42(NC6):631-633, 1981.
- Coppersmith S. N., Fisher D. S., Halperin B. I., Lee P. A., Brinkman W. F., **Dislocations and the Commensurate-Incommensurate Transition in Two Dimensions.** *Phys Rev B* 25(1):349-363, 1982.
- Cross M. C., **Ingredients of a Theory of Convective Textures Close to Onset.** *Phys Rev A* 25(2):1065-1076, 1982.
- Dautremont-Smith W. C., **Transition-Metal Oxide Electrochromic Materials and Displays—A Review. I. Oxides With Cathodic Coloration.** *Displays* 3(1):3-22, 1982.
- Dietz R. E., Yafet Y., Williams G. P., Lapeyre G. J., Anderson J., **Sum-Rule Test for Coherent and Incoherent Contributions to the Photo-Electron Cross Section Near Core-Electron Resonances in Metallic Ni and Pt.** *Phys Rev B* 24(12):6820-6830, 1981.
- Dutta N. K., Nelson R. J., **The Case for Auger Recombination in $In_{1-x}Ga_xAs_yP_{1-y}$.** *J Appl Phys* 53(1):74-92, 1982.
- Dynes R. C., **Electron Localization and Coulomb Interactions in Two Dimensions.** *Surf Sci* 113(1-3):510-517, 1982.
- Eisinger J., Flores J., **The Relative Locations of Intramembrane Fluorescent Probes and of the Cytosol Hemoglobin in Erythrocytes Studied by Transverse Resonance Energy Transfer.** *Biophys J* 37(1):6-7, 1982.
- Englert T., Tsui D. C., Gossard A. C., Uihlein C., **G-Factor Enhancement in the 2D Electron-Gas in GaAs/AlGaAs Heterojunctions.** *Surf Sci* 113(1-3):295-300, 1982.
- Epelboin Y., Patel J. R., **Determination of Burger's Vectors of Dislocations in Synthetic Quartz by Computer-Simulation.** *J Appl Phys* 53(1):271-275, 1982.
- Feldman L. C., **Atomic Positions of Surface Atoms Using High-Energy Ion Scattering.** *Nucl Instru* 191(1-3):211-219, 1981.
- Fishman G., Pinczuk A., Worlock J. M., Stormer H. L., Gossard A. C., Wiegmann W., **Coupled Electron-LO Phonon Excitation in a Two-Dimensional Electron System.** *J Physique* 42(NC6):305-307, 1981.
- Gallagher P. K., Johnson D. W., **Solid-State Reactivity in the System $Na_2CO_3-CaCO_3$.** *J Phys Chem* 86(2):295-297, 1982.
- Giannetta R. W., Ikezi H., **Macroscopic Structures on the Electron Charged Surface of Liquid-He-4.** *Surf Sci* 113(1-3):412-418, 1982.
- Gray E. W., Harrington D. J., **Voltage Breakdown Between Closely Spaced Electrodes Over Polymeric Insulator Surfaces in Air.** *J Appl Phys* 53(1):237-244, 1982.
- Guillon D. et al., **Liquid Crystals Under Pressure—X-ray Investigation of Smectic C-Phases.** *J Chem Phys* 76(4):2056-2063, 1982.
- Harmon B. N., Weber W., Hamann D. R., **Vibrational Frequencies Via Frozen Phonons.** *J Physique* 42(NC6):628-630, 1981.
- Hart R. M., Bergman J. G., Wokaun A., **Surface-Enhanced Raman Scattering From Silver Particles on Polymer-Replica Substrates.** *Optics Lett* 7(3):105-107, 1982.
- Hauser J. J., **Amorphous Semiconducting Ag-Te Films.** *J Physique* 42(NC4):943-946, 1981.
- Heaven M., Miller T. A., Freeman R. R., White J. C., Bokor J., **Two-Photon Absorption, Laser-Induced Fluorescence Detection of C1 Atoms.** *Chem P Lett* 86(5-6):458-462, 1982.
- Hegarty J., Sturge M. D., Gossard A. C., Wiegmann W., **Resonant Degenerate Four-Wave Mixing in GaAs Multiquantum Well Structures.** *Appl Phys L* 40(2):132-134, 1982.
- Heimann P. A., Olsen J. E., **A Sensitive Method for Measuring Surface Conductivity of Insulators.** *J Appl Phys* 53(1):546-549, 1982.

- Hensel J. C., Dynes R. C., Tsui D. C., **Absorption of Ballistic Phonons by the 2D Electron-Gas in a Si MOSFET.** *J Physique* 42(NC6):308-310, 1981.
- Hensel J. C., Dynes R. C., Tsui D. C., **Absorption of Ballistic Phonons by the 2D-Electron Gas in a Si MOSFET.** *Surf Sci* 113(1-3):249-255, 1982.
- Hensel J. C., Dynes R. C., Unterwal F. C., Simons A. L., **Singular Effects in Phonon Focusing—Formation of Phonon Focusing Caustics.** *J Physique* 42 (NC6):212-214, 1981.
- Huppert D. et al., **Dynamics of the Dual Fluorescences of Para-Dimethylamino-benzonitrile.** *J Photochem* 18(1):89-95, 1982.
- Iwahana K. et al., **Raman Scattering From TMTSF Salts.** *Molec Cryst* 79(1-4):39-47, 1982.
- Jackson S. A., Platzman P. M., **Polaronic Aspects of a 2D Electron on the Surface of a Liquid He Film.** *Surf Sci* 113(1-3):401-404, 1982.
- Jewell J. L., Gibbs H. M., Targ S. S., Gossard A. C., Wiegmann W., **Regenerative Pulsations From an Intrinsic Bistable Optical Device.** *Appl Phys L* 40(4):291-293, 1982.
- Kamgar A., Tsui D. C., **The Shubnikov-Dehaas Effect in Micron and Sub-Micron Si MOSFETS.** *Surf Sci* 113(1-3):467-473, 1982.
- Kaplan M. L., Reents W. D., **Cyclopenta(Para-Phenylene Sulfide) and Cyclo-tetra(Para-Phenylene Sulfide)—Examples of New Macrocyclic Series.** *Tetrahedr L* 23(4):373-374, 1982.
- Kaplan M. L. et al., **Electrical Conductivity in TCNQ Salts of Bis(4-Dimethylamino)phenylimino) Sulfur and Its Structural Analogs.** *Molec Cryst* 80(1-4):51-66, 1982.
- Karlicek R. F., Donnelly V. M., Collins G. J., **Laser-Induced Metal Deposition on InP.** *J Appl Phys* 53(2):1084-1090, 1982.
- Keith H. D., **Optical Behavior and Polymorphism in Poly(ethylene Sebacate). 1. Morphology and Optical Properties.** *Macromolec* 15(1):114-122, 1982.
- Keith H. D., **Optical Behavior and Polymorphism in Poly(ethylene Sebacate). 2. Properties of the New Polymorph.** *Macromolec* 15(1):122-126, 1982.
- Khanarian G., Tonelli A. E., **Kerr Effect and Dielectric Study of Poly(oxyethylene Glycols).** *Macromolec* 15(1):145-148, 1982.
- Kobayashi T., Ohashi Y., **Intersystem Crossing in IR and RH Complexes Studied by Nanosecond and Picosecond Spectroscopy.** *Chem P Lett* 86(3):289-294, 1982.
- Kobayashi T., **Picosecond Time-Resolved Sn ← S1 Absorption Spectrum of the Tetracyanobenzene Toluene Complex.** *Chem P Lett* 85(2):170-174, 1982.
- Kolks G. et al., **Magnetic Exchange in Imidazolate-Bridged Copper(II) Complexes.** *J Am Chem S* 104(3):717-725, 1982.
- Kress, W. et al., **Phonons in Mixed-Valence Compounds.** *J Physique* 42(NC6):3-10, 1981.
- Kumar J., Silfvast W. T., Wood O. R., **Infrared Emission and Recombination From a Dense Sodium Plasma Produced by Resonant Optical Pumping.** *J Appl Phys* 53(1):218-222, 1982.
- Lang D. V., Cohen J. D., Harbison J. P., **Observation of a Reversible Field-Induced Doping Effect in Hydrogenated Amorphous Silicon.** *Phys Rev L* 48(6):421-424, 1982.
- Laughlin R. B., **Impurities and Edges in the Quantum Hall Effect.** *Surf Sci* 113(1-3):22-26, 1982.
- Lavine, C. F., Wagner R. J., Tsui D. C., **Magnetic Field Dependence of the Photo-response of the Electron Inversion Layer on (100) Si.** *Surf Sci* 113(1-3):112-117, 1982.
- Lewerenz H. J., Ferris S. D., Doherty C. J., Leamy H. J., **Charge Collection Microscopy on P-WSE2—Recombination Sites and Minority-Carrier Diffusion Length.** *J Elchem So* 129(2):418-423, 1982.
- Lovinger A. J., **Annealing of Poly(vinylidene Fluoride) and Formation of a 5th Phase.** *Macromolec* 15(1):40-44, 1982.
- MacLennan C. G. et al., **Effects of Titan on Trapped Particles in Saturn's Magnetosphere.** *J Geo R-S P* 87(NA3):1411-1418, 1982.
- Matsuoka S., **Excess Entropy and Stress-Strain Behavior of Polymeric Glasses.** *J Macr S Ph B* 19(4):715-728, 1981.

- Miller A., Miller D. A. B., Smith, S. D., **Dynamic Non-Linear Optical Processes in Semiconductors.** *Adv Physics* 30(6):697-800, 1981.
- Miller G. L. et al., **A Technique for Investigating the Properties of Surfaces, Thin-Films, and Interfaces by Means of a Mechanical Marginal Oscillator.** *J Appl Phys* 53(2):979-983, 1982.
- Murarka S. P., Read M. H., Doherty C. J., Fraser D. B., **Resistivities of Thin-Film Transition-Metal Silicides.** *J Elchem So* 129(2):293-301, 1982.
- Murayama K., Bosch M. A., **Radiative Recombination of Localized Excitons in Amorphous and Crystalline As₂S₃.** *J Physique* 42(NC4):343-346, 1981.
- Murray C. A., Allara D. L., **Measurement of the Molecule-Silver Separation Dependence of Surface Enhanced Raman Scattering in Multilayered Structures.** *J Chem Phys* 76(3):1290-1303, 1982.
- Narayanamurti V., **Transport of High-Energy Phonons.** *J Physique* 42(NC6):221-225, 1981.
- Nelson D. F., Cooper J. A., **High-Field Electron Velocities in Silicon Surface Inversion-Layers.** *Surf Sci* 113(1-3):267-272, 1982.
- Ng K. K. et al., **Effects of Grain Boundaries on Laser Crystallized Poly-Si MOSFETS.** *Elec Dev L* 2(12):316-318, 1981.
- Panock R., Freeman R. R., Zegarski B. R., Miller T. A., **Anticrossing Spectroscopy of the N = 6, 7, 8-1, 3 D States in He-3.** *Phys Rev A* 25(2):869-875, 1982.
- Patel D. J. et al., **Extra Adenosine Stacks Into the Self-Complementary d(CGCGAATTCGCG) Duplex in Solution.** *Biochem* 21(3):445-451, 1982.
- Patel D. J. et al., **Premelting and Melting Transitions in the d(CGCGAATTCGCG) Self-Complementary Duplex in Solution.** *Biochem* 21(3):428-436, 1982.
- Patel D. J. et al., **Structure, Dynamics, and Energetics of Deoxyguanosine-Thymidine Wobble Base Pair Formation in the Self-Complementary d(CGTGAATTCGCG) Duplex in Solution.** *Biochem* 21(3):437-444, 1982.
- Patel D. J. et al., **Structure and Energetics of a Hexanucleotide Duplex With Stacked Trinucleotide Ends Formed by the Sequence d(GAATTCGCG).** *Biochem* 21(3):451-455, 1982.
- Phillips J. C., **Domain Microscopy in Chalcogenide Alloy Glass Thin-Films.** *J Physique* 42(NC4):197-200, 1981.
- Phillips J. C., **The Physics of Glass.** *Phys Today* 35(2):27-33, 1982.
- Pinczuk A., Worlock J. M., **Light Scattering by Two-Dimensional Electron Systems in Semiconductors.** *Surf Sci* 113(1-3):69-84, 1982.
- Poate J. M., **Ion-Beam Analysis of Semiconductor Interfaces.** *Nucl Instru* 191(1-3):39-46, 1981.
- Powers L. et al., **Structural Features of the Copper-Depleted Cytochrome-Oxidase From Beef-Heart Iron EXAFS.** *FEBS Letter* 138(2):245-248, 1982.
- Ramakrishnan T. V., **Density Wave Theory of First-Order Freezing in Two Dimensions.** *Phys Rev L* 48(8):541-545, 1982.
- Reents W. D., Kaplan M. L., **Mass-Spectral Analysis of Poly(Para-Phenylene Sulfide).** *Polymer* 23(2):310-313, 1982.
- Revesz A. G., Wemple S. H., Gibbs G. V., **Structural Ordering Related to Chemical Bonds in Random Networks.** *J Physique* 42(NC4):217-219, 1981.
- Reynolds C. L., Tamargo M. C., Anthony P. J., Zilko J. L., **Analysis of the Short-Time Liquid-Phase Epitaxial-Growth of Al_xGa_{1-x}As.** *J Cryst Gr* 57(1):109-112, 1982.
- Rosetti R., Brus L. E., **Time Resolved Energy Transfer From Electronically Excited 3b3u Pyrazine Molecules to Planar Ag and Au Surfaces.** *J Chem Phys* 76(2):1146-1149, 1982.
- Sato T., Hasegawa A., **Externally Driven Magnetic Reconnection Versus Tearing Mode Instability.** *Geophys R L* 9(1):52-55, 1982.
- Schilling F. C., **C-13 NMR Triple-Resonance Measurements Using Simultaneous Fluorine and Proton Decoupling.** *J Magn Res* 47(1):61-67, 1982.
- Schluter M., Sham L. J., **Density Functional Theory.** *Phys Today* 35(2):36-43, 1982.
- Schwenk H. et al., **Meissner Anisotropy in Deuterated (TMTSF)₂ClO₄.** *Molec Cryst* 79(1-4):277-282, 1982.
- Sessler G. M., West J. E., Gerhard G., **High-Resolution Laser-Pulse Method for Measuring Charge Distribution in Dielectrics.** *Phys Rev L* 48(8):563-566, 1982.

- Shah J., **Investigation of Hot Carrier Relaxation With Picosecond Laser Pulses.** *J Physique* 42(NC7):445-462, 1981.
- Shank C. V., Fork R. L., Greene B. I., Weisbuch C., Gossard A. C., **Picosecond Dynamics of Highly Excited Multiquantum Well Structures.** *Surf Sci* 113(1-3):108-111, 1982.
- Shank C. V., Auston D. H., **Ultrafast Phenomena in Semiconductor Devices.** *Science* 215(4534):797-801, 1982.
- Slusky S. E. G., Jackel L. D., **Transient Analysis of Low-Hysteresis Josephson Interferometer With Feedback.** *J Appl Phys* 53(1):740-743, 1982.
- Smith P. W. et al., **Bistability at an Electrooptic Interface.** *Optics Lett* 7(2):57-59, 1982.
- Snyder L. C. et al., **Stability and Bonding of Disilyne and Its Isomers—A Generalized Valence Bond-Effective Potential Study.** *Int J Quant* 21(3):565-579, 1982.
- Stillinger F. H., **Capillary Waves and the Inherent Density Profile for the Liquid Vapor Interface.** *J Chem Phys* 76(2):1087-1091, 1982.
- Stillinger F. H., Weber T. A., **Hidden Structure in Liquids.** *Phys Rev A* 25(2):978-989, 1982.
- Stolen R. H., Bosch M. A., **Low-Frequency and Low-Temperature Raman Scattering in Silica Fibers.** *Phys Rev L* 48(12):805-808, 1982.
- Stone J., Walrafen G. E., **Overtone Vibrations of OH Groups in Fused-Silica Optical Fibers.** *J Chem Phys* 76(4):1712-1722, 1982.
- Stormer H. L., Tsui D. C., Gossard A. C., **Zero Resistance State and Origin of the Quantized Hall Effect in Two-Dimensional Electron Systems.** *Surf Sci* 113(1-3):32-38, 1982.
- Stronach C. E., Squire K. R., Arrott A. S., Patterson B. D., Heinrich B., Lankford W. F., Fiory A. T., Kossler W. J., Singh J. J., **Muon Hyperfine Fields in Iron and Its Dilute Alloys.** *J Magn Magn* 25(2):187-193, 1981.
- Swartz R. G. et al., **A Technique for Rapidly Alternating Boron and Arsenic Doping in Ion-Implanted Silicon Molecular-Beam Epitaxy.** *Appl Phys L* 40(3):239-241, 1982.
- Tamari N., **Tin Doping of Active Region in InGaAsP/InP Lasers.** *Appl Phys L* 40(2):108-110, 1982.
- Targ S. S., Tai K., Jewell J. L., Gibbs H. M., Gossard A. C., McCall S. L., Passner A., Venkates T. N., Wiegmann W., **External Off and On Switching of a Bistable Optical Device.** *Appl Phys L* 40(3):205-207, 1982.
- Tien Z. J., Worlock J. M., Perry C. H., Pinczuk A., Aggarwal R. L., Stormer H. L., Gossard A. C., Wiegmann W., **Light Scattering from Two-Dimensional Electron Systems in Strong Magnetic Fields.** *Surf Sci* 113(1-3):89-93, 1982.
- Tsang W. T., **Extremely Low Threshold (AlGa)As Graded-Index Wave-Guide Separate Confinement Heterostructure Lasers Grown by Molecular-Beam Epitaxy.** *Appl Phys L* 40(3):217-219, 1982.
- Tsang W. T., **Recent Progress in Growing Reliable (AlGa)As DH Lasers by Molecular-Beam Epitaxy for Optical Communication Systems.** *J Cryst Gr* 56(20):464-474, 1982.
- Tsui D. C., Gossard A. C., Kaminsky G., Wiegmann W., **Transport Properties of GaAs IGFETS.** *Surf Sci* 113(1-3):464-466, 1982.
- Ugurbil K. et al., **P-31 Nuclear Magnetic Resonance Studies of Bioenergetics in Wild-Type and Adenosinetriphosphatase(1-) Escherichia-Coli-Cells.** *Biochem* 21(5):1068-1075, 1982.
- Ulbrich R. G., Narayanamurti V., Chin M. A., **Ballistic Transport and Decay of Near Zone-Edge Nonthermal Phonons in Semiconductors.** *J Physique* 42(NC6):226-228, 1981.
- Vanuitert L. G., **Relations for Hydration Enthalpies of Metalion Hydrates and Stability Constants of Metal Dibenzoylmethane Chelate Complexes.** *Mater Res B* 17(2):223-230, 1982.
- Voorhoeve R. J., Trimble L. E., Nakajima S., Banks E., **Square Concentration Pulses in Oxidation Catalysis Over Perovskite-Type Oxides of Manganese and Iron.** *ACS Symp S* 1982(178):253-266, 1982.
- Wells R., Hammond K., Lamola A. A., Blumberg W. E., **Relationships of Bilirubin Binding Parameters.** *Clin Chem* 28(3):432-439, 1982.

- Willens R. H., Kornblit A., Testardi L. R., Nakahara S., **Melting of Pb as It Approaches a Two-Dimensional Solid.** Phys Rev B 25(1):290-296, 1982.
- Williams J. M. et al., **New (TMTSF)₂X Derivatives—A Change in the Selenium Network Dimensionality Derived From the Molecular and Crystal Structures of (TMTSF)₂(FSO₃) < T = 298K, 123K* and (TMTSF)₂(BR04)T = 298K.** Molec Cryst 79(1-4):319-326, 1982.
- Wood O. R., Patel C. K. N., Murnick D. E., Nelson E. T., Leventhal M., Kugel H. W., Niv Y., **Measurement of the Lamb Shift in Hydrogenic Cl-16+.** Phys Rev L 48(6):398-402, 1982.
- Wudl F., **A Spin-Charge Separation Hypothesis Based on the Structure of the Salts (TMTSF)₂PF₆-, (TMTSF)₂ASF₆-.** Molec Cryst 79(1-4):67-78, 1982.
- Yoshizawa H. et al., **Random-Field Effects in Two-Dimensional, and Three-Dimensional Ising Antiferromagnets.** Phys Rev L 48(6):438-441, 1982.
- Young J. S., Langer W. D., Goldsmith P. F., Wilson R. W., **Coupling of the Magnetic Field and Rotation in the Dark Cloud-B5.** Astrophys J 251(2):L 81-L 84, 1981.
- Zilco J. L., Williams R. S., **Auger-Electron Spectroscopy Study of GaAs Substrate Cleaning Procedures.** J Elchem So 129(2):406-408, 1982.

SOCIAL AND LIFE SCIENCES

- Eisinger J., Flores J., Salhany J. M., **Association of Cytosol Hemoglobin With the Membrane in Intact Erythrocytes.** P Nas Biol 79(2):412, 1982.
- Samuel A. G. et al., **Length Effects in Word Perception—We is Better Than I But Worse Than You or Them.** J Exp Psy P 8(1):91-105, 1982.

CONTENTS, SEPTEMBER 1982

PART 1

- Wideband, Bidirectional, Lightguide Communication With an
Optically Powered Audio Channel
R. C. Miller, B. C. De Loach, T. S. Stakelon, and R. B. Lawry
- Equalization of Multimode Optical Fiber Systems
B. L. Kasper
- Frequency-Hopped Single-Sideband Modulation for Mobile Radio
V. K. Prabhu and R. Steele
- Description of Fasnet—A Unidirectional Local-Area Communications
Network
J. O. Limb and C. Flores
- On the Distribution Function and Moments of Power Sums With
Log-Normal Components
S. C. Schwartz and Y. S. Yeh
- Piecewise Linear Approximation of Multivariate Functions
G. S. Lee
- A Traffic Overflow System With a Large Primary Queue
J. A. Morrison and P. E. Wright
- Memoryless Nonlinearities With Gaussian Inputs: Elementary Results
H. E. Rowe
- A Variation on CSMA/CD That Yields Movable TDM Slots in Inte-
grated Voice/Data Local Networks
N. F. Maxemchuk

PART 2

STORED PROGRAM CONTROLLED NETWORK

- Prologue
F. T. Andrews, Jr. and K. E. Martersteck
- Overview
S. Horing, J. Z. Menard, R. E. Staehler, and B. J. Yokelson
- Generic Network Plan
J. J. Lawser, R. E. LeCronier, and R. L. Simms

Routing of Direct-Signaling Messages in the CCIS Network
R. F. Frerking and M. A. McGrew

No. 1/1A ESS—SPC Network Capabilities and Signaling
Architecture

L. J. Gawron, S. J. Lueders, and K. L. Moeller

CCIS and SPC Network Performance

E. A. Davis, C. J. Funk, and J. M. Sebeson

Calling Card Service—Overall Description and Operational
Characteristics

R. G. Basinger, M. Berger, E. M. Prell, V. L. Ransom, and
J. R. Williams

Calling Card Service—TSPS Hardware, Software, and Signaling
Implementation

D. E. Confalone, B. W. Rogers, and R. J. Thornberry, Jr.

Calling Card Service—Human Factors Studies

D. J. Eigen and E. A. Youngs

800 Service Using SPC Network Capability

D. Sheinbein and R. P. Weber

800 Service Using SPC Network Capability—Network
Implementation and Administrative Functions

C. W. Haas, D. C. Salerno, and D. Sheinbein

Data Base Administration System—Overall Description and
Operational Characteristics

R. G. Barrere, J. P. Delatore, J. W. Lurtz, R. J. Piereth,
and C. M. Rubald

Data Base Administration System—Architecture and Data Base
Design

S. F. Sampson and D. W. Tietz

THE BELL SYSTEM TECHNICAL JOURNAL is abstracted or indexed by *Abstract Journal in Earthquake Engineering, Applied Mechanics Review, Applied Science & Technology Index, Chemical Abstracts, Computer Abstracts, Current Contents/Engineering, Technology & Applied Sciences, Current Index to Statistics, Current Papers in Electrical & Electronic Engineering, Current Papers on Computers & Control, Electronics & Communications Abstracts Journal, The Engineering Index, International Aerospace Abstracts, Journal of Current Laser Abstracts, Language and Language Behavior Abstracts, Mathematical Reviews, Science Abstracts (Series A, Physics Abstracts; Series B, Electrical and Electronic Abstracts; and Series C, Computer & Control Abstracts), Science Citation Index, Sociological Abstracts, Social Welfare, Social Planning and Social Development, and Solid State Abstracts Journal*. Reproductions of the Journal by years are available in microform from University Microfilms, 300 N. Zeeb Road, Ann Arbor, Michigan 48106.



Bell System